

https://dspace.org/

Prototype damper for use in deep foundation pile testing

Vorster, Kyle Sidney

2012-07-04
http://hdl.handle.net/10539/11599

Downloaded from a DSpace repository. https://dspace.org/

PROTOTYPE DAMPER FOR USE IN DEEP FOUNDATION PILE TESTING

Kyle Sidney Vorster

A dissertation submitted to the Faculty of Engineering and the Built Environment, University of the Witwatersrand, Johannesburg, in fulfilment of the requirements for the degree of Master of Science in Engineering.

Johannesburg, 2011

DECLARATION

I declare that this dissertation is my own, unaided work, other than where specifically acknowledged. It is being submitted for the degree of Master of Science in Engineering in the University of the Witwatersrand, Johannesburg. It has not been submitted before for any degree or examination in any other university.

Signed this _____ day of _____ 2011

_____

Kyle Sidney Vorster

ABSTRACT

A new method of testing deep foundation piles is proposed, focusing specifically on rapid load testing. The test involves applying a controlled force to a pile by dropping a weight and damper on it. The specific damper provided required modification of the annular gap to accommodate the magneto-rheological fluid, which replaces the hydraulic fluid. Two accelerometers and one K-type thermocouple monitor the damper by means of a control circuit with a programmable micro-controller. The control circuit bus impedance and board capacitance are evaluated. The control circuit outputs a signal which switches a coil housed inside the damper. This coil generates a field in the annular gap that changes the amount of damping, and consequently alters the applied force. With a control algorithm implemented, it is possible to attain the desired impact on a pile, potentially giving an insight into its load bearing capabilities.

ACKNOWLEDGEMENTS

While many simply assist, Prof. G. Gibbon contributed to the growth of both this dissertation and the author. A special thanks is also due to Dr. I. Luker who instigated and guided the project requirements, as well as provided the shock absorber. Sidney Vorster aided in numerous ways, including construction and a pair of hands when two were not enough. Much thanks is given to Bradford Cunningham, who - with the aid of Prof. I. Hofsajer - worked with the author for the design and evaluation of the controller circuit, as well as the thermocouple design.

CONTENTS

DECLARATION ii

LIST OF FIGURES viii

LIST OF TABLES x

1 INTRODUCTION 1

1.1 Types of Piles . . . 1

1.2 Non-destructive Pile Testing . . . 2

1.3 Magneto-rheological Fluid . . . 5

1.3.1 Specifications and composition . . . 5

1.3.2 Operation and function . . . 6

1.3.3 Modelling . . . 7

1.4 Aims of Study . . . 9

2 FORMULATION OF THE PROBLEM 10

2.1 Rapid Load Test (RLT) . . . 10

2.2 Similar Tests . . . 11

2.2.1 Statnamic test . . . 12

2.2.2 Fundex pile test . . . 12

2.3 Review of Work . . . 13

2.4 Methodology . . . 14

2.4.1 Objectives . . . 14

2.4.2 Factors influencing results . . . 15

2.5 Scope . . . 16

3 DAMPER AND MAGNETIC CIRCUIT 17

3.1 Damper . . . 17

3.1.1 Physical parameters . . . 18

3.1.2 Operation 21
3.1.3 Maintenance and construction 22
3.2 Magnetic Circuit 23
3.2.1 Operation 23
3.2.2 Magnetic model 24
3.2.3 Final coil design and placement 27
3.2.4 Equivalent circuit model 28
3.3 Annular Gap 28
3.3.1 Parallel-plate model 29
3.3.2 Dynamic range and controllable force 29
3.3.3 Discussion of the results 31
3.4 Conclusion 33

4 CONTROLLER AND DRIVER CIRCUITS 34
4.1 Controller Circuit 34
4.1.1 Functional overview 34
4.1.2 Controller features 39
4.1.3 Development board 41
4.2 Driver Circuit 42
4.2.1 Functional overview 42
4.2.2 Operation and analysis 43
4.3 Packaging 45
4.3.1 Outline of requirements 45
4.3.2 Internal positioning of equipment 46
4.3.3 External access 47
4.3.4 Display 48
4.4 Conclusion 49

5 TRANSDUCERS 50
5.1 Accelerometers 50
5.1.1 Functional overview 50
5.1.2 Sampling and converting 51
5.1.3 Placement and performance 52
5.1.4 Accelerometer calibration 53
5.2 Thermocouple and Heating Effects 59
5.2.1 Functional overview 59

5.2.2 Sampling and converting 60
5.2.3 Placement and performance 61
5.2.4 Thermocouple calibration 62
5.3 Conclusion 66

6 EXPERIMENTAL PROCEDURE FOR THE DROP TESTS 67
6.1 Emulation of Pile Testing 67
6.2 Development of Drop Rig 68
6.3 Practical Errors 69
6.4 Experimental Procedure and Methodology 70
6.5 Conclusion 72

7 RESULTS AND DISCUSSION 73
7.1 Experiment Observations 73
7.1.1 Stationary testing 73
7.1.2 Thermal response 75
7.1.3 Incremented frequency 76
7.1.4 Incremented duty cycle 76
7.2 Analysis 78
7.3 Conclusion 80

8 SUMMARY CONCLUSIONS AND RECOMMENDATIONS 81
8.1 Recommendations for Future Work 81
8.2 Summary and Conclusions 83

A CONTROLLER SCHEMATIC 84

B DRIVER SCHEMATIC 86

REFERENCES 88

BIBLIOGRAPHY 92

LIST OF FIGURES

1.1 Common load bearing pile types, adapted from [2] 2
1.2 Load comparison of the various testing methods, adapted from [5]. . 4
1.3 Comparison of the force profile developed along the pile [4]. 4
1.4 Operation of the magnetic particles when a magnetic field is applied. 6
1.5 Newton model of fluid [7]. 8
2.1 The RLT using the Unloading Point Method, adapted from [4, 24] . 11
2.2 The typical Statnamic test apparatus, adapted from [5]. 12
2.3 Concept behind the Fundex Pile Test [3]. 13
2.4 The results from the damper in its second revision. 13
3.1 Isometric model view and photograph. 18
3.2 An exploded view of the damper. 19
3.3 Annotated diagram of the spring. 20
3.4 Half cross-section of the damper viewed from the top plane. 21
3.5 Operation of the damper as it impacts with the test pile. 22
3.6 Cross-section of the magnetic circuit region. 24
3.7 Equivalent magnetic circuit model. 25
3.8 Number of turns versus the flux density in the gap. 26
3.9 The relationship between the gap and current for the installed coil. . 26
3.10 Photograph of piston with wound coil and thermocouple cable. . . . 27
3.11 Equivalent circuit of the coil. 28
3.12 Behaviour of MR fluid through a parallel duct, adapted from [7]. . . 30
3.13 Decomposition of forces in an MR fluid, adapted from [7]. 30
3.14 Modelled response of shock absorber for a change in gap size. 32
4.1 Photograph of the controller unit, showing the populated PCB. . . . 35
4.2 Controller functional overview block diagram 35
4.3 Bode diagram of the thermocouple filters. 36
4.4 Bode diagram of the accelerometer filters. 37
4.5 Pull-up LED indicator circuit. 38

4.6 Block diagram representation of the controller functions. 39
4.7 Top and bottom layers of the controller PCB. 41
4.8 Block diagram representation of the driver circuit. 42
4.9 Photograph of the driver circuit on veroboard. 44
4.10 Simulation of the current through the coil versus the gate voltage. . 45
4.11 Photograph of the internal positioning of the circuits. 46
4.12 Photograph of the package taken from the top view. 48
5.1 Photograph of an accelerometer on the supplied development board. 51
5.2 Block diagram of the accelerometer circuit. 51
5.3 Positioning and casing for the accelerometer circuits. 52
5.4 The accelerometer as placed on a rotating trajectory, adapted from [53]. 53
5.5 Flow diagram of the calibration code. 55
5.6 The mounted accelerometer and circuit in the lathe. 56
5.7 Results obtained from three experiments at 430 RPM using Acc 1. . 57
5.8 Calibration curves for the accelerometers. 58
5.9 Block diagram of the thermocouple circuit. 60
5.10 Placement of the thermocouple cable through the piston. 61
5.11 Flow diagram of the thermocouple calibration process. 63
5.12 Results obtained directly from the calibration process. 64
5.13 Typical noise on thermocouple circuit at 38,5 °C. 64
5.14 The calibration curve for the thermocouple amplifier. 65
5.15 Comparison between calibrated and non-calibrated error. 65
6.1 Photograph of the drop rig. 68
6.2 Misalignment affect on the experiment. 69
6.3 Flow diagram of the manual procedure. 71
7.1 Comparison of the two accelerometers. 74
7.2 Accelerometer output while stationary. 74
7.3 Thermal response of the three operating frequencies. 75
7.4 Comparison of all the different frequency schemes. 76
7.5 Acceleration data from three tests under identical conditions. 77
7.6 Comparison of all the different duty cycle schemes. 78
7.7 Illustrative graph of the different regions during damping. 79
A.1 Circuit diagram of the controller. 85
B.1 Circuit diagram of the MOSFET driving circuit. 87

LIST OF TABLES

1.1 MR fluid relevant properties [16] 6
2.1 Project objectives and success criteria. 15
3.1 Spring specifications. 20
3.2 Worst case magnetic circuit parameters. 25
3.3 Coil design parameter. 27
5.1 Accelerometer relevant specifications [29]. 53
5.2 Calibration data as it relates to the speed of rotation. 56
5.3 Accelerometer error accumulation. 59
5.4 Thermocouple amplifier relevant specifications [55]. 62
5.5 Temperature circuit tolerances. 66
6.1 Final specifications of the drop test. 68
6.2 Summary of experiments performed on the damper 71

Chapter 1

INTRODUCTION

Piles are used for deep foundations. The integrity of an installed pile may be assessed using many different methods, where the appropriateness of the test method used is based on several conditions, including the type of pile to be tested. A new method of pile testing is proposed by making use of magneto-rheological fluid, which responds to a magnetic field. Using non-destructive testing methods, the goal is to develop a rapid load test similar to other currently available testing techniques.

1.1 Types of Piles

The earth's crust varies in terms of depth and composition. To address these varying conditions, there are many methods of constructing deep foundations, each one addressing certain geotechnical difficulties. There are three general categories of deep foundations, these are [1]:

1. Batter Piles
2. Sheet Piles
3. Load Bearing Piles

Batter piles provide lateral support and are driven at an inclination to the vertical [1]. Driven on a "batter", these piles are caused to compress from lateral forces. Sheet piles are formed by sheets or planks which lock together to form a retaining wall. This method of piling is generally used to retain soil banks or to form a barrier to the flow of water [1]. The shock absorber method would be inadequate at testing the piles mentioned so far, and as such is limited to only load bearing piles.

Commonly, load bearing piles act as subterranean columns, which are designed to support vertical loads [1]. A structure will transfer its load to these piles by means of the shaft head, which will in turn be transferred and distributed to the surrounding soil.

The tangential skin friction and the end bearing of the pile act to negate the downward force caused by the supported structure. Some common load bearing pile types are shown in Figure 1.1.

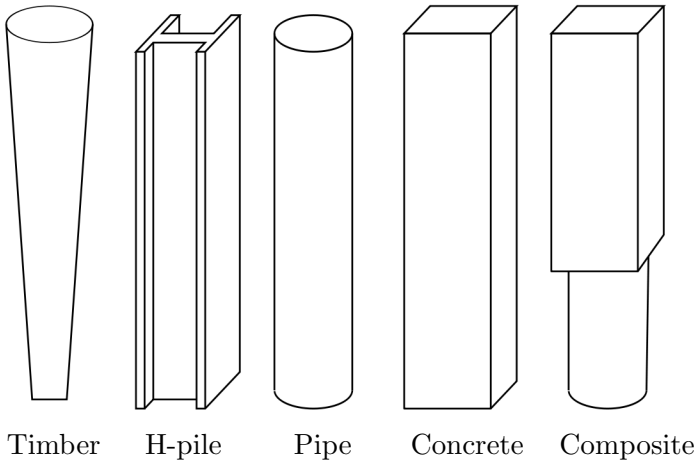


Figure 1.1: Common load bearing pile types, adapted from [2]

Each pile type has its own set of pros and cons, and are generally selected based on the final bearing load and soil conditions. For instance, timber piles can bear loads of up to 55 tons [2], compared with cast—in—place, concrete piles which can take up to 150 tons. Geometry of the pile and sub-surface effects also play a large role and need to be considered before pile testing.

1.2 Non-destructive Pile Testing

The use of non-destructive pile testing (NDT) gained acceptance in 1993 with the publication of the Federal Highway Administration report titled, "Drilled Shafts for Bridge foundations" [3]. The report developed concepts on drilled shafts and augured, cast—in—place (ACIP) piles in the USA, and forms many of the testing specifications.

The use of non-invasive testing as an alternative to full-scale tests are designed such that a foundation's integrity may be assessed without prohibitively large project costs [3], allowing for leaner and safer deep foundation designs. Pile load tests may be employed in all cycles of a pile's life. During pre-construction, the piling system to be implemented may require verification, and during construction the variations in soil and water conditions affect the piles' performance. Once installed, the piles' load capacity may be determined.

Pile load testing may be separated into four basic categories, according to the time required over which a load is applied. In order of longest to shortest, these are [4]:

1. Maintained or Static Load Test : hours to days
2. Constant Rate of Penetration Test : minutes
3. Rapid Load Test (RLT) : 50 – 200 ms
4. Dynamic Load Test (DLT) : 5 – 8 ms

While a pile may experience fast transient loads in its service lifetime, the majority of the time a pile would either carry a permanent load or a very slowly changing load. It follows that the more dissimilar the test is to normal operation, the more interpretation that would be required [3]. Conversely, the longer the test, the higher the cost and time required with which to test multiple piles.

The relative impacting weights are illustrated in Figure 1.2. The static test is used as the normalising factor, showing that a dynamic test uses approximately 2 % of the static test mass, and a rapid load test would use up to 10 % [5, 6].

The advantages for a fast test include less set-up time, reduced costs and less time required of skilled labour. Making use of these advantages, a comparison between the RLT and DLT is necessary to justify the approach taken. While both tests require more interpretation than the slower tests, the RLT is the simpler test to interpret [4]. This arises from the force profile developed along the length of the pile, as shown in Figure 1.3.

For the DLT, a compression wave caused by the force applied travels down the pile before being reflected at the base of the pile (all unlabelled arrows refer to forces due to soil effects). The RLT causes the entire pile to be in compression, which is closer to what the pile experiences during typical operation. The RLT is also less

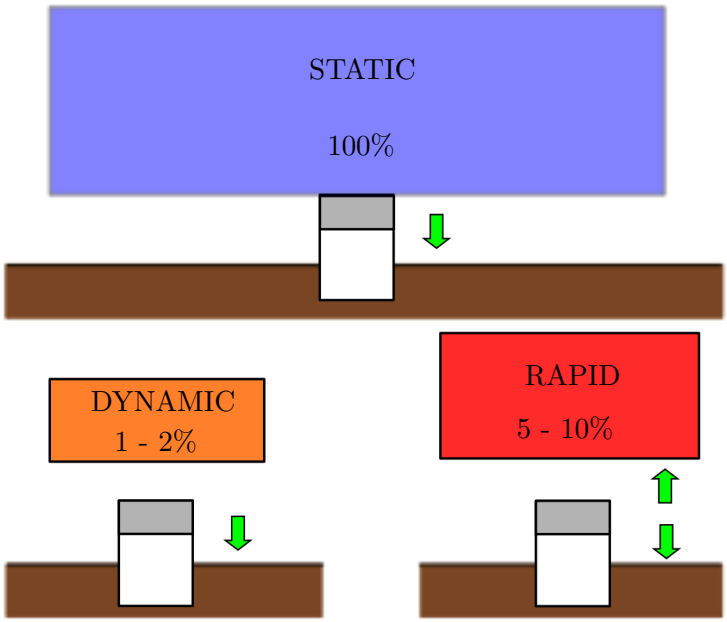


Figure 1.2: Load comparison of the various testing methods, adapted from [5].

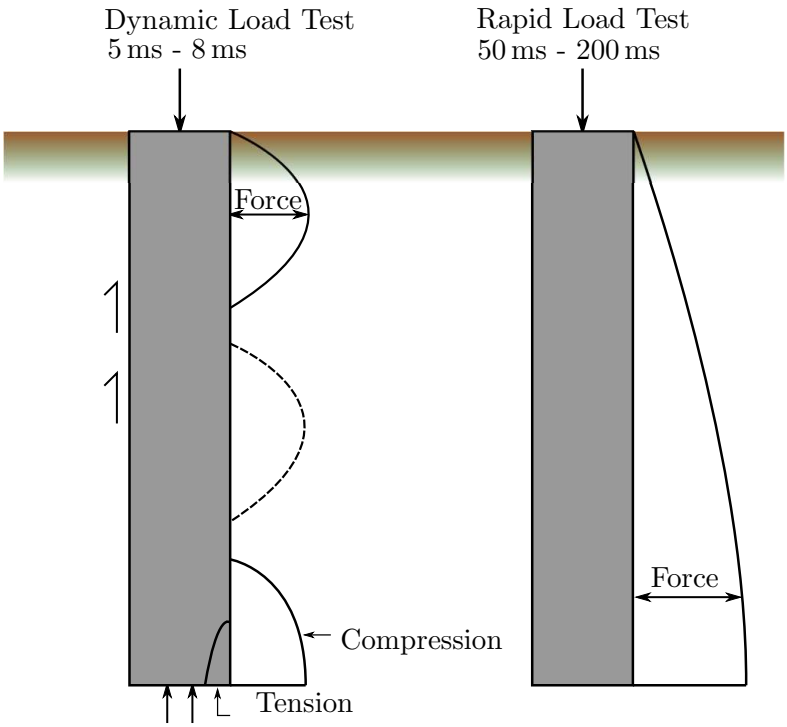


Figure 1.3: Comparison of the force profile developed along the pile [4].

affected by necks and bulging in the pile's cross section [3]. There are limitations to the pile size and number of piles tested for a given period of time using the RLT, but with less likelihood of damaging the pile.

1.3 Magneto-rheological Fluid

Magneto-rheological (MR) fluid was first developed by Jacob Rainbow at the US National Bureau of Standards in 1940 [7]. Together with Electro-rheological (ER) fluid, these fluids are often referred to as "intelligent" or "smart", despite the fact that the fluids are not capable of any information processing [8]. The misnomer comes from the fluids' ability to reversibly change properties based on an applied magnetic or electric field, for MR and ER fluids respectively. Typical fluids respond solely to the speed of either extension or compression.

MR fluids are composed of micron-sized particles suspended in a carrier liquid. When a magnetic field is applied to the fluid, these particles align and have the effect of changing the yield stress of the fluid. Consequently, a range of models were developed to better understand the nature of the fluid so that it may be used to its maximum potential in devices such as dampers [9–11].

1.3.1 Specifications and composition

Under normal conditions, MR fluids have a consistency comparable to motor oil [7]. However, MR fluids have the unique capability of interaction with magnetic fields [12]. This has the effect of solidifying the fluid and restricting movement. The fluid is generally made up of three components, namely [12, 13];

1. A liquid base or carrier liquid,
2. Colloidal sized magnetic particles,
3. and a Stabilizer.

The carrier liquid is chosen according to the application. The fluid is typically mineral oil, synthetic oil, water or glycol [14]. The liquid base functions as both a lubricant and to suspend tiny magnetic particles which respond to a magnetic field.

If these colloidal particles are smaller than 1–2 nm they lose their magnetic properties, but made too large and they will agglomerate due to the decreased effect of thermal activity [12]. Typical sizes for MR fluids vary between 3–10 nm [15]. The stabiliser prevents particles from aggregating, which is comprised of long chain

molecules (polymers or surfactants). The stabiliser forms a bonded monomolecular layer around each magnetic particle.

The MR fluid available is supplied by Lord Inc. [15], product code *MRF-132DG-250* [16]. This particular fluid has a hydrocarbon base, which is generally used for controllable, energy-dissipating applications. Examples include shock absorbers, dampers and brakes. The relevant MR fluid properties are reproduced in Table 1.1 for convenience.

Table 1.1: MR fluid relevant properties [16]

Appearance	Dark Gray Fluid
Viscosity @ 40 °C	0,092 ± 0,015 Pa − s
Density	2,98 to 3,18 g/cm^3
Flash Point	150 °C
Operating Temperature	−40 to 130 °C

Using the information provided in Table 1.1, along with the curves describing the magnetic properties and how it relates to shear stress, it is possible to design for both the controller and damper.

1.3.2 Operation and function

As shown in Figure 1.4, the MR fluid magnetic particles acquire a dipole moment, forming fibrils which align with the magnetic field [7, 8]. The stability of the fluid is dependant on the size of the colloidal particles.

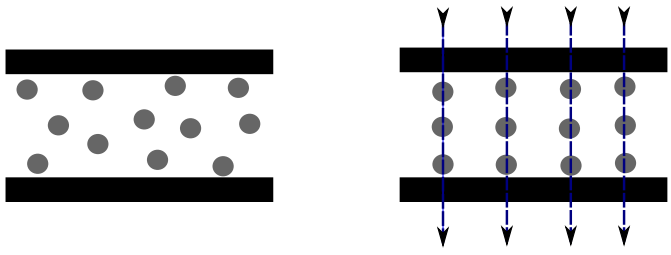


Figure 1.4: Operation of the magnetic particles when a magnetic field is applied.

M. T. Thompson found that when the fluid is exposed to a changing magnetic field the power loss is linearly dependant on the excitation frequency when in the range or 100 Hz to 1 MHz [17]. This is caused by the time lag between applying the

magnetic field and the time required to magnetize the particle, which is particularly relevant as the driver circuit applies a magnetic field by means of a PWM wave (see Section 4.2). The LORD Wonder Box also makes use of a PWM signal to control the fluid [18].

The MR fluid replaces the hydraulic fluid inside the damper, making it important to quantify the differences between typical oils and the proposed fluid. It is expected that the solid content will increase the effective viscosity [8]. There are three main affecting factors, namely [19];

1. Density
2. Kinematic viscosity
3. Dynamic viscosity

The most direct comparison is made between the density of the two fluids. MR fluid has a density of $3\,\mathrm{g/cm^3}$, where as typical hydraulic fluid ranges between 0,868 and $0{,}882\,\mathrm{g/cm^3}$ [20]. The dynamic viscosity is quoted in Table 1.1, and most hydraulic oils are given in kinematic viscosity which lie between 16 to 100 cSt [20, 21]. The kinematic viscosity of the MR fluid is found by converting the dynamic viscosity using Equation 1.1.

$$v_K = \frac{\eta}{\rho} \tag{1.1}$$

where

η = Is dynamic viscosity (Pa − s).
ρ = Is the density ($\mathrm{kg/m^3}$).
v_K = Is the kinematic viscosity (cSt or $\mathrm{mm^2/s}$).

The kinematic viscosity of the MR fluid is calculated at 30,6 cSt, which lies in the range of normal hydraulic fluids. The significant increase in density coupled with the alterable yield stress implies a bigger annular gap will be needed as calculated in Section 3.3.

1.3.3 Modelling

Conventional hydraulic fluid behaves as a Newtonian liquid, as shown in Figure 1.5. MR fluids are best described using a Bingham plastic model, since the fluid is

characterised by both yield stress and marginal viscosity [8]. In practice, the yield stress forms the main operational parameter.

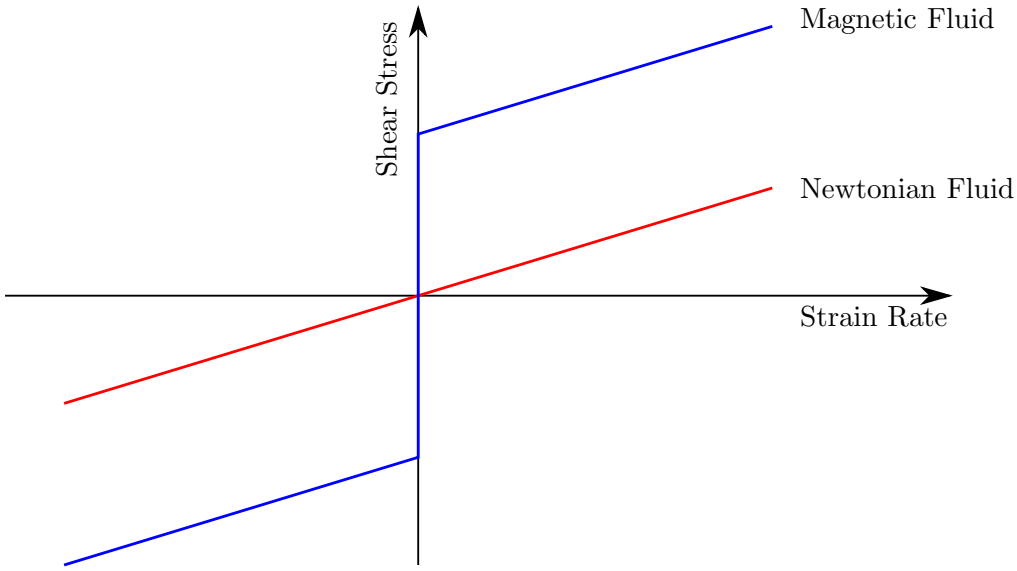


Figure 1.5: Newton model of fluid [7].

In accordance with the Bingham Model described, the total shear stress is described by Equation 1.2 [7]. The damper only operates in one direction during an impact, removing the need to mathematically incorporate direction in the equations describing the Bingham Model.

$$\tau = \tau_0(H)sgn(\gamma) + \eta\gamma \qquad |\tau| \ < |\tau_0| \tag{1.2}$$

$$\gamma = 0 \qquad |\tau| \ < |\tau_0| \tag{1.3}$$

where

τ_0 = Is the yield stress caused by the applied field.
γ = The shear strain rate.
H = The amplitude of the applied magnetic field.
η = Is the field independent post-yield plastic viscosity

The viscosity η is defined as the slope of the measured shear stress versus the shear strain rate, as illustrated in Figure 1.5. While the Bingham model is relatively simple to both understand and implement, it remains an effective model especially during the design phase of an MR damper [7]. This method is used in conjunction

with the parallel-plate model, as described in more detail in [7], to find the optimum annular gap (see Section 3.3).

1.4 Aims of Study

The aim of the project is to build a new technology which can address an under-development in the pile testing industry. By looking at what currently exists in combination with pile analysis techniques, the technology developed may contribute to the growth of this sector [4]. Specifically, a non-destructive method of rapidly loading a bearing pile is proposed.

The primary objective is to impact a pile with a predetermined force profile. The control of the impact is intended to put the entire pile into compression, which yields a simpler result in terms of analysis compared to multiple areas of compression and contraction throughout the length of the pile (see Chapter 2). Achieving this goal would create a new and relatively cheap method of testing piles which is unique to South Africa [4].

The type of test proposed falls into the category of Rapid Load Testing (RLT), which is one of the more attractive testing methods because of the cost efficiency, analysis reliability and total number of piles testable per day [4]. Another goal is to provide greater control and energy efficiency to the process, which would directly impact on the simplicity and accuracy of analysing the results of the testing procedure.

Chapter 2

FORMULATION OF THE PROBLEM

The problem is first defined by the rapid load test requirements and procedure. Similar tests are reviewed to both apprise current technology and to better define where the damper test fits in. The prototype damper provided was in its second revision, having had tests already performed with it. A methodology was followed to redesign this damper to use MR fluid, where the amount of work achievable is defined in the project scope.

2.1 Rapid Load Test (RLT)

While the actual RLT testing is to be done by the School of Civil Engineering at the University of the Witwatersrand using the adapted shock absorber, it is important to understand the link between the test and the damper. This link lies in the RLT analysis using a method which is called the "Unloading Point Method" in its basic form [4, 6, 22].

In order to use this method, the weight of the mass needs to be between 5 % and 10 % of the expected maximum operational load (as previously mentioned), and the time over which the force is applied must be long enough that the resulting wavelength of the force is greater than the length of the pile [4, 5, 23]. This has the affect of placing the entire pile in compression. The unloading point may then be evaluated from the penetration versus load graph as shown in Figure 2.1. The red line refers to the "derived static equivalent" response of the pile.

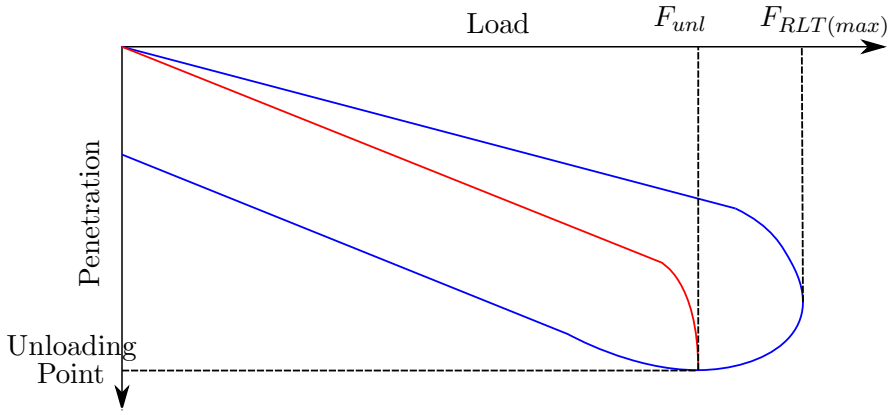


Figure 2.1: The RLT using the Unloading Point Method, adapted from [4, 24]

The shock absorber controls the time over which the total force is applied and the mass, together with the drop height, influences the total average force available. The total force applied to the pile (F_{RLT}) may be broken down into various components, as illustrated in Equation 2.1 [4, 6, 22].

$$F_{RLT} = F_S + F_V + F_E \tag{2.1}$$

where

F_S = The force from the static resistance of soil.
F_V = The force from soil due to high velocity pile movement
F_E = The force generated from the inertia of the pile

By monitoring the acceleration of the mass, it is possible to derive the applied force to the pile. Additionally, using the real-time information from the accelerometers, a control algorithm may be used to damp the falling mass. This has the affect of controlling the time over which the force is applied, making it possible to place the entire pile under compression. For further information about the Unloading Point Method, the interested reader may refer to [4, 6, 22].

2.2 Similar Tests

The shock absorber test is to be loosely based on two types of RLT's. The new test proposed has the goal of improving on the two technologies, with the added benefit of being specific to South Africa [4]. The two tests are the Statnamic testing method and the Fundex Pile Load test [3].

2.2.1 Statnamic test

The first test discussed is the Statnamic test, so called for its combination of the Static and Dynamic test procedures. The test apparatus is shown in Figure 2.2.

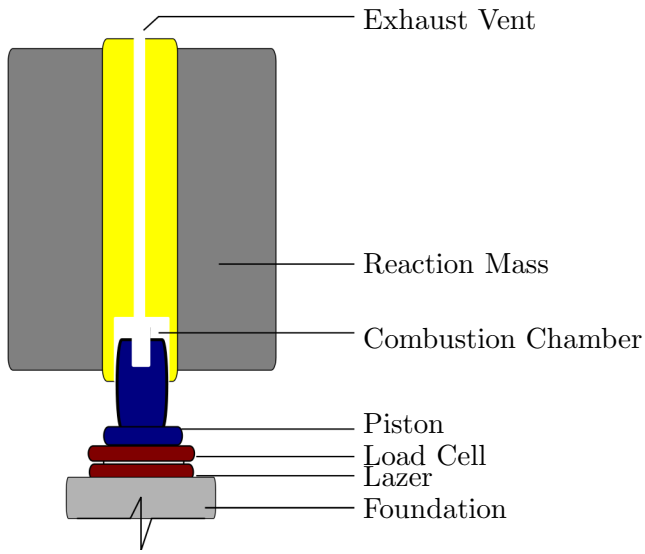


Figure 2.2: The typical Statnamic test apparatus, adapted from [5].

The Statnamic Test involves accelerating the reaction mass vertically skywards by means of a controlled explosion fed by rocket fuel [5]. Newton's second law of motion ensures that the upward force of the mass in turn causes a downward force on the pile. The control is performed by the fuel used, geometry of the combustion chamber as well as by venting gas [5, 6].

2.2.2 Fundex pile test

The second test considered is the Fundex Pile Test. Similar to the test proposed, the Fundex test also operates within the RLT requirements [3]. The falling mass is secured to robust springs which act to both cushion the reaction mass and prevents damage to the pile, as illustrated in Figure 2.3. The springs act to extend the force over a slightly longer period of time, similar to the damper proposed. The control for the Fundex test is instilled via the geometry and material of the springs and reaction mass.

The damper system proposed would operate similarly to the technologies described. Instead of springs, a damper will be used and instead of an explosion with venting,

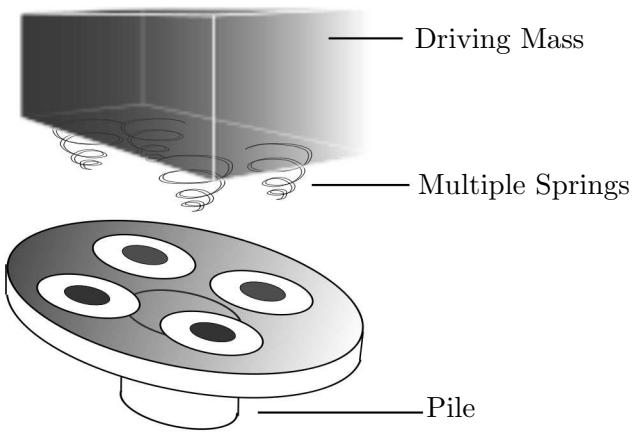


Figure 2.3: Concept behind the Fundex Pile Test [3].

the damper is to be controlled semi-actively by means of MR fluid [25–27].

2.3 Review of Work

The damper provided was tested previously using hydraulic fluid by the School of Civil Engineering. The results are summarised by Figure 2.4. The average force applied by the damper was calculated using Newtonian equations of motion [28]. The maximum force applied to the test material is 3,53 kN, which occurs at a drop height of 400 mm.

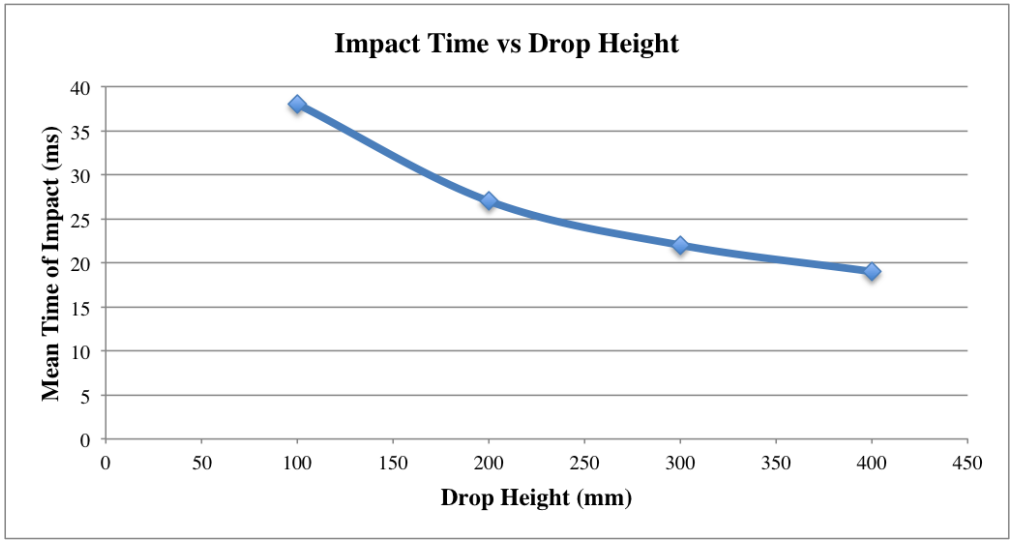


Figure 2.4: The results from the damper in its second revision.

The initial testing of the damper containing hydraulic fluid was dropped from a height of 100 mm to 400 mm. Approximately 18,5 mm of the piston's stroke was used, despite variations in drop height. The duration of the impact decreased for increased drop height. This result was expected since the velocity of the damper as it impacts is higher for increased drop heights.

The impact time is too short to fall in the RLT category. The impact time period does increase for decreased drop height, but reduces the applied force. If dropped from too low there will not be enough force to depress the piston. While it would be possible to use a damper with a different geometry, custom dampers would then have to be made for each test. By using MR fluid, it is possible to dynamically control the damper over the duration of the impact in terms of the instantaneous force applied and total impact time.

2.4 Methodology

The project was made manageable by creating several objectives which arise from the MR fluid requirements. The factors influencing the project are also discussed in terms of how they affect the design decisions and constraints.

2.4.1 Objectives

By using a controllable fluid inside the shock absorber, several problems are generated. MR fluid has different characteristics to hydraulic fluid and requires a magnetic field to change the fluid's properties. Electronic support for the magnetic field is therefore required. The project was broken into five objectives, each with their own criteria for success, which has been summarised by Table 2.1.

While the MR fluid has a viscosity comparable to that of hydraulic fluid (see Section 1.3), it is significantly more dense and exposing the fluid to a magnetic field will have the apparent effect of increasing the fluid viscosity. To accommodate these changes, the damper's annular gap required alteration with a coil placed inside the damper to generate the magnetic field.

Before the transducers may be implemented, they were first calibrated. The controller developed is used to monitor each transducer, with the ability to log data and serially communicate. Since the micro-controller can not directly generate any

Table 2.1: Project objectives and success criteria.

Project Objectives	**Indications of Success**	**Monitor and Evaluation**
Modify the damper's	A magnetic field inducing coil and wider annular gap	An appropriate dynamic response and controllable force
Interface and log the transducers	Serially transferable data with logging capabilities	Calibrated transducers that corroborate with each other
Develop a controller	Outputs a PWM signal	Correct operation of the driver circuit and data transmission to a PC
Develop a driving circuit	Switches a MOSFET which drives the coil	Alterable MR fluid yield stress
Implement a working algorithm	Accelerometers register the change in damping	Analysis of data from accelerometers

substantial current, a driving circuit capable of energising the coil is necessary to interface with the controller.

A basic algorithm was implemented on the controller to establish that the design is operational. Development of a control algorithm is beyond the scope of this project, and as such limited the maximum drop height of the experiments.

2.4.2 Factors influencing results

Certain design criteria were provided by the School of Civil Engineering [4]. As so far as the final experiment is concerned, the maximum height to be designed for is 2,5 m. Upon further discussion, it was decided that initial testing (without a control algorithm), was not to exceed 0,2 m.

The accelerometers and damper were both provided. This means that the damper design is limited to alterations only, and the accelerometers will only register accelerations below 70 g [29]. Regardless of this constraint, the accelerometers were investigated for appropriateness (see Section 5.1).

2.5 Scope

Much of the onus is on the School of Civil Engineering within the University of the Witwatersrand to develop the technology to completion. The scope of this dissertation is to optimise the prototype damper for use with the MR fluid and to create a measurement system capable of monitoring all the transducers, with the ability to control the damper.

Once the damper is developed, preliminary testing is to be performed on soft-board. No testing of piles is to be performed, and no analysis of the results or what the results may pertain to in terms of pile integrity is required.

In summary, the requirements are to alter the provided damper enough so that control may be established, then to create the necessary circuitry which will support the damper operations. No software user interface is necessary, and since the device is to be used in laboratories, it is assumed power may be obtained from a bench supply. To ascertain that the system operates satisfactorily, the final requirement is to monitor the transducers and manually adjust the damping during a few drop tests before surrendering the device to the School of Civil Engineering.

Chapter 3

DAMPER AND MAGNETIC CIRCUIT

Several factors affect the damping capability of the shock absorber. The damper geometry and design are first described as the shock absorber itself forms part of the magnetic circuit. By altering the annular gap between the piston and housing to accommodate the MR fluid, the properties of both the magnetic circuit and the dynamic range of the damper are simultaneously altered. Hence, finding the optimum dynamic range and controllable force is necessary for adequate control of the damper.

3.1 Damper

The shock absorber – or more accurately, the damper – is directly mounted to the falling mass with two accelerometers attached. In this way, both the damper and falling mass will experience identical accelerations, with the exception of the piston and internal fluid, during impact.

The design process started with the identification of the alterable parameters available. The basic damper unit supplied was pre-constructed for the same task, but without any adaptive control and an annular gap calculated for hydraulic fluid. Having a pre-constructed device placed constraints on the designer in terms of the damper type and materials used. This minimizes the design criteria to the:

- annular gap between the piston and the housing
- magnetic circuit

- internal fluid
- additional minor modifications and maintenance

Identifying the various parts of the shock absorber and materials allows the necessary calculations to be made for determining the annular gap and magnetic circuit. The MR fluid resource is limited and precautions, in terms of maintenance and safety, are critical.

3.1.1 Physical parameters

While a damper design may be very complicated, in terms of dimensional data, material specifications, performance and tolerances, the shock absorber itself is fairly standard [8]. All the parts and dimensioning of the damper were modelled in 3-D to both verify and communicate the design. The final model is shown in Figure 3.1, which compares the computer generated model as well as a photograph of the damper.

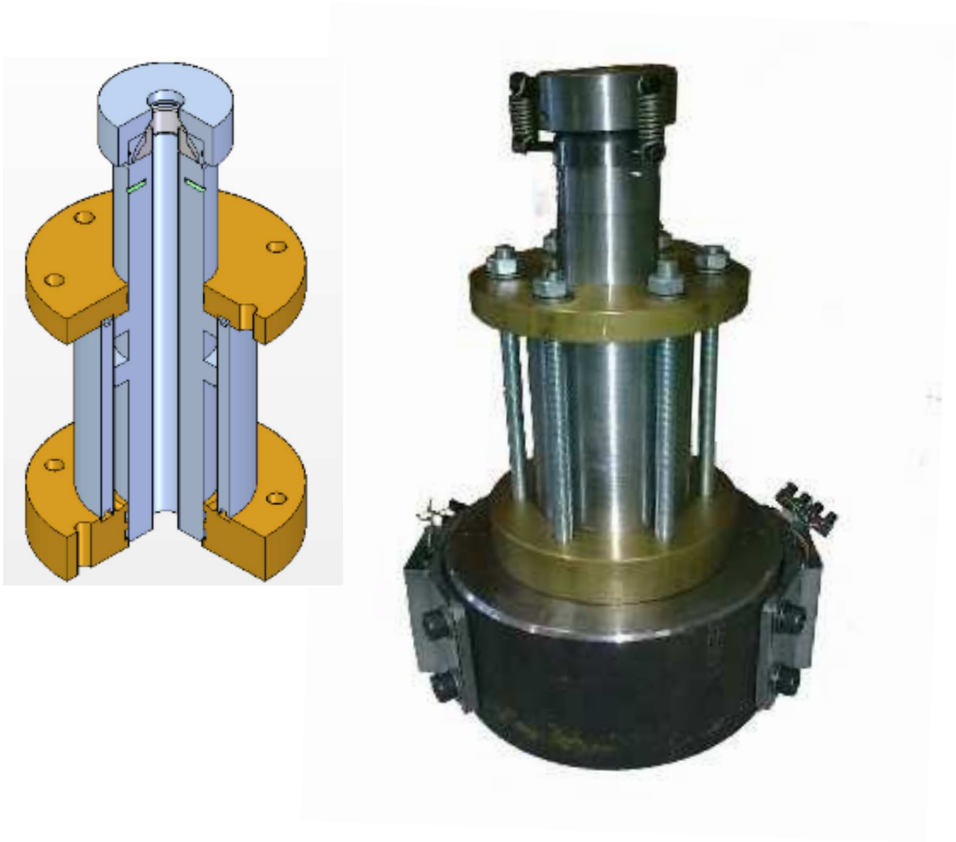


Figure 3.1: Isometric model view and photograph.

The damper is designed to be dropped directly on the floating bearing secured to the bottom of the piston. This bearing corrects for any slight miss-alignment between the pile and piston head, minimising damage to the pile head and damper. The stroke of the damper is 20 mm, due to the shoulders on the piston.

The piston is contained between two brass plates. The material chosen minimises the impact that the brass plates will play on the magnetic circuit as explained in Section 3.2. Between the two brass plates is the housing, which acts to both contain the magnetic fluid and forms part of the magnetic circuit. The cylindrical housing is made from mild steel. The exploded view in Figure 3.2 shows the interconnection between the various parts of the damper.

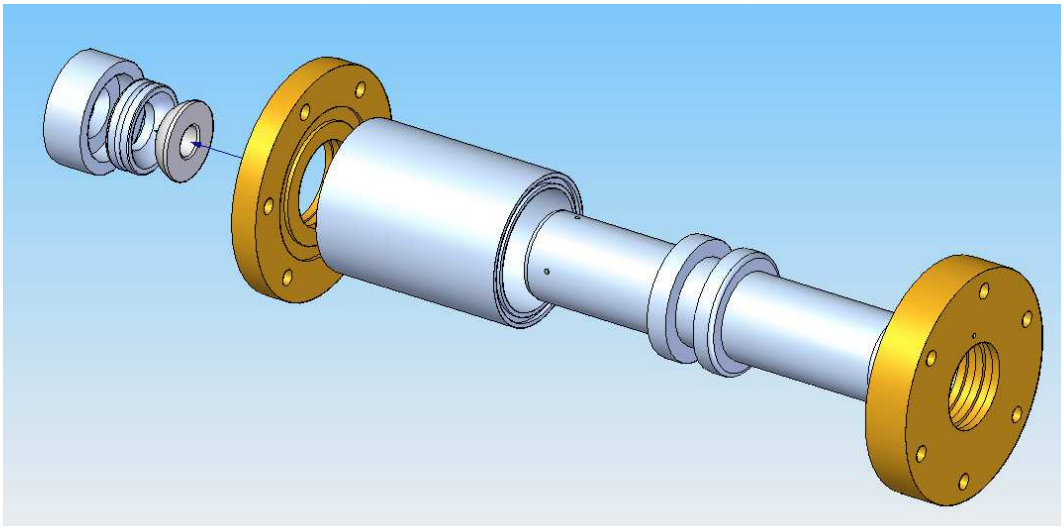


Figure 3.2: An exploded view of the damper.

The cavities between parts are where the o-rings and seals are placed to prevent the fluid from leaking out. The rubber seals introduce a lot of friction during operation, which is accounted for when the dynamic range of the damper was determined (see Section 3.3).

Between the lower extruded shoulder and the base of the damper there is a steel spring. The spring is present to return the piston to its original position after an impact has occurred and to apply a resistive force. Several other methods exist which would yield the same results, but a spring is robust, simple to implement and model [8].

The spring characteristics are illustrated in Figure 3.3, where the outer diameter is specified as D_{Out}, the metal diameter is d and the uncompressed length is L_{Free}.

The spring will never be fully compressed, as it is limited by the 20 mm stroke of the damper.

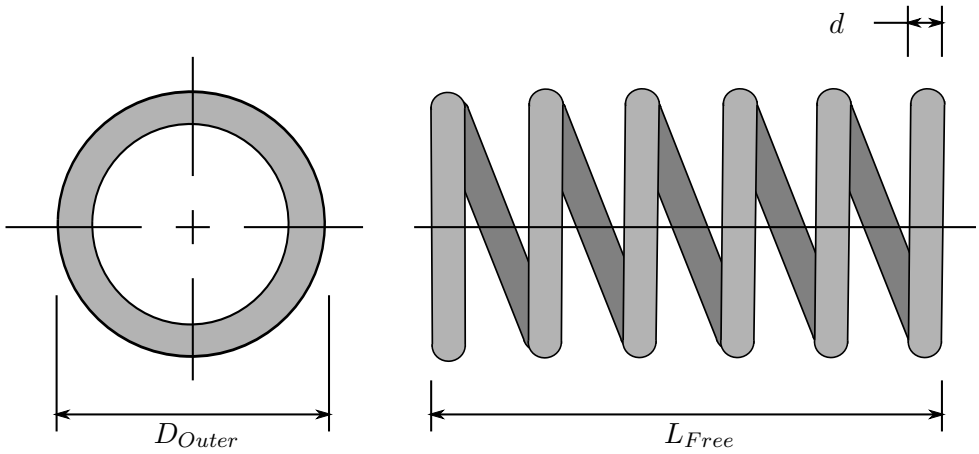


Figure 3.3: Annotated diagram of the spring.

Following from Figure 3.3, the specifications are summarised in Table 3.1. With these quantities the force generated by the spring may be quantified and used to estimate the dynamic response of the damper (see Section 3.3).

Table 3.1: Spring specifications.

Characteristic	**Quantity**
Outer Diameter D_{Out}	51,35 mm
Wire Diameter d	3,20 mm
Free Length L_{Free}	66,00 mm
Active Coils	3 Coils

The annular gap is formed between the protrusions on the piston and the housing of the damper. The original size of the gap is 0,3 mm, by increasing the gap between the piston and housing, the dynamic range of the damper was altered to better suit the fluid used (see Section 3.3). Figure 3.4 shows a cross-section view of he damper to better illustrate the annular gap.

The volume of fluid which is controlled by the magnetic circuit lies predominantly in this gap. While this volume is small at any one time, a fair amount of MR fluid

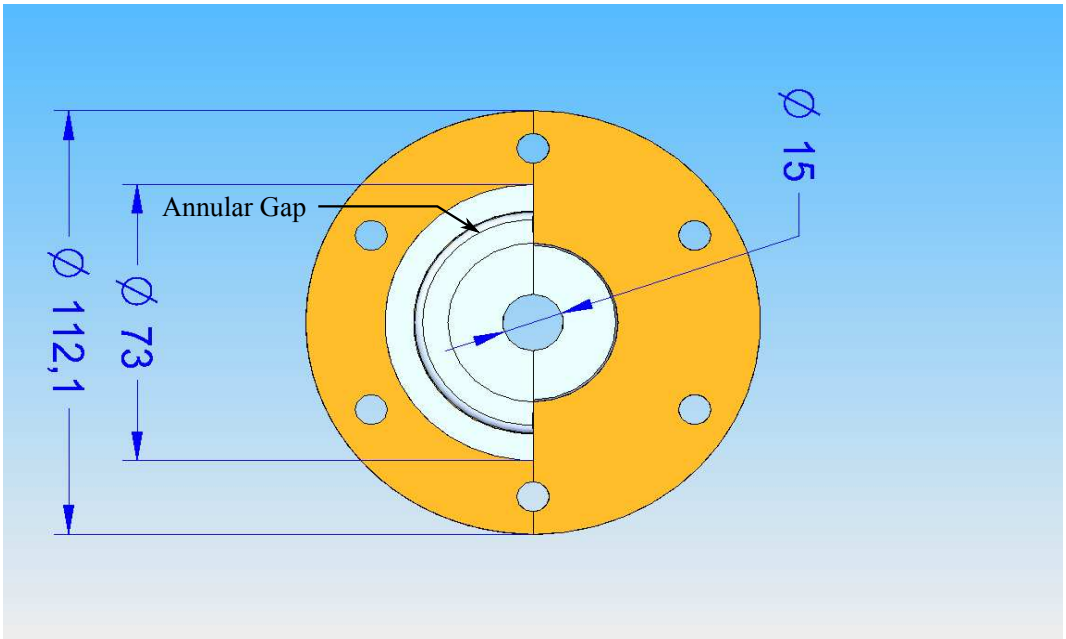


Figure 3.4: Half cross-section of the damper viewed from the top plane.

is still necessary so that the life span of the MR fluid does not become a limiting factor [8].

A 10,2 kg mild steel mass has been secured to the damper by means of threaded grooves and bolts. The weight of the mass is chosen according to the desired amount of force applied to the pile head. Including the body of the damper, the maximum force apply-able is approximately 105 N. This mass is often referred to as the "Driving Mass", and is chosen based on the pile and type of test to be applied [3, 30].

3.1.2 Operation

The shock absorber is operated by positioning the driving mass on top and the floating bearing towards the test pile or soft-board. A guiding rod is used to keep the damper vertical when dropped. When the damper is in contact with the test material, the piston will move into the housing as illustrated in Figure 3.5.

During this period is when controlling the fluid affects the experiment in terms of the amount of damping experienced and consequently the force applied to the test material. Ideally a constant force for 50 ms is desired as this emulates placing a pile into full compression as discussed in Section 1.2.

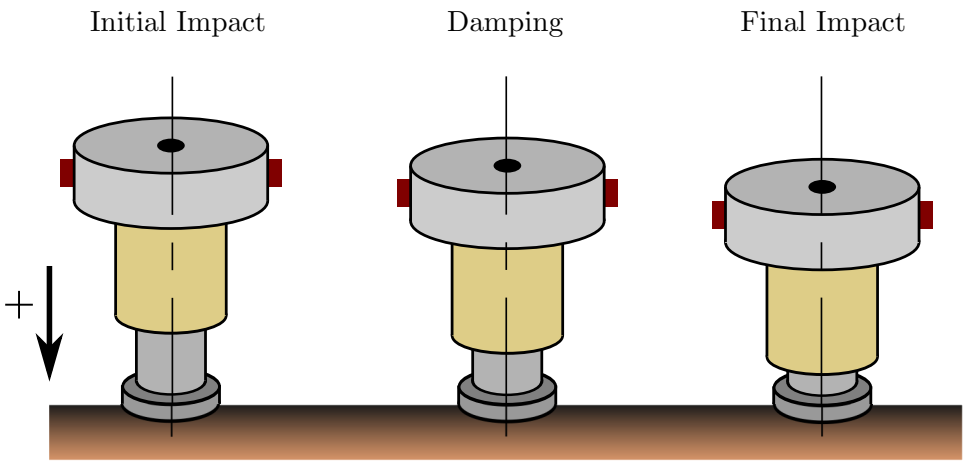


Figure 3.5: Operation of the damper as it impacts with the test pile.

3.1.3 Maintenance and construction

In order to work on the damper, as is needed when machining the annular gap or replacing the fluid, it is necessary to disassemble the damper. The damper may be dismantled using the following steps:

1. Remove the three bolts connecting the damper to the mass
2. Place the damper upright in a tray
3. Unscrew the nuts and remove the remaining three bolts
4. Carefully remove the bottom brass plate
5. Drain the contained fluid

To prevent leakage during disassembly, the housing is sealed with silicone to the top brass plate. During reassembly, any damaged seal or o-ring is to be replaced. The bottom plate has a grommet that may be removed to allow trapped air out of the system. The maximum expected pressure in the system is 108,3 kPA based on Equation 3.1 [28].

$$P_0 = \frac{F}{A} + \frac{1}{2}\rho v^2 \tag{3.1}$$

Where P_0 is the total pressure, which is made up from static pressure which is force F divided by area A, and dynamic pressure calculated from viscosity ρ and velocity v. The pressure in the system dictates what precautions are necessary to avoid leaking. The useful life of a damper is heavily affected by leaking due to seal wear [8].

The damper has no surface finish or corrosion resistance, so environmental moisture should be avoided [8]. Care must be taken when handling the MR fluid, as specified by the fluid safety guide [31]. This includes operating the device where there is good ventilation and avoiding skin and eye contact. The MR fluid must be shaken after long periods of standing, as the heavier particles settle to the bottom.

3.2 Magnetic Circuit

The magnetic circuit focuses on controlling the MR fluid within the damper. This is accomplished by developing sufficient magnetic flux density (B) in the fluid to alter the yield stress (H). The curve for yield stress versus the magnetic field strength may be viewed in Section 1.3. By analysing the magnetic system, an appropriate number of coils for a given annular gap at a rated current was found.

3.2.1 Operation

A typical bench power supply can provide 3 A of current from a single channel. Taking safety into account, along with space limitations inside the shock absorber, the appropriate wire size is 0,129 mm^2. This allows up to 3,7 A to be safely supplied, whilst being thin enough for future experimentation with two coils in the damper chamber.

Since the coil is controlled with a PWM signal (see Section 4.2), the fluid is best operated at maximum yield stress and lowest possible magnetic flux density. Using the technical data-sheet supplied by Lord Inc. [16], the MR fluid (*MRF-132DG*) yield stress saturates for field strengths (H) greater than 300 kAmp/m, which occurs at a flux density of 1 T. Using the curve of flux density versus field strength, the relative magnetic permeability (μ) for the MR fluid is calculated using Equation 3.2.

$$\mu = B/H \tag{3.2}$$

Using the above mentioned as part of the design parameters, the magnetic calculations are used to design the coil [32]. The response of the system is also predicted, using the magnetic model, for different power supply amounts.

3.2.2 Magnetic model

Generating a magnetic field in the annular gap, containing the MR fluid, changes the yield stress of the fluid. By applying a magnetic field, the magnetic particles suspended in the fluid align, which changes the damper's stiffness (refer to Section 1.3). The magnetic model was developed by looking specifically at the area between the two shoulders of the piston, which is directly affected by the magnetic circuit, as shown in Figure 3.6.

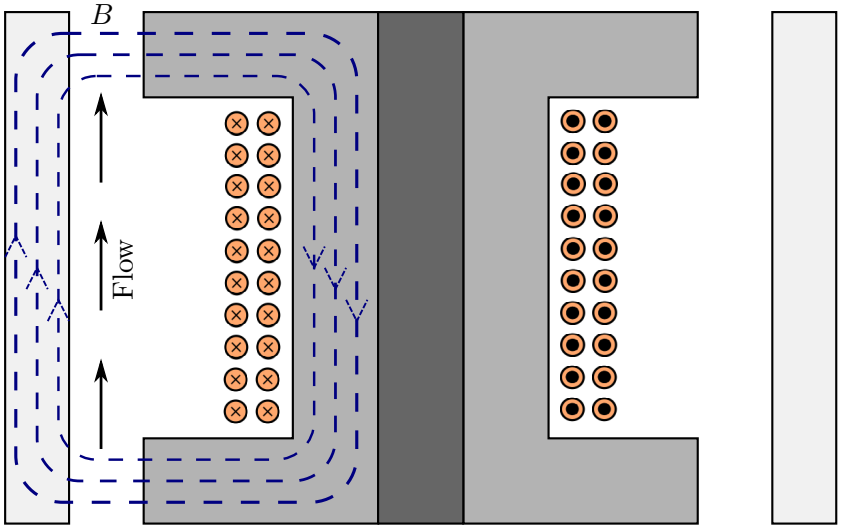


Figure 3.6: Cross-section of the magnetic circuit region.

The MR fluid surrounds the central piston. Recalling that the housing and piston are both fabricated from mild steel, the flux path will follow the dashed blue path illustrated on Figure 3.6. The top and bottom plates of the shock absorber are brass, forcing the vast majority of the flux to pass through the fluid gap with minimal fringing and flux leakage.

Ignoring fringing and using an axis-symmetric approach, the magnetic circuit may be simplified to the equivalent magnetic circuit in Figure 3.7. Since there are no air gaps to dominate the system, the reluctance of both the damper housing and piston are significant.

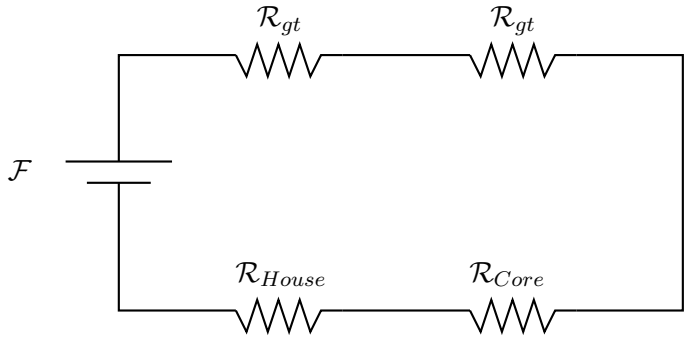


Figure 3.7: Equivalent magnetic circuit model.

Following the path shown in Figure 3.6, there are two "gaps" which are represented in Figure 3.7 by the two reluctances $\mathcal{R}_{gt}$. Both the core and housing generate their own reluctance, shown as $\mathcal{R}_{Core}$ and $\mathcal{R}_{House}$ respectively. By considering the axis-symmetric nature of the damper, the reluctances were evaluated using Equation 3.3 [32].

$$\mathcal{R} = \frac{l}{\mu \times A} \tag{3.3}$$

Using the magnetic equations mentioned in conjunction with the axis-symmetric approach, the reluctances were calculated and are tabulated in Table 3.2.

Table 3.2: Worst case magnetic circuit parameters.

R_{House}	1,695×10^4 AT/Wb
R_{Core}	3,886×10^4 AT/Wb
R_{gt}	1,983×10^4 AT/Wb
No. of Turns	240 T
Current (I)	3,7 A
MMF ($\mathcal{F}$)	703 AT

From the magnetic circuit model, the relationship between the number of coils and the magnetic field stress is shown in Figure 3.8, assuming the highest possible load current and largest gap size.

From Figure 3.8, A flux density of 1 T occurs when there are 240 coils. Designing the coil for the worst case specification impacts on testing, since a smaller gap size would

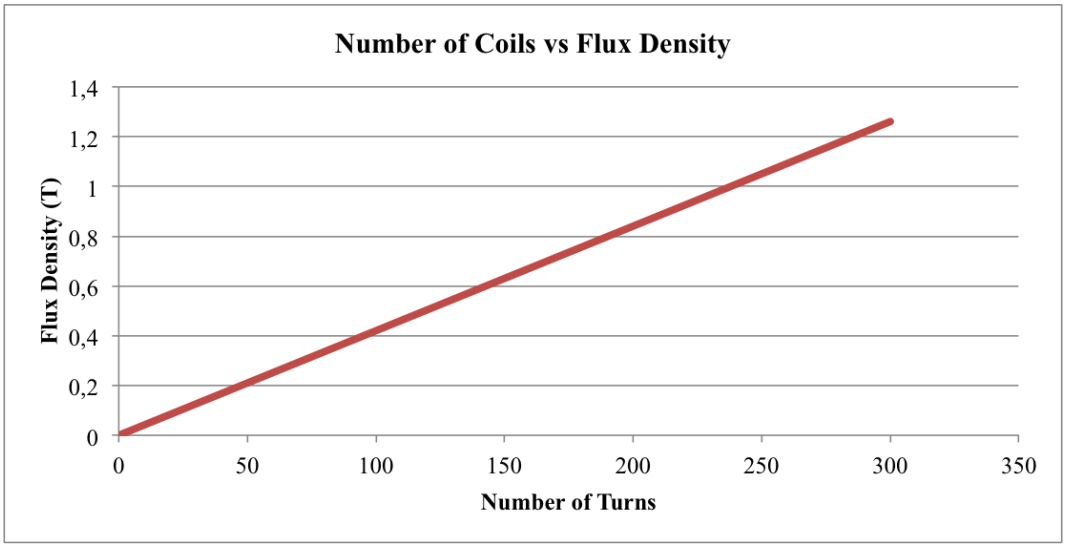


Figure 3.8: Number of turns versus the flux density in the gap.

require less current to achieve the same magnetic flux density. This is illustrated in Figure 3.9, which starts with the initial gap size of 0,3 mm.

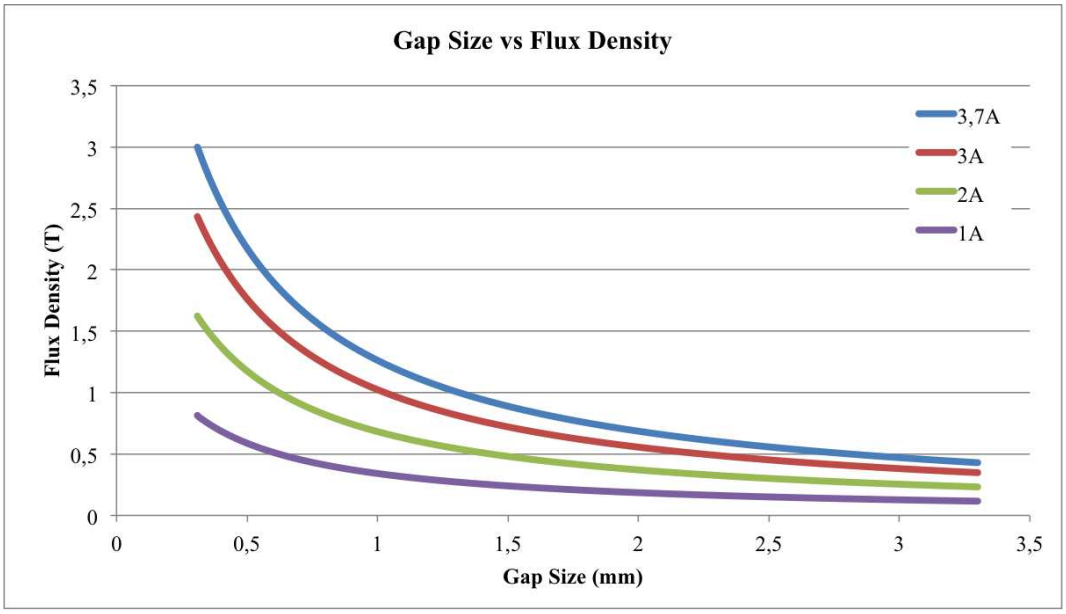


Figure 3.9: The relationship between the gap and current for the installed coil.

The initial current requirement of the damper is 1,3 A for a gap size of 0,3 mm. The annular gap was increased to 0,6 mm, which requires 2 A to saturate the fluid (see Chapter 7). The wire thickness is chosen based on the worst case annular gap size, which demands a current of 3,7 A.

3.2.3 Final coil design and placement

Copper wire was chosen to minimise the impedance and thickness of the coil. The installed coil is shown in Figure 3.10, where it is wound around the piston. The green and white insulated wires shown is the thermocouple cable, used to monitor the temperature of the fluid (see Section 5.2).

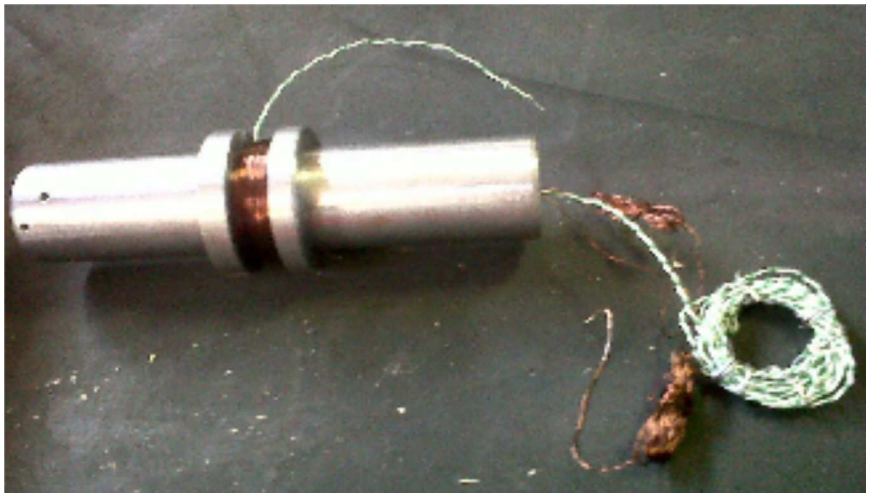


Figure 3.10: Photograph of piston with wound coil and thermocouple cable.

The coil properties have been summarized in Table 3.3. When designing the coil, care must be taken not to use too many turns, as the time to establish the desired current in the coil is approximately directly proportional to the number of turns in the coil and the applied voltage [7].

Table 3.3: Coil design parameter.

Parameter	**Value**
Number of Coils	1
Number of Turns	240
Wire Diameter	0,7239 mm
Coil Inner Diameter	42 mm
Coil Outer Diameter	43,5 mm

The inner and outer coil diameter refers to the amount of space taken up inside the damper, around the piston. The wire used for the coil has the narrowest diameter possible for the maximum current required. This ensures ample space in the cavity for the installation of a second coil for possible future testing. The entry hole would

have to be widened to gain access to the second coil, which would increase the risk of fluid leaking.

The entry whole is sealed with a strong epoxy resin. The same resin is used to ensure all the wires connected to the damper are in place with minimal risk of damage to the insulation. Additionally, insulation tape is used on the piston, between the two shoulders, to prevent any possible short circuit to the device.

3.2.4 Equivalent circuit model

The equivalent circuit model of the coil is shown in Figure 3.11. The equivalent coil resistance R_{Coil} and coil inductance L_{Coil} measures at 4,8 Ω and 40 μH respectively. The resistance measured is similar to the estimated resistance of 4,017 Ω using the wire impedance of 133,9 Ω/km with a length of approximately 30 m.

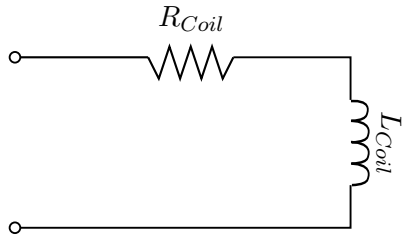


Figure 3.11: Equivalent circuit of the coil.

By simulating the coil and driver circuit (see Section 4.2), it was found that an applied voltage of 12 V over the coil is high enough to generate a 1 T magnetic field in the annular gap containing MR fluid, provided the coil is operated at 20 kHz with a 50 % duty cycle.

3.3 Annular Gap

The shock absorber provided was originally designed to operate using hydraulic fluid. By replacing the hydraulic fluid with MR fluid, the performance of the shock absorber was expected to change considerably. Without a major structural change in the absorber design, there are few ways to adapt to this change in function. The most accessible and influential alteration to make is to widen the annular gap between the piston and housing.

While this process can be done iteratively by gradually machining the piston and performing experiments, there are several drawbacks to this approach. Most importantly, the amount of MR fluid was limited, and potential loss becomes significant when the damper is continuously dismantled. Also, without a guide to where the optimum performance may be, it is likely that the piston shoulder would be over machined, causing irreparable damage.

To avoid the issues mentioned previously, the annular gap was analysed from a quasi-static approach. Using the following three assumptions, a quasi-static model was developed that describes the dynamic response of the shock absorber:

1. The MR damper moves at a constant velocity.
2. The fluid flow is fully developed.
3. The Bingham plasticity model of MR fluid applies.

An accurate method of modelling the damper involves using Navier-Strokes equations with an axis-symmetric approach [7]. This method is unduly complicated and has been shown to be closely approximated by the Parallel-plate method by [7].

3.3.1 Parallel-plate model

The problem is again looked at from the magnified perspective of a section of the gap. Since the ratio between the diameter of the shock absorber and the annular gap is small, it may be approximated as a parallel duct as shown in Figure 3.12.

Taking advantage of the axis-symmetric nature of the damper, the relationship between the dimensions mentioned in Figure 3.12 may be evaluated in terms of the shock absorber dimensions. Hence, the parameter h becomes the gap width $(R_2 - R_1)$, the width w is $\pi(R_1 + R_2)$ and L is the height of the shoulder on the piston.

3.3.2 Dynamic range and controllable force

By further developing the parallel-plate model, the two most important parameters for evaluating the dampers may be mathematically described. These parameters are

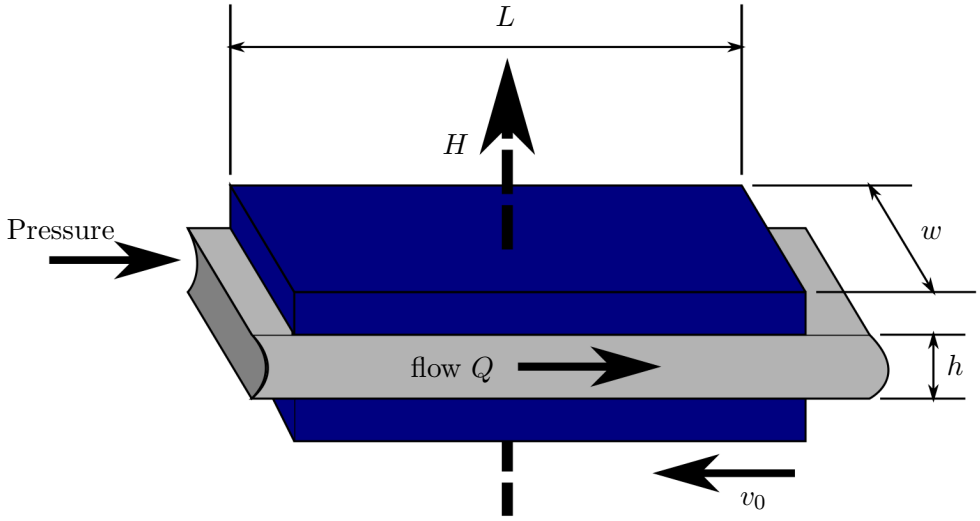


Figure 3.12: Behaviour of MR fluid through a parallel duct, adapted from [7].

the controllable force (F_{uc}) and the dynamic range (D) [7, 8]. The shock absorber resisting force may be split into a controllable force F_τ and an uncontrollable force F_{uc} which is made up of the viscous force F_η and the friction force F_f [7]. The decomposition of forces is shown with respect to the velocity of the duct (v_0) in Figure 3.13.

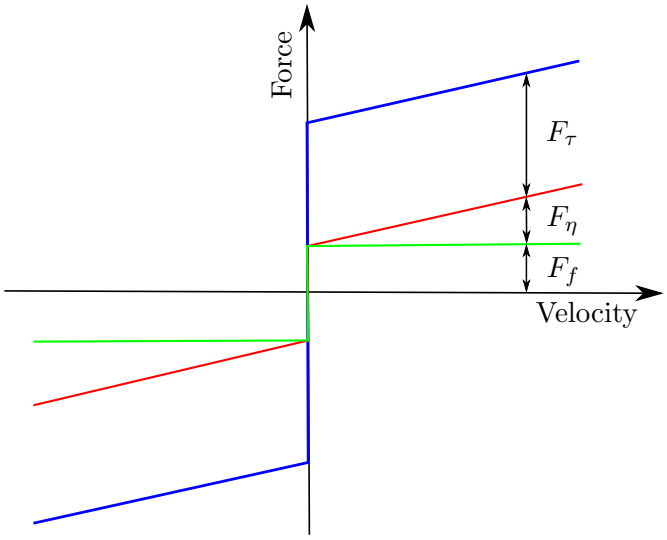


Figure 3.13: Decomposition of forces in an MR fluid, adapted from [7].

The ratio of the resisting force F with F_{uc}, defines the dynamic range (D) [7]. This is illustrated mathematically in Equation 3.4.

$$D = \frac{F}{F_{uc}} = 1 + \frac{F_\tau}{F_\eta + F_f} \tag{3.4}$$

Where F_η is the force due to the viscosity of the MR fluid. Both F_η and F_τ are evaluated using the parallel plate model to give Equations 3.5 and 3.6.

$$F_\eta = \left(1 + \frac{whv_0}{2Q}\right) \times \frac{12\eta QLA_p}{wh^3} \tag{3.5}$$

$$F_\tau = c\frac{\tau_0 LA_p}{h} \tag{3.6}$$

The dimension parameters are described in Figure 3.12. The surface area A_p is defined as the length L of the duct multiplied by the width w. The parameter τ_0 is the controllable yield stress of the fluid, and the parameter c is described by Equation 3.7.

$$c = 2.07 + \frac{12Q\eta}{12Q\eta + 0.4wh^2\tau_0} \tag{3.7}$$

Where η refers to the viscosity of the fluid. Concatenating Equation 3.6 with 3.7 yields the controllable force Equation 3.8.

$$F_\tau = \left(2.07 + \frac{12Q\eta}{12Q\eta + 0.4wh^2\tau_0}\right)\frac{\tau_0 LA_p}{h} \tag{3.8}$$

It becomes immediately apparent from Equation 3.8 that the controllable force is inversely proportional to the gap size, which relates to the parameter h [7]. To optimise the damper, there is a trade-off between the controllable force and the dynamic range. The smaller the gap size, the more control but less dynamic range. Conversely, the larger the gap the more dynamic range and less control. Too much gap and both dynamic range and controllable force diminished.

3.3.3 Discussion of the results

Given the equations discussed, the best method of finding the optimum gap is to input all the parameter data available and vary the gap size until the optimum point is found. Several assumptions were made to do the calculation. These include:

- velocity (v_0) is the final velocity of the worse case test conditions.
- uniform fluid flow for calculating flow rate.
- MR fluid is operating in the plug flow region.
- the majority of the friction force originates from the spring.

With the above assumptions, the flow rate Q may be calculated. Starting with a gap size of 0,3 mm, which is the original gap size, the gap is increased by 0,1 mm increments. The resulting graph is shown in Figure 3.14.

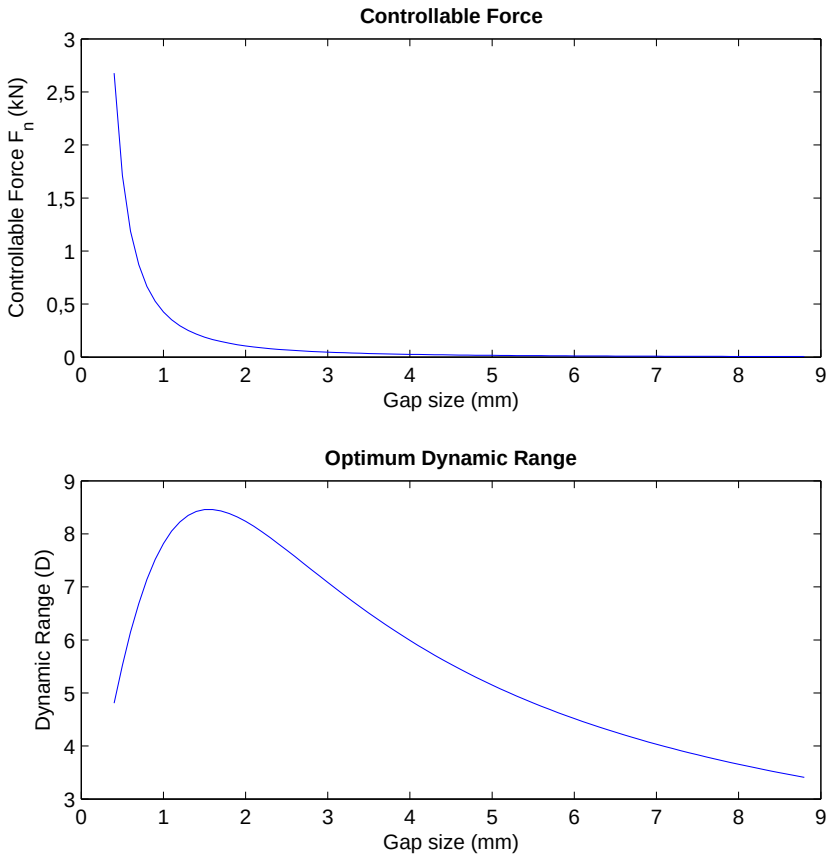


Figure 3.14: Modelled response of shock absorber for a change in gap size.

From the graph, the optimum point for dynamic range is at approximately 1,3 mm. This gives a dynamic range of 8,2 D and a controllable force of 300 N. The driving mass is approximately 102 N, which is comparable to the predicted controllable force. With the gap size calculated, compression of the fluid should be reduced such that the damper does not respond rigidly during the start of an impact.

Since this gap size is relatively large compared with the original gap size, the simulations for the magnetic circuit are done with the calculated gap size as the worse case scenario. The last experiments performed on the damper were done with an annular gap size of 0,6 mm because the controllable force is higher and the current requirements are lower. The smaller gap size still has a high enough dynamic range of approximately 5 D and a much larger controllable force of approximately 1,5 kN. Further widening of the annular gap is not explored due to the limited MR fluid.

3.4 Conclusion

The mass is securely bolted to the damper, which was first described in terms of the dimensions and operation to build an understanding of the damper mechanics. With this understanding, the limitations on coil design and consequently the driving circuit became apparent. The physical dimensions also affect the damper's performance, which impacts on the controllable force of the damper. Proper maintenance was also briefly discussed to both preserve the quality of the damper, as well as to preserve the MR fluid.

The damper was altered from hydraulic fluid to MR fluid so that it could be controlled by exploiting the properties of MR fluid, which stem from the suspended magnetic particles in the fluid. The fluid is operated in shear mode, between the piston and the housing. This space is referred to as the "annular gap". Between the two shoulders of the piston is where the coil for generating the magnetic field resides. The magnetic modelling and annular gap analysis take into account the fluid characteristics (specifically its density and changing yield stress with an applied field) in conjunction with the intended shear mode operation.

The optimum annular gap size is based on the balance between the peak dynamic range and the controllable force. With the evaluated gap size, the shock absorber has enough controllable force to cushion the falling mass, whilst having sufficient dynamic range to avoid issues such as fluid compression during an initial impact instead of flowing through the annular gap. The gap was machined wider to improve the dynamic response of the damper. The controllable force of the damper came into effect when controlling the fluid using the developed circuits.

Chapter 4

CONTROLLER AND DRIVER CIRCUITS

There are three transducers used to monitor the damper. In order to both monitor the sensors and to change the yield stress of the MR fluid, two circuits were designed. The controller circuit samples the transducers and outputs digitally, while the driver circuit supplies current to the coil. In order to minimise damage to these circuits and to simplify their use, both circuits are packaged with appropriate ports.

4.1 Controller Circuit

The controller is the central unit that does all the collecting, processing and outputting of data. It interacts with the analogue world by sampling and converting signals from the transducers, and outputs an appropriate PWM signal for the driver circuit. The controller was used for both calibrating the accelerometers and controlling the final adapted damper. This was done by taking advantage of the controller's ability to operate from portable power and by either storing or transmitting data. A photograph of the controller is shown in Figure 4.1.

4.1.1 Functional overview

A high level functional diagram representing the functions of the controller is given in Figure 4.2. The blue blocks on the left represent the inputs into the controller, and the green blocks on the right are outputs. The complete circuit diagram for the micro-controller circuit is given in Appendix A.

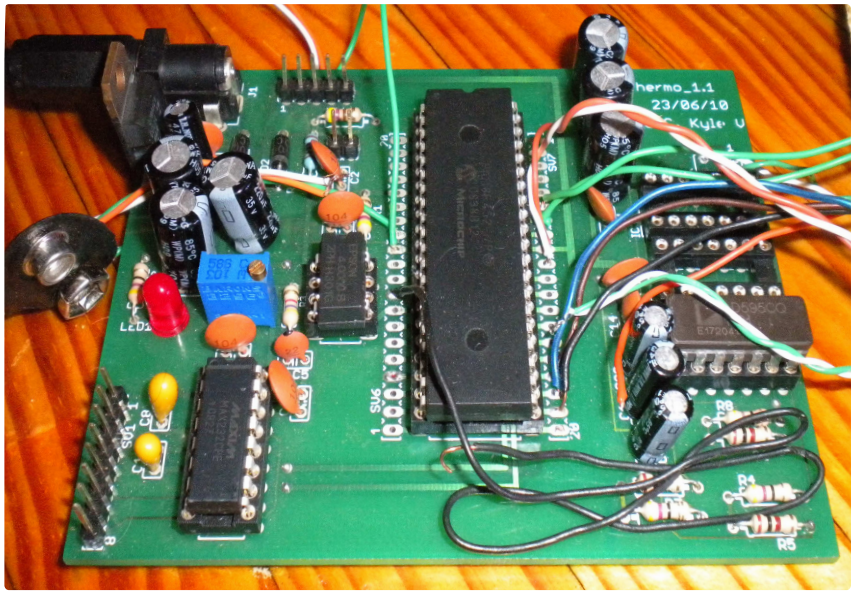


Figure 4.1: Photograph of the controller unit, showing the populated PCB.

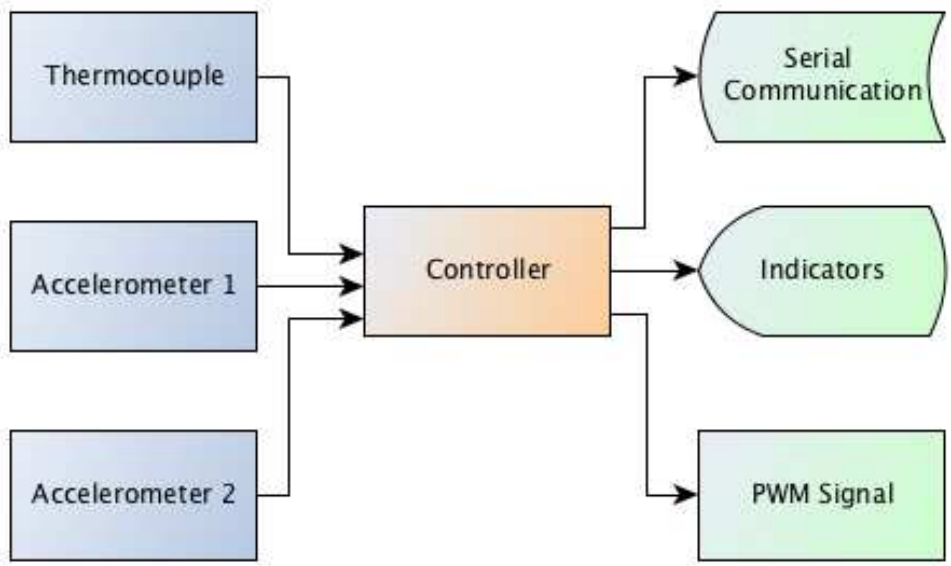


Figure 4.2: Controller functional overview block diagram

Each transducer is calibrated so as to minimise the error. The accelerometers are described in detail in Section 5.1, and the thermocouple is similarly described in Section 5.2. Discussed here is how the transducers interface with the controller.

The thermocouple instrumentation amplifier *AD595CQ* operates in conjunction with a K-Type cable to give a signal of 10 mV/°C. Since the temperature of the system is expected to change over seconds, a first order, low pass filter with a cut-off of

20 Hz is chosen such that the error from the filter is less than 0,1 % at a sampling frequency of 1 Hz. The transfer function of the filter is given in Equation 4.1.

$$H_{thermo}(\omega) = \frac{1}{1 + \frac{j\omega}{132.98}} \tag{4.1}$$

A 160 Ω series resistance with a 47 μF shunt capacitor achieves the desired transfer function $H(\omega)$. The transfer function has the frequency response depicted in Figure 4.3.

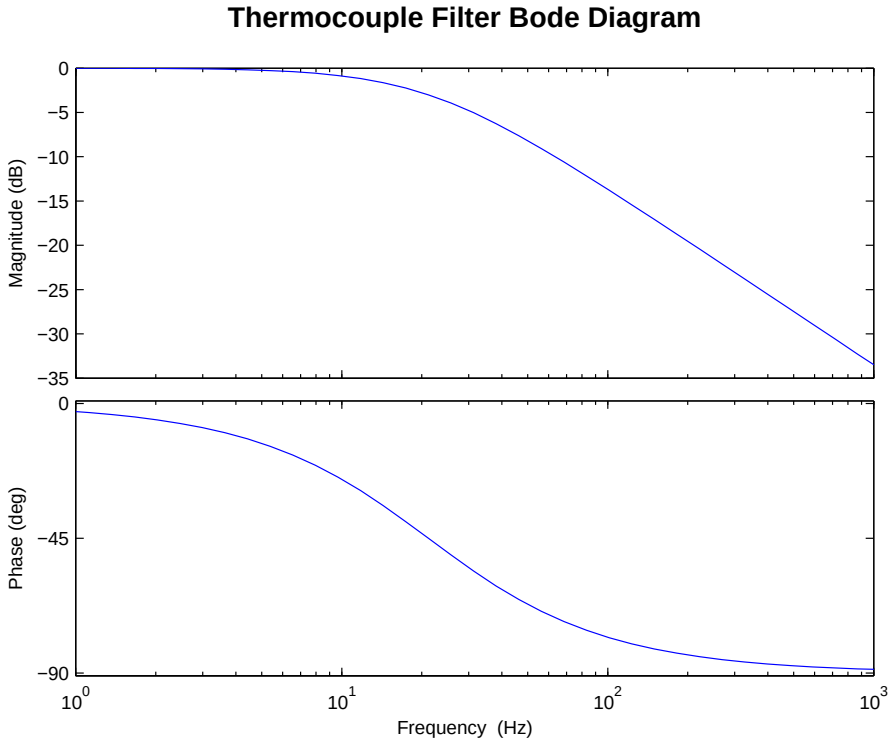


Figure 4.3: Bode diagram of the thermocouple filters.

The filtered thermocouple signal interfaces with analogue port *AN0* on the PIC micro. Similarly, each accelerometer signal is filtered and given an ADC port on the micro-controller. Accelerometer 1 uses *AN5* (pin 8), and Accelerometer 2 uses *AN6* (pin 9). A first order filter is used with the transfer function shown in Equation 4.2.

$$H_{acc}(\omega) = \frac{1}{1 + \frac{j\omega}{3030.30}} \tag{4.2}$$

This type of filter was used because each accelerometer has a Bessel Filter with a $-3\,\mathrm{dB}$ frequency response of 400 Hz. So the first order filter is there primarily to attenuate noise induced along the signal transmission lines. The Bode diagram for the first order accelerometer filters are shown in Figure 4.4.

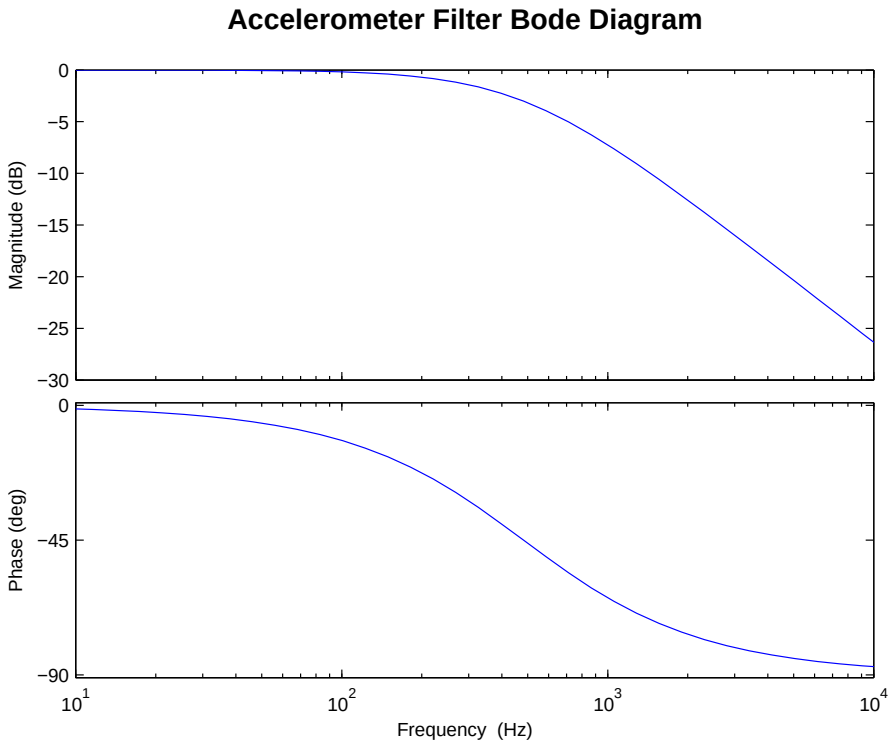


Figure 4.4: Bode diagram of the accelerometer filters.

One of the primary forms of communication between the controller and the user is done via a serial protocol. Header pins on the edge of the board allow a user to connect to the serial communications by means of an adapted DB-9 cable using a null modem arrangement. With the controller in its packaging, the serial communications are easily accessed from a DB-9 socket. To enable the micro to communicate via RS-232, a 5 V driver and receiver unit was installed. The *MAX232CPE* by Maxim fills this function [33].

The RS-232 chip has several attractive features including a typical data rate of 120 kbps with 10 ns propagation delay [33]. Each time a transducer transmits, it sends a word length of 16 bits plus one 8 bit character. Since the two accelerometers are monitored with speeds relative to the time span of the impact, with intermittent thermocouple readings, there must be a minimum bit rate of 29 kbps to get a sampling rate of 600 Hz for real-time data transfer.

The data is in fact sampled at double the minimum sampling rate (58 kbps), which falls within the allowable transfer rate. The *MAX232CPE* also has the advantage of being both a receiver and transmitter of RS-232 communications. This feature may be useful for future applications.

In addition to serial communication, certain data is best represented visually and without requiring a computer and interpretation. This includes warnings and verification that data has been logged. The microprocessor is configure to output a low (0 V) when outputting a warning. One of four LEDs will respond as in accordance with Figure 4.5.

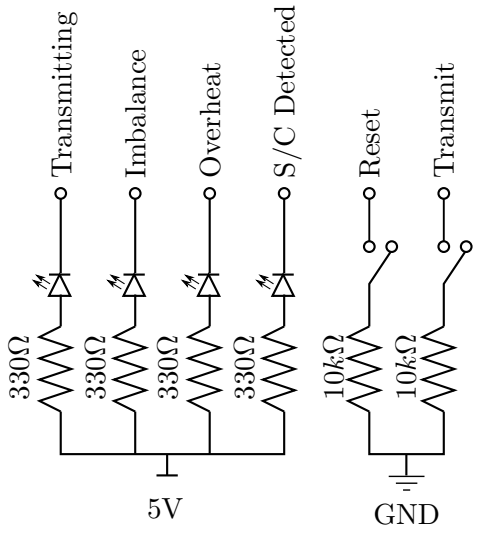


Figure 4.5: Pull-up LED indicator circuit.

The function and placement of the LED indicators are described in more detail in Section 4.3. Two push buttons have also been included and served various functions during the design phase, but were assigned as a reset and data transmit in the final package.

The PWM output from the controller is taken from the controller board and fed to the driver circuit. The following two attributes of the PWM signal may be altered by the controller and the controlling algorithm:

1. The PWM period
2. The PWM frequency

This is done by writing to the Timer 2 pre-scale value, the *CCPR1L* register and to the *CCP1CON* bits [34]. Several other features are included in the controller design in order to adequately operate the damper.

4.1.2 Controller features

The development board has been simplified by the block diagram shown in Figure 4.6. Each block represents a function of the PCB. Starting with the orange block at the centre, the *PIC18F452* forms the central processing unit (CPU) [34].

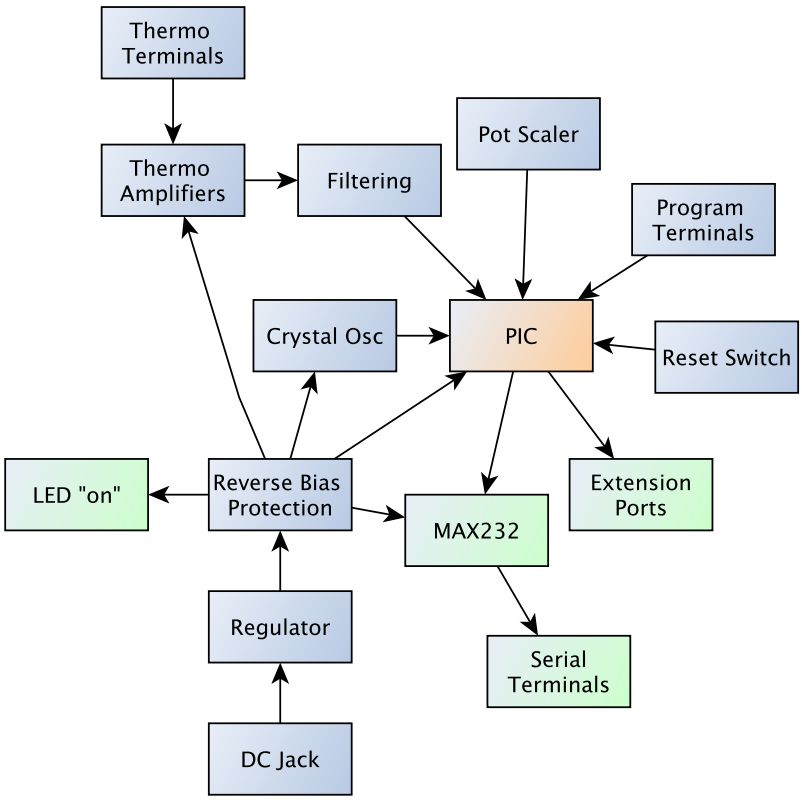


Figure 4.6: Block diagram representation of the controller functions.

Availability and cost are the first motivating factors for this particular chip. Also, the chip was selected for its ability to support the functions shown in Figure 4.6. These functions include:

- 1536 bytes on chip RAM
- 8 bit programmable pre-scaler

- 10 bit ADC ports, fast sampling rate, linearity of $1LSb$
- PWM output, resolution of 1 to 10 bits
- Addressable USART module
- In-Circuit Debug (ICD)
- Low power, high speed FLASH

To power all the digital devices, a 9 V DC jack is provided. The jack terminals are connected to a *L7805CV* regulator, which may be supplied with 8 V to 30 V [35]. Since the board is often supplied by a bench supply, reverse bias protection is necessary. This feature has been inadvertently tested on multiple occasions. An LED lights up when the board is adequately powered.

Originally, the reset feature was designed as a push button on the board. This was replaced with two terminals, such that the button may be located remotely on the external packaging (see Section 4.3). Several features of the chip are accessible externally via terminals. It is through these terminals that the micro may be programmed using an *RJ-12* cable, making the controller a completely independent development board. In order and with the corresponding *RJ-12* colour, the programming pins are:

1. Programming Clock (PGC) - Yellow
2. Programming Data (PGD) - Green
3. Ground (GND) - White
4. 5 V Supply (V_{DD}) - Black
5. Memory Clear (MCLR) - Blue

The clock signal is provided externally from a 5 V TTL clock oscillator with a frequency of 4 MHz. The clock oscillator is placed as close to the micro as possible to ensure no high frequency issues. By having an external clock input, timing stability is ensured.

A 10 kΩ POT scaler connects to the positive voltage reference on the PIC for adjusting the ADC sensitivity. A draw back of using the potentiometer is that the voltage value drifts when the supply voltage changes. This may happen when

operating off batteries. The problem was circumvented by using the internal 5 V reference when an unreliable supply was used.

4.1.3 Development board

All these functions were put together on a 10 cm × 8 cm PCB, shown with bottom layer in blue and the top layer in red in Figure 4.7. Similar to the functional block diagram, the PIC is in the centre of the board. The thermocouple amplifiers are on the right with the filter circuits on the bottom right. The left of the board contains the DC jack and the RS-232 support.

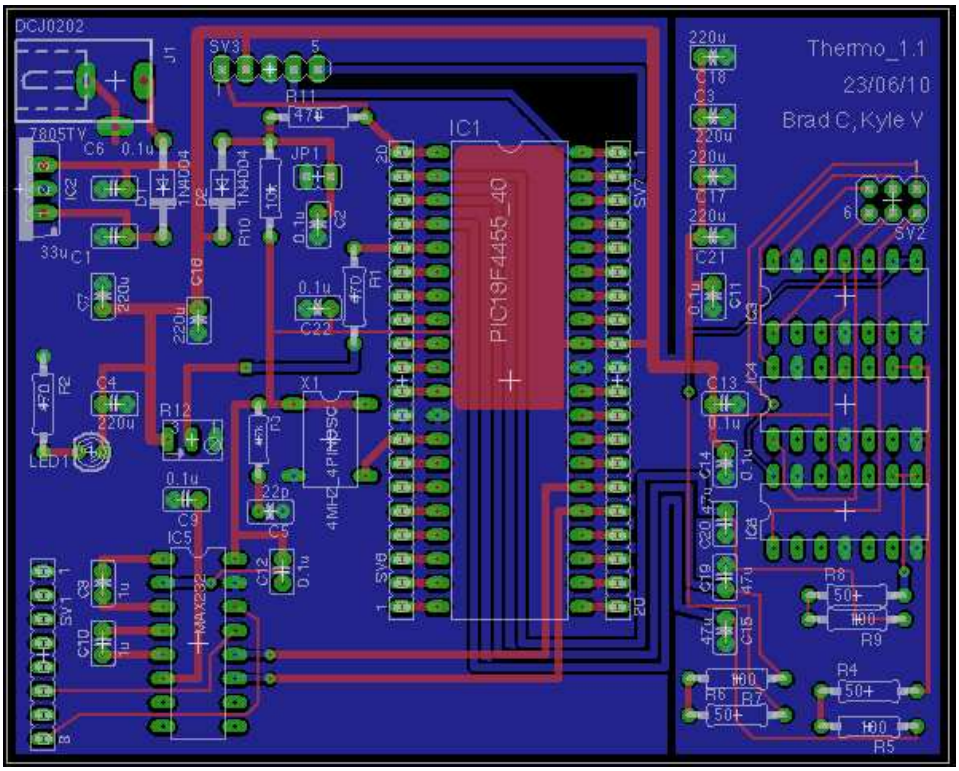


Figure 4.7: Top and bottom layers of the controller PCB.

By fabricating the PCB, potential noise was reduced. This was accomplished by using discrete decoupling components in combination with an embedded capacitor and multiple ground planes [36–38]. The left side of the development board, as shown in Figure 4.7, is the digital plane and the right side is the analogue plane. The two planes are joined by a conductive gap. All routing from one plane to the other is carefully done via this gap to avoid long inductance loops [39, 40].

4.2 Driver Circuit

The controller is able to monitor all the transducers, as well as outputting a PWM signal with the intent of dynamically changing the yield stress of the fluid. This method is similar to the one employed by the LORD Wonder Box® [18]. To achieve this, the coil housed in the damper must be excited enough that the fluid responds in the region necessary to hold with the gap calculations as described in Section 3.3. The PIC processor can not supply enough current to drive the coil directly, and so a MOSFET and driver circuit were developed.

The first stage in the design of the driving circuit was to have a look at the requirements of the fluid, as well as the output capabilities of the controller (see Section 1.3). The PWM signal from the micro-controller is transmitted by an optocouple, which is then amplified by the MOSFET driver. Finally, the MOSFET switches the coil to create the magnetic field in the damper.

4.2.1 Functional overview

Several methods of controlling the fluid were considered, each having varying degrees of complexity. Ultimately, the simplest and quickest to respond topology would make for the best coil excitation. The block diagram in Figure 4.8 gives a basic overview of the system implemented. The signal from the controller goes directly to the optocouple, used to minimise the sampling error [41]. From there, a driver is used to drive the MOSFET, which in turn switches the coil. The driver circuit has its own regulator to supply the digital components, so as to remain isolated from the controller circuit.

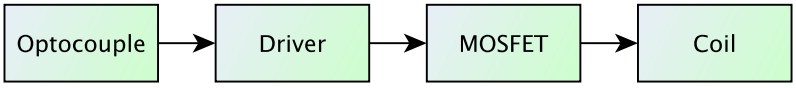


Figure 4.8: Block diagram representation of the driver circuit.

Since the driver circuit switches current in the range of 1,5 A to 3,7 A (based on the annular gap size), a substantial amount of noise is anticipated due to the high frequencies generated when switching the inductive load. This could be induced back into the controller circuit if not electrically isolated [41]. Isolation of the two

circuits is accomplished by means of an *HCPL2631* optocouple between the PWM input and the MOSFET driver [42]. See Appendix B for the circuit diagram.

Resistors R_1 and R_5 together form pull-up resistors for the signal from the microcontroller. The unused input is tied to ground to avoid any unnecessary floating voltages. Capacitor C_5 is specified by the data sheet. Resistor R_4 is another pull-up for interfacing with the driving circuit.

The driver operates similarly to a comparator. It takes the digital input signal and gives a saturated output at a higher voltage [43], which is used to fully bias the MOSFET gate junction. The decoupling capacitor C_3 over the driver supply is specified in the data sheet. The second input is connected to ground, and the second output has been left floating. The output of the driver goes to a voltage divider. The voltage over the coil may be safely increased to 30 V without damaging the driving circuit, as the driver is supplied with 12 V on the output side by a regulator.

Before the gate of the MOSFET, two resistors are used in a voltage divider configuration. The gate resistor R_2 will minimally impede the propagation of the transmitted signal but will also stabilise the MOSFET [44–46]. Resistor R_3 acts to establish the necessary voltage across the Gate—Source junction.

In parallel with R_3 is an 18 V Zener diode (D_2), which protects the gate of the MOSFET from over voltages. The other diode (D_1) is the *CQ827G* Schottky diode, chosen for its fast response time. This diode acts to dissipate current from the coil when the MOSFET no longer conducts. The MOSFET was chosen on its switching speed and its current rating [47]. The worst case current of 3,7 A, relating to an annular gap of 1,2 mm, is designed for.

The capacitor bank put in parallel with the coil fills the purpose of maintaining the current to the coil. Five 2,2 nF WIMA capacitors in parallel make a capacitance of 11 nF. Finding an equivalent single capacitor is possible, but the high value makes it hard to find and would respond slower than several parallel capacitors. Each capacitor used is rated at 63 V.

4.2.2 Operation and analysis

The design for the MOSFET circuit is simple to implement. While the circuit was developed on computer and all the necessary files for producing the PCB were generated, due to cost and time restraints the final circuit was developed on

veroboard, as shown in Figure 4.9.

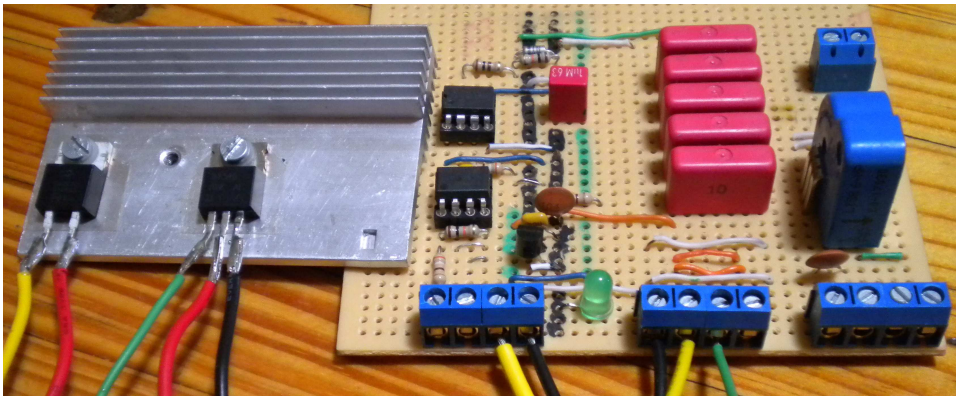


Figure 4.9: Photograph of the driver circuit on veroboard.

The MOSFET and a Schottky diode are placed on the heat sink, with care taken to electrically isolate them. As designed, the circuit takes a PWM signal from the micro and inverts the signal before switching the MOSFET [47]. Terminal blocks were used for inputs into the circuit, and a chocolate terminal block for connecting the devices on a separate heat sink.

The input from the micro-controller is between 0 V and 5 V. The output is inverted by the MOSFET driver [48], which biases the MOSFET gate and consequentially switches the coil. The rise time of the driver is 48 ns with the coil off, and increases to approximately 1 μs with the coil on.

The coil resistance is measured to be 4,8 Ω, which requires 12 V to generate a maximum current of 2,0 A resulting in the fluid achieving maximum yield stress when the MOSFET is fully biased (see Section 3.2). The inductance of the coil is 40 μH, relating to an acceptable response time to a change in current. The simulation of these settings are shown in Figure 4.10

Connecting both the controller and driver circuit, plus connecting all the sensors, may be complicated without a circuit digram. To simplify the procedure, the circuits are connected together then placed into a package with terminals available for external connection of sensors, power and the coil.

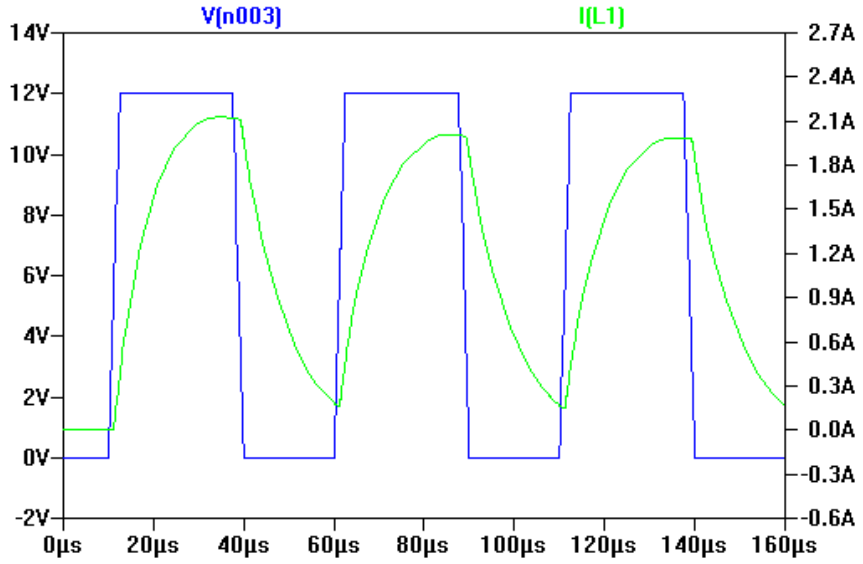


Figure 4.10: Simulation of the current through the coil versus the gate voltage.

4.3 Packaging

The packaging simplifies the circuitry use (with the aid of ports and labels), and creates a protective barrier from environmental hazards. Before the package may be designed, the type of environment and expected hazards were assessed, along with the type of end user that is expected.

4.3.1 Outline of requirements

The damper system is intended to be used inside laboratories by members of the School of Civil Engineering. Based on this information, environmental conditions such as:

- temperature,
- humidity and
- element exposure

are kept relatively constant. Consequentially, the packaging consists of plastic and aluminium. It also need not be airtight, nor are desiccants required. The package is also expected not to come into contact with any hazardous gases.

Once inside the packaging, the users will require access to the circuit functions in order to operate the device. Ports on the external package allow for this. Indicator LED's are visible to the operator on the front panel.

4.3.2 Internal positioning of equipment

The box chosen is just large enough to fit all the circuitry compactly inside. All together, there are four separate parts placed inside the box, namely:

1. Control circuit
2. Driver circuit
3. MOSFET and Schottky diode on heat sink
4. Display and Button Panel

Each part is secured to an appropriate place within the box, as shown in Figure 4.11. The MOSFET and Schottky don't produce excessive heat, and so are attached to a small heat-sink and glued to the top of the box. All connecting wires to the package walls are removable for easy dismantling of the product.

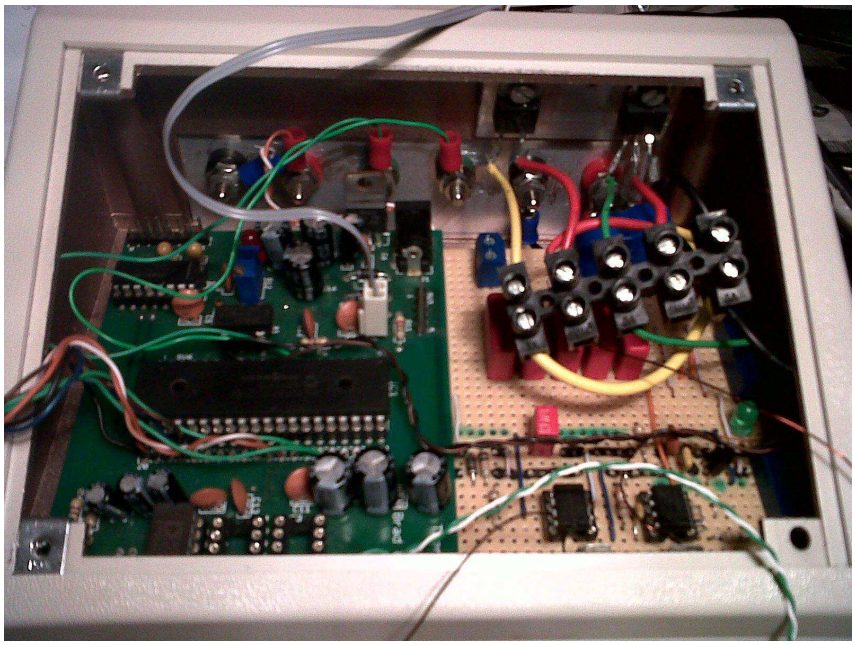


Figure 4.11: Photograph of the internal positioning of the circuits.

The veroboard driving circuit is mounted to the bottom of the package, with the controller placed in the available free space on the veroboard. The controller is on rubber feet to avoid electrical contact with the components on the driving circuit. The display and buttons are glued into place on the top panel of the box.

4.3.3 External access

In order to operate the controller whilst contained in the packaging, several connectors are included on the outside of the the packaging. These connectors allow power to be supplied to both the controller and driver, as well as switches and buttons for interacting with the controller. Ports are made available for serial communication, but programming the microprocessor requires internal access.

Power is supplied separately to the digital logic and the driving circuit. The separate supplies may be connected externally using the two sets of red and black terminals on the back of the package. One set is for the digital supply and the remaining set supplies the coil and has a 3,7 A fuse connected internally to prevent over-currents. Typically, the following voltages are applied to the terminals:

- Digital Supply - 9 V
- Coil and Driver Supply - 12 V to 30 V

The coil and driver power supply may change based on the PWM scheme used and on the annular gap size. The bigger the gap, the greater the current demand. Once connected, the coil may be switched in and out of the circuit by the toggle switch provided. If currents higher than 3 A are required, the toggle switch must be bypassed. The two accelerometer inputs (green banana terminals) are situated close to the supply voltage to minimise the wire loop area.

Figure 4.12 shows the available ports which are visible from the top of the package. The buttons connect to a digital i/o port on the microprocessor, with the exception of the reset button which links to the reset pin. The on/off toggle switch disconnects the supply to the coil. Three sets of coloured banana input terminals are provided for easy connection of the coil and transducers.

The accelerometer inputs may be found on the back of the package. Programming the microprocessor is not externally accessible, and may only be done by removing

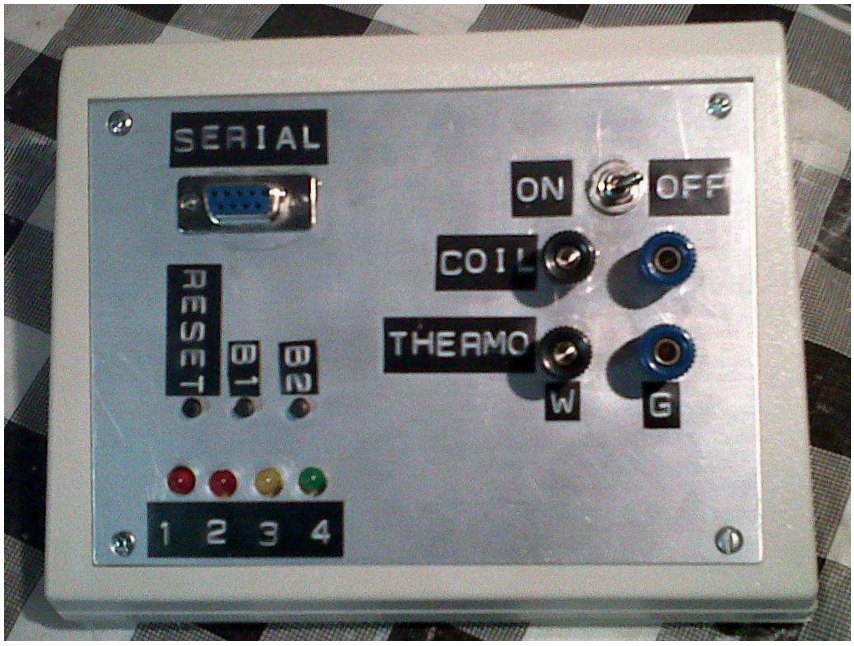


Figure 4.12: Photograph of the package taken from the top view.

the cover. This minimizes the chance of erroneous code being implemented by an inappropriate user. Data may be received serially via the RS-232 port found on the top left of the front panel.

Three push-buttons are provided. The first button is the microprocessor reset button, and the remaining buttons ($B1$ and $B2$) may be programmed for any function, but are primarily included to be used as a "Set" and "Output Data" for non real-time operation.

4.3.4 Display

Just below the push-buttons, on the front panel of the packaging, are the display LED's. The labels for the LED's are numerical since they may be re-programmed (see Section 4.1). The intended use for each LED are as follows:

1. Controller power
2. Damper thermal warning
3. Event triggered
4. Miscellaneous warning

Colour coding of the LED's are used to distinguish between the various functions. The bus connecting the LED's to the microprocessor are easily disconnected, but the panel itself is glued in place. With the top panel securely closed, the contained circuitry is securely mounted with the terminals clearly labelled. The packaging was not used during the assessment of the accelerometers, as the additional weight would have caused the unbalanced load to wobble on the lathe (see Section 5.1.4).

4.4 Conclusion

The performance of the damper was assessed by monitoring the three transducers using the controller circuit. The controller incorporates several functions necessary to monitor the experiment and calibrate the accelerometers. It also has several additional functions that aid in directly developing on the controller. Each input is monitored by an ADC port with appropriate filtering prior to sampling. The digital output of the controller is processed by the driver circuit.

The driver circuit acts as the interface between the controller and the coil. This circuit is isolated by means of a digital optocouple such that feedback to the controller is minimised. The coil is switched by an n-channel MOSFET, biased by a MOSFET driver, where the voltage and current requirements are based on the coil properties and annular gap size. Precautions were taken in terms of dissipating current and over voltage protection.

The circuitry was packaged to withstand laboratory conditions and transportation. All relevant features of the system, such as transducer inputs and communication ports, were made accessible so that the package need not be opened for anything other than programming the microprocessor. Dismantling of the product was simplified for potential further development.

Chapter 5

TRANSDUCERS

Two accelerometer circuits were previously mounted for monitoring the shock absorber when operated with hydraulic fluid. These transducers were first evaluated in terms of their fitness for the new task, as well as calibrated. Similarly, the thermocouple cable and amplifier were designed and calibrated.

5.1 Accelerometers

The revised goal of the accelerometers are to both monitor each experiment and give feedback to the control circuit. To achieve this, the response time of the accelerometers must operate fast enough for control during an impact. This requirement makes most digital accelerometers inappropriate [49]. The next priority is accuracy in terms of the maximum error possible. The sensors employed have to complement the experimental set up in terms of geometry, power requirements and robustness.

The accelerometers supplied with the damper contain iMEMS® *ADXL78* transducers by Analogue Devices [29]. This type of transducer is generally used for vibration monitoring and control, collision detection and shock detection, making it ideal for the required application. Figure 5.1 shows one of the accelerometers. The accelerometer itself is encased in a steel packaging.

5.1.1 Functional overview

Separate from the controller, each accelerometer has its own amplifier [50], filter and reference as shown in Figure 5.2 [51]. Since the transducer emits an analogue



Figure 5.1: Photograph of an accelerometer on the supplied development board.

signal, no clock signal is necessary from the micro-controller to the transducer. The amplification process is best done before the signal is transmitted to the micro, to avoid any significant voltage drop.



Figure 5.2: Block diagram of the accelerometer circuit.

Contained on the accelerometer development board is a 2 pole Bessel filter with a cut-off of 400 Hz. Each accelerometer is supplied via a voltage regulator with a diode for reverse bias protection. The regulator for the accelerometer outputs 5 V for an input voltage between 6,5 V and 30 V. Both circuits should output a signal centred at 2,5 V for 0 g.

5.1.2 Sampling and converting

When calibrating the accelerometers, the transducers were sampled such that approximately one full revolution is sampled with only 120 integers. When detecting an impact, each accelerometer is sampled by the microprocessor at 2 kHz on 10 bit ADC ports. This is sufficiently fast compared to the Nyquest rate of 600 Hz (based

on the accelerometer filters) [52]. With a reference voltage of 5 V, the maximum resolution is 4,88 μV, or 0,15 g for Accelerometer 1 and 0,17 g for Accelerometer 2.

The transducers have a range of 2,5 $\pm$ 2,317 V for Accelerometer 1 and 2,5 $\pm$ 2,030 V for Accelerometer 2, based on the calibration data. Converted to acceleration, the range is between $\pm$70 g.

5.1.3 Placement and performance

Each accelerometer was firmly secured to the falling mass, as shown in Figure 5.3. The circuit was carefully bolted to a curved metal plate, using plastic pads to both electrically isolate the circuit and to reduce horizontal shock waves. The plate was then bolted to the mass, along with a thin metal covering which protects the accelerometer circuit from EMI and physical damage.



Figure 5.3: Positioning and casing for the accelerometer circuits.

From the position that the accelerometers were mounted, the output from each accelerometer should theoretically be identical, assuming the driving mass falls vertically with no side to side movement. With the non-calibrated accelerometers, each reading was suspect and the two differed widely from each other for the same impact. Before the calibration process could be set up, the accelerometers had to

be evaluated in terms of what performance was expected. Table 5.1 summarises the main points of interest.

Table 5.1: Accelerometer relevant specifications [29].

Characteristic	**Quantity**
Maximum Non-linearity	2 %
Cross axis sensitivity	5 %
Sensitivity	25,65 to 28,35 mV/g
Clock Noise	5 $\mathrm{mV_{p-p}}$
Output Voltage Maximum	$V_{DD}-$ 0,25 V
Output Voltage Minimum	0,25 V
Temperature Range	−40 to 105 °C
Supply Voltage	−0,3 V to 7 V

5.1.4 Accelerometer calibration

Often, calibration of accelerometers require linear motion laboratory instruments [53]. The draw back of this method, other than needing the right equipment to perform the procedure, is that long displacements are needed for static acceleration and low frequency vibration. Due to this, a rotation method was adopted to calibrate the accelerometers. A basic model of the system is supplied in Figure 5.4 [53].

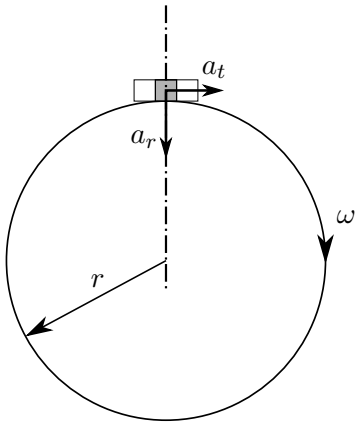


Figure 5.4: The accelerometer as placed on a rotating trajectory, adapted from [53].

This method involves rotating the accelerometers and mathematically translating the RPM of the motor to centripetal acceleration a_r by means of Equation 5.1:

$$\alpha_r = \omega^2 \times r \tag{5.1}$$

Once the signal is captured it may be compared with the expected reading, by using the radius (r) in conjunction with the angular velocity (ω) of the motor. The tangential acceleration (a_t) may be used to explore the cross axis sensitivity effect [53].

The accelerometers were tested one at a time. Each accelerometer remained on its respective PCB, which is in turn bolted to a steel plate. The three wires required to power the accelerometer and transmit the signal were connected to a 9 V cell and the data acquisition circuit respectively.

The data acquisition circuit used was the same circuit developed for the control of the shock absorber. The code to perform the operation follows the procedure shown in the flow diagram in Figure 5.5. The initial delay allows the motor to achieve a steady state before logging the signal from the accelerometer to be tested.

The time period over which the samples were taken varies according to the speed of the rotor. Ideally, one complete revolution of the rotor would be captured per time period. The reason for this is because of the limited amount of acquirable data on the 10 bit microprocessor, which allows approximately 120 integers to be stored in volatile memory. With the code and procedure formulated, the equipment needed to perform the calibration included:

- Lathe (motor)
- Equipment mount
- 9 V Cell
- Data acquisition circuit

A lathe provided quick and fine control for discreet speeds between 20 RPM and 2000 RPM. In order to mount the equipment in the lathe a support mount was fashioned out of wood with places for the data acquisition circuit, a 9 V cell and a correctly orientated accelerometer circuit. Once set in the lathe, the data was sent serially after each experiment.

Following the procedure outlined above, the lathe was loaded with the mount containing the components as shown in Figure 5.6. All loose wires were tucked

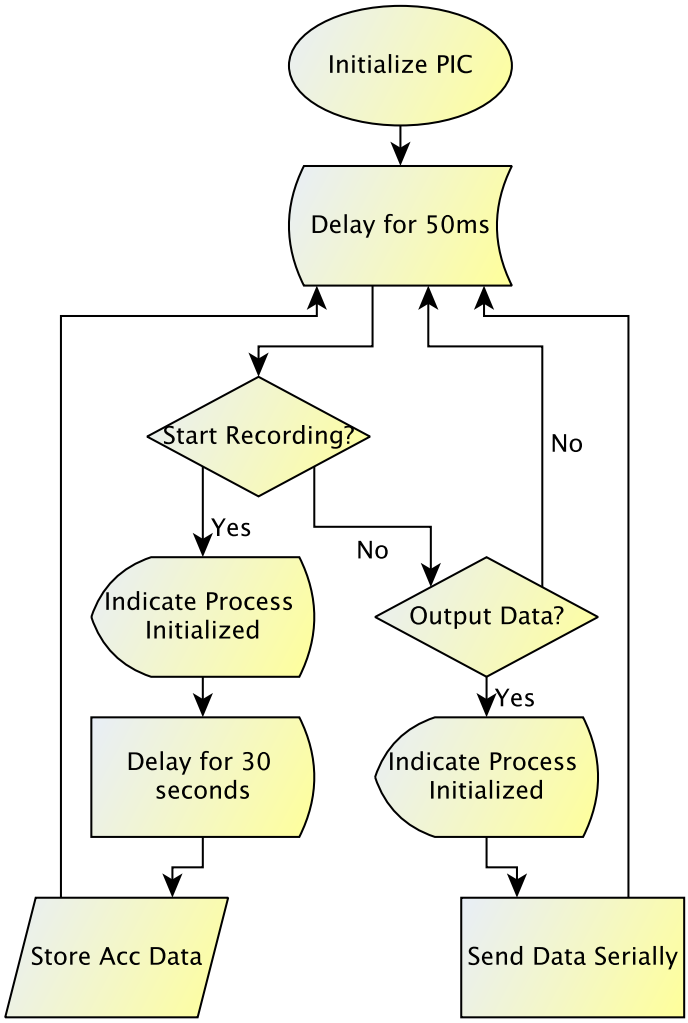


Figure 5.5: Flow diagram of the calibration code.

strategically away, and the electronic components were cushioned using double-sided tape.

The support mount offered enough space at the rear to be clamped into place, and the front end was marked and center-punched for the placement of the rotational pin. A perpendicular protrusion was placed so that the accelerometer may be placed with its positive measuring axis aligned with the expected centripetal acceleration. Drill-holes were placed at strategic positions so that the equipment could be secured in place using cable ties.

The motor speed was then measured and verified using a stroboscope. After each completed experiment the motor is powered down and the data sent serially to a PC over RS-232. The operating speeds are shown in Table 5.2, along with the

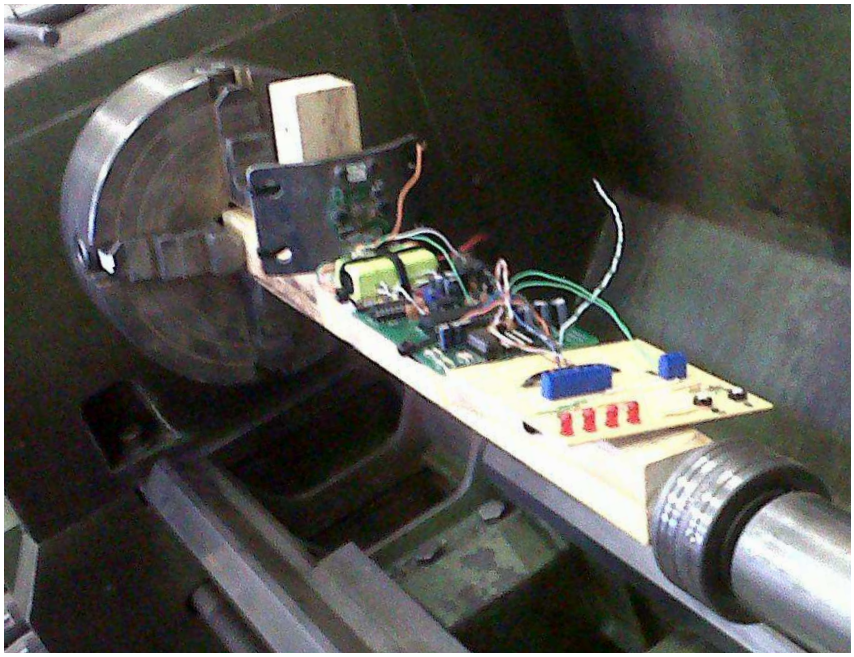


Figure 5.6: The mounted accelerometer and circuit in the lathe.

centripetal acceleration and calculated sample frequency. The same calculations are used when the sensors are flipped around to assess the opposite sensing direction.

Table 5.2: Calibration data as it relates to the speed of rotation.

Measured RPM	**Centripetal Acc.** (rad/s^2)	**Acc. in gravities** (g)	**Time per revolution** (ms)	**Sample Frequency** (Hz)
430	93,27	9,33	139,53	860
480	116,22	11,62	125,00	960
695	243,66	24,37	86,33	1390
993	497,41	49,74	60,42	1986
1209	737,34	73,73	49,63	2418

The lathe employed has several operating speeds, but only five operating speeds were applicable. If the rotation is too slow, the sample frequency necessary to capture one complete revolution has the potential to alias, and if the rotation is too fast the accelerometer will saturate. For each speed, the accelerometers were tested three times. This was to ensure consistency and repeatability. The accelerometers proved to be reliable in terms of both. Illustrated in Figure 5.7 are the three graphs for the repeated readings taken whilst operating at 430 RPM.

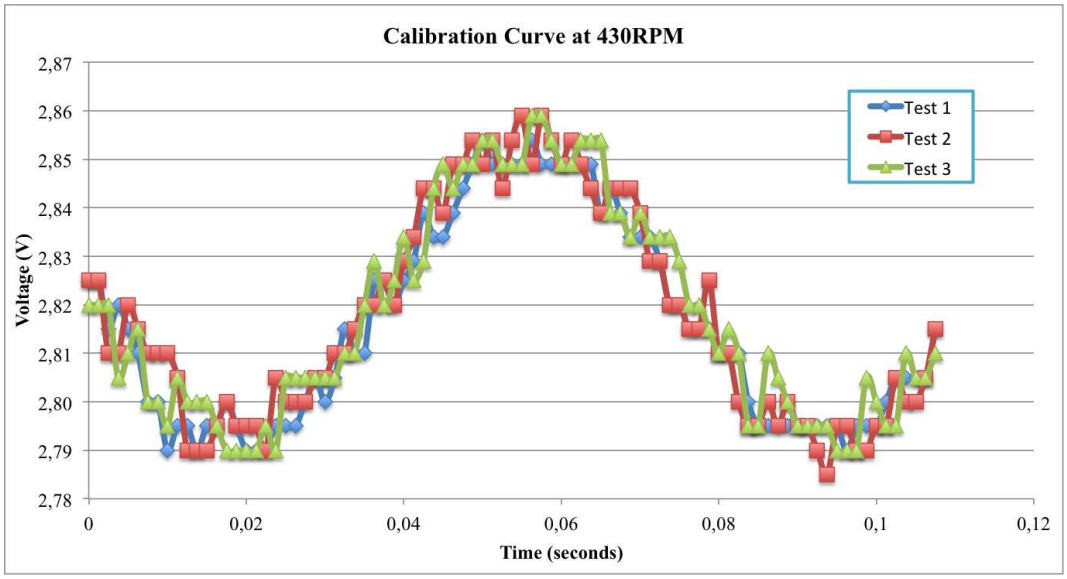


Figure 5.7: Results obtained from three experiments at 430 RPM using Acc 1.

The DC offset is due to the centripetal acceleration, while the imposed sinusoid is attributed to gravity. This is due to the orientation of the accelerometer during rotation. The super imposed signal from gravity provides the position of the accelerometer for each reading, as well as giving an indication to the dynamic response of the acceleration. The final measurement at 1209 RPM saturated, as expected.

By taking the DC offset for every set of readings, and comparing it to the ideal, Figure 5.8 was produced. The straight trend line confirms that the accelerometers are linear. The ideal trend line, shown in green, is very similar to Accelerometer 2, where Accelerometer 1 has a more sloped gradient, reflecting a lower sensitivity.

According to the information obtained from the graph, Accelerometer 1 has a sensitivity of 33,1 mV/g and Accelerometer 2 has a sensitivity of 29,0 mV/g. Both graphs have an offset that fall well within ±150 mV, as specified by the *AD22281* data sheet [29].

All experiments were done under similar conditions, with an ambient temperature of approximately 28 °C. The calibration equations for the accelerometers are given in Equation 5.2 and 5.3, where the first equation describes the response of Accelerometer 1 and the second describes Accelerometer 2.

$$acc_1 = 0.0331 \times acc_{1g} + 2.5 \tag{5.2}$$

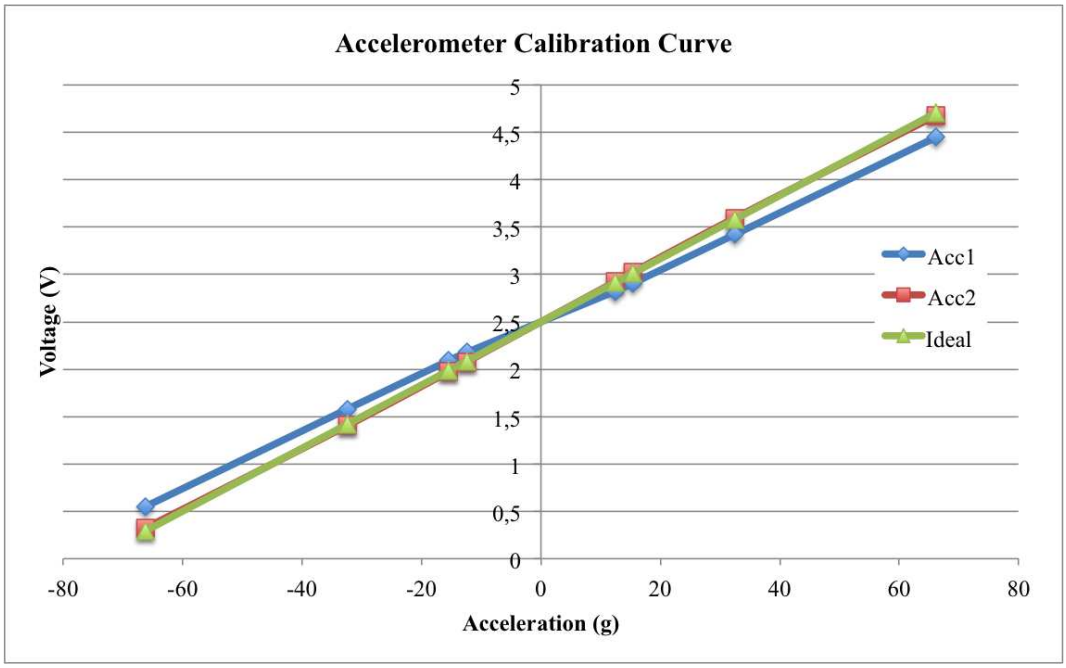


Figure 5.8: Calibration curves for the accelerometers.

$$acc_2 = 0.029 \times acc_{2g} + 2.5 \tag{5.3}$$

where

acc_1 = Is the acceleration of accelerometer 1 in V
acc_2 = Is the acceleration of accelerometer 2 in V
acc_{1g} = Is the acceleration of accelerometer 1 in gravity (g)
acc_{2g} = Is the acceleration of accelerometer 2 in gravity (g)

The more rigid the damper is when impacting with a test material, the faster the impact is expected to occur. This relates to the acceleration of the mass, and rate of change of the accelerometer signal. Due to the inherent 400 Hz second order, low-pass filter of the accelerometers, measuring frequencies above 300 Hz would incur an attenuation greater than 80 % of the signal. Focusing below this frequency would miss a lot of the information generated by the impact.

The analysis of the error of each transducer for a frequency of 300 Hz is summarised in Table 5.3. The accelerometer's associated error differs to one another due to their unique transfer functions.

The error translates to 35 % for Acc 1 and 34 % for Acc 2. While this error is significantly high, it is a worse case error and acceptable for the preliminary purposes

Table 5.3: Accelerometer error accumulation.

Error Source	**Acc 1 Error** (mV)	**Acc 2 Error** (mV)
Transducer	±96	±91
Bessel Filter	±944	±887
1st Order Filter	±605	±569
Total Error	±1 645	±1 547

of testing the damper. See Section 8.1 for recommendations on improving this error. The error due to conversion is insignificant relative to the total error.

Thermal drift has an insignificant effect due to the conditions the device is operated under, in conjunction with the operating temperature range of the accelerometers. Cross axis-sensitivity and package alignment of the transducers are taken into account in Chapter 6.

5.2 Thermocouple and Heating Effects

Measuring the temperature of the MR fluid (inside the shock absorber) ensures that the device is operated correctly and safely. While it is difficult to get a transducer into the damper to take thermal measurements, the task is made easier by using K-type (chromel-alumel) thermocouple wire. The single core, twisted pair is shorted at the sensing end and is easily placed inside the damper through the same access point as the copper wire for the coil.

The thermal transducer circuit is first over-viewed from a functional perspective, before the placement and performance are evaluated [51]. The transducer was then evaluated and calibrated to ensure accurate measurements were taken. Finally, the filtered signal produced by the thermocouple amplifier was sampled by an ADC port on the micro-controller.

5.2.1 Functional overview

Before the thermal measurement can be sampled, it is first picked up by the thermocouple cable as explained by Figure 5.9. From the thermal detection, the

signal is linearised and amplified by an thermocouple amplifier, then filtered and finally sampled by the micro-controller [51].

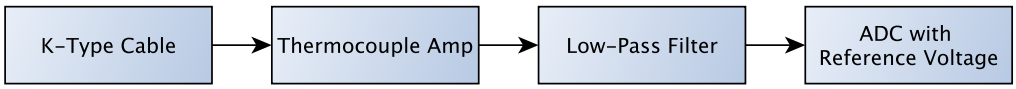


Figure 5.9: Block diagram of the thermocouple circuit.

The thermocouple wire operates on the thermoelectric effect [51, 54], where a voltage is generated across the thermocouple wire due to dissimilar metals. In this case, the thermocouple cable is manufactured from chromel-alumel and is classified as IEC Class 1, K-type. The thermal couple is made up of two single core (0.2 mm) wires twisted together.

This signal is received by the pre-trimmed thermocouple amplifier ($AD595CQ$) which linearly amplifies the thermocouple signal based on Equation 5.4 [55]. The $AD595CQ$ ideally gives 10 mV/°C.

$$AD595\ output = (Type\ K\ Voltage + 11) \times 247.3\ \mu V \tag{5.4}$$

The chosen thermocouple amplifier is cold-junction compensated and can measure temperatures from 0 to 300 °C, making it ideal for the application. The temperature of the system changes relatively slowly, which is reflected by the 20 Hz low pass filter explained in Section 4.1.

5.2.2 Sampling and converting

Since the change in signal is sluggish, sampling can be done at relatively low rates. The thermocouple signal is sampled at 100 Hz, to avoid any possible aliasing, by a 10 bit ADC port on the micro-controller using a 5 V reference (V_{Ref}). Using Equation 5.5, the $PIC18F452$ will have a maximum resolution of 4,88 μV.

$$Resolution = \frac{V_{Ref}}{Bit\ Resolution} \tag{5.5}$$

The conversion process introduces an error of approximately 0,05 %. The 5 V reference is set internally to avoid any voltage drift. The maximum possible temperature measurable with this configuration is 300 °C.

5.2.3 Placement and performance

The K-type wire is soldered at the sensing end and placed inside the cavity designed for the coil, where it can monitor the MR fluid inside the damper (see Figure 5.10). The single core wire shares the same access as the coil wiring, without requiring too much widening of the hole through the piston. This minimises potential leaking.

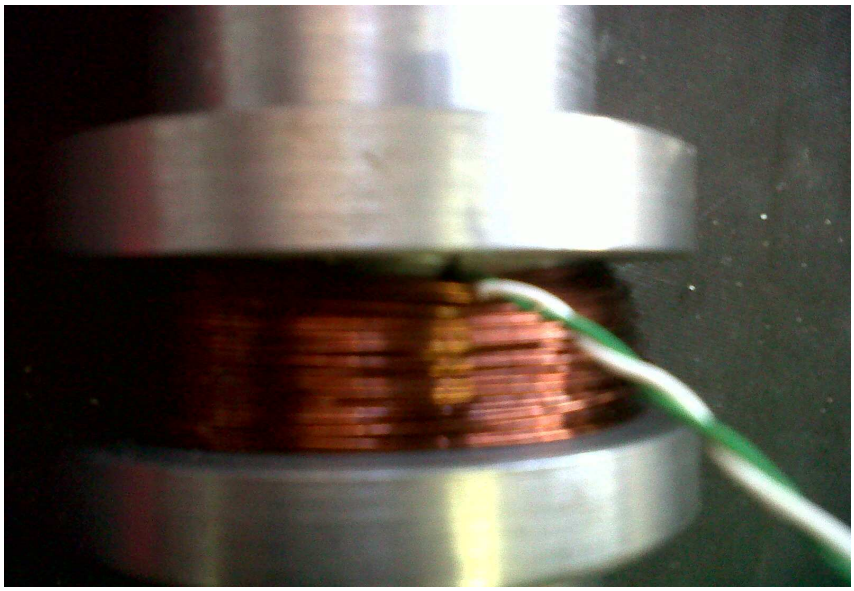


Figure 5.10: Placement of the thermocouple cable through the piston.

The thermocouple wire and amplifier specifications are summarised in Table 5.4. The specifications listed focus on the operating conditions of the circuit and the inherent errors.

The calibration for the thermocouple transducer takes into account the operating conditions, and the corrections to the thermocouple output are done via the microcontroller.

Table 5.4: Thermocouple amplifier relevant specifications [55].

Characteristic	**Quantity**
Input Offset	40,44 μV/°C
Sensitivity	10 mV/°C
Output Voltage Maximum	$V_{DD}-$ 2 V
Output Voltage Minimum	0 V
Temperature Range	−55 to 125 °C
Supply Voltage	5 V to 30 V

5.2.4 Thermocouple calibration

While the damper is only expected to be operated in the laboratory, the damping process causes energy to be absorbed and it is anticipated that the MR fluid will absorb energy and heat up. Referring to Section 1.3, the fluid can operate between −40 °C and 130 °C with a flash point of 150 °C. Since 0 °C to −40 °C temperatures are unlikely and cannot damage the device, the thermal measurements are calibrated from 0 °C to 150 °C.

The thermocouple transducer circuit was calibrated on a Fluke 5520A Multifunction Calibrator [56]. Being careful to set the calibrator to the correct grounding scheme and matching it to the K-type thermocouple used, the input was gradually increased and the thermocouple transducer calibrated.

The process described by Figure 5.11 was conducted on two separate days for the sake of determining repeatability. The calibration signal was manually adjusted after logging 10 values.

The calibration process was terminated when the operating temperature range was fully covered. The temperature was incremented by 10 °C each time. From this process the thermocouple response may be mapped and the system calibrated.

The data obtained is illustrated graphically in Figure 5.12, where each step clearly shows where the Fluke input was incremented. The repeated experiment follows this trend exactly, proving that the sensor is repeatable.

By taking a single data set for a given temperature, the noise induced in the system can be quantified. Figure 5.13 shows the change in voltage for the arbitrary temperature of 38,5 °C.

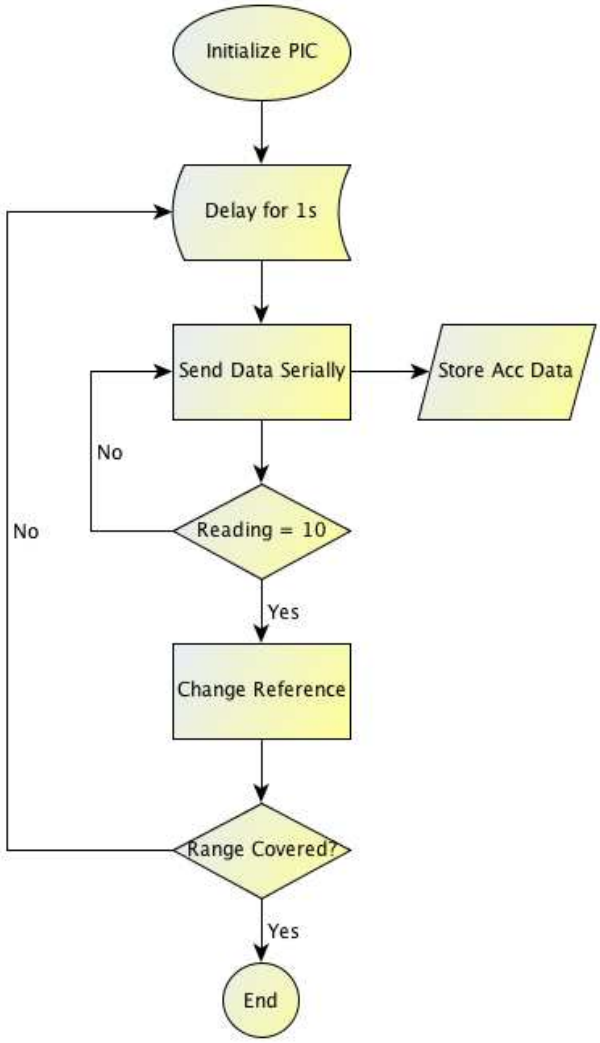


Figure 5.11: Flow diagram of the thermocouple calibration process.

From the graph, the maximum recorded voltage oscillation is measured at 3 mV, which translates to 0,3 °C. This level of oscillation may also be found for other calibrated temperature values recorded. The noise is quantified using Equation 5.6:

$$SNR_{dB} = 20 \log_{10} \left(\frac{V_{Signal}}{V_{Noise}} \right) \tag{5.6}$$

From the equation above, the signal to noise ratio (SNR) is 10.5 for a signal sensitivity of 10 mV and 3 mV of noise. This is an acceptable amount of noise and only minimally impacts on the integrity of the signal.

In Figure 5.14, it can be confirmed that the thermocouple gives a linear output,

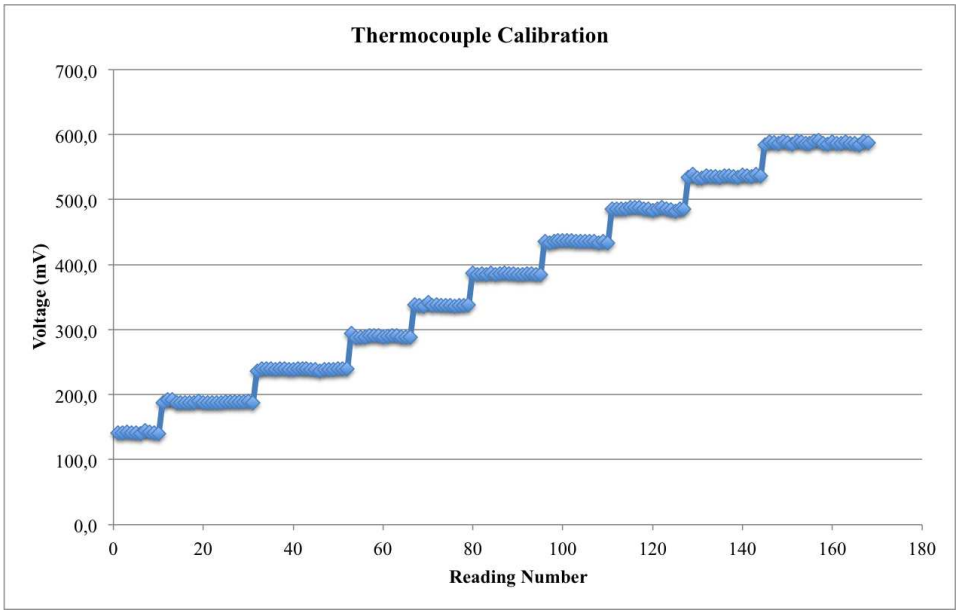


Figure 5.12: Results obtained directly from the calibration process.

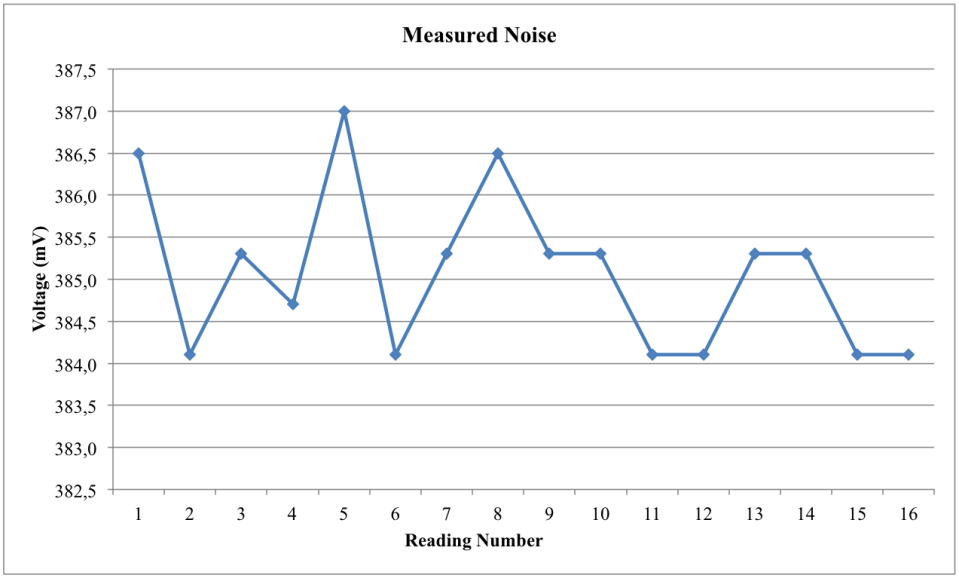


Figure 5.13: Typical noise on thermocouple circuit at 38,5 °C.

where the error bars reflect the noise measured. From the graph, it may be observed that there is a general +1,15 mV offset. This was easily corrected for in code on the micro-controller.

The percentage error for the thermocouple circuit is shown in Figure 5.15. As anticipated, the error decreases for increasing temperature as the induced noise has less impact. The maximum error is 0,9 % at 150 °C.

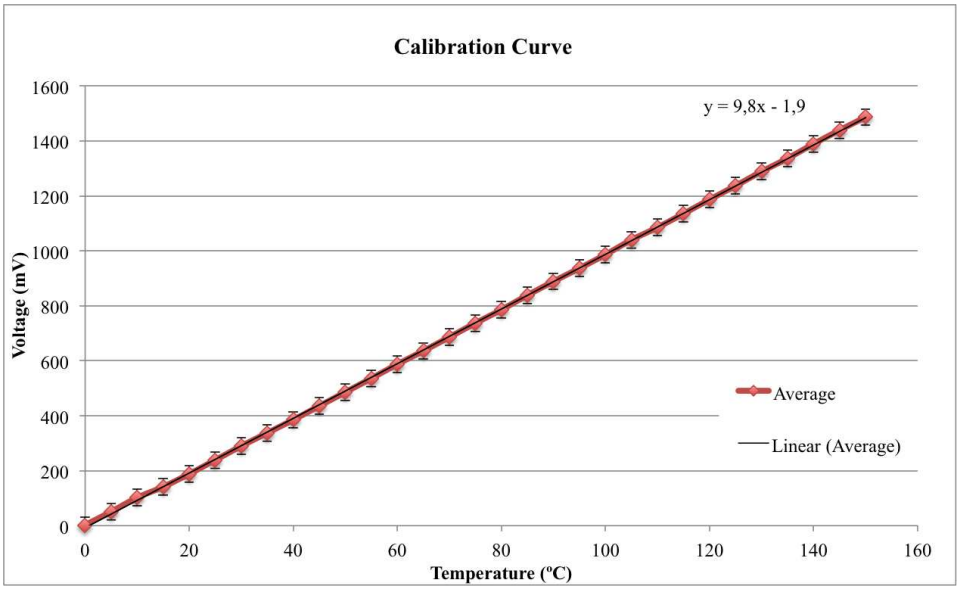


Figure 5.14: The calibration curve for the thermocouple amplifier.

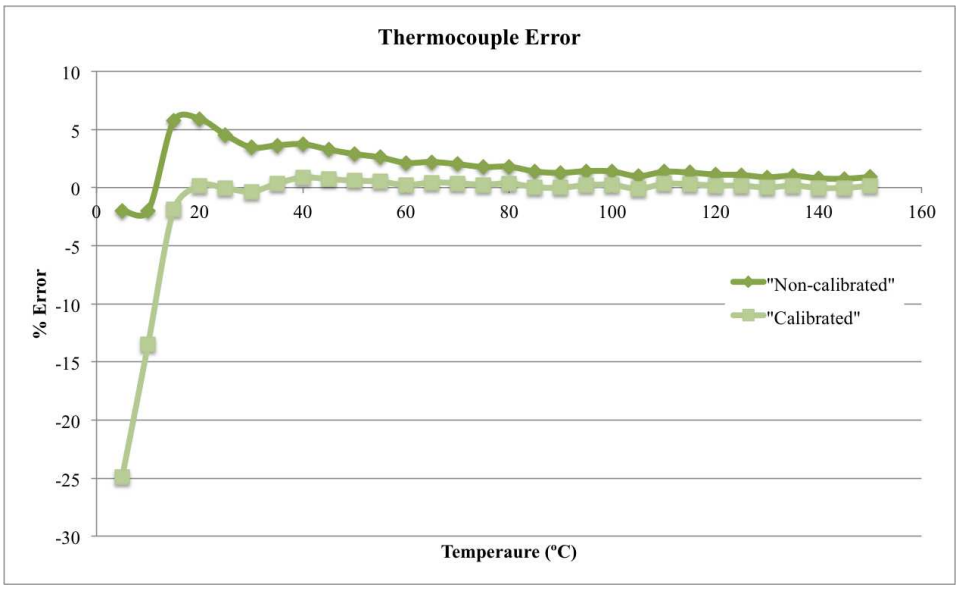


Figure 5.15: Comparison between calibrated and non-calibrated error.

The error due to thermal drift is specified as a maximum of 0,6 °C when operated between 0 °C and 50 °C [55]. The expected operating temperature is approximately 25 °C, since the damper will be operated in a laboratory. At this temperature the thermal drift is approximately 0,1 °C [55]. The errors have been summarised in Table 5.5.

The error due to the filter is negligible, since there is a high input impedance into the micro-controller and since the signal does not change fast enough to be affected by

Table 5.5: Temperature circuit tolerances.

Error Source	**Maximum Error** (mV)
Thermocouple Wire	±15
Amplifier	±16
Filter	0
Conversion	±0,005
Induced Noise	±2
Total Error	±33,005

the 3 dB point. The error from conversion is not significant, making the maximum accumulated error ±33 mV which translates to ±3,3 °C. With calibration, this error is reduced to ±0,35 °C.

5.3 Conclusion

It was determined that the supplied accelerometers are adequately suited for the adapted shock absorber, due to their analogue nature and robust packaging. The accelerometers were calibrated and secured to the driving mass, while the necessary adjustments were implemented on the PIC microprocessor.

A thermocouple wire and amplifier were installed such that the temperature of the fluid inside the damper could be monitored. The thermocouple wire was inserted into the device using the same access point as the coil which generates the magnetic field. The calibrated accelerometers give an error of ±0,35 °C. Dangers such as leaking due to fluid expansion and overheating were avoided during experimentation by monitoring the temperature of the fluid whilst testing.

Chapter 6

EXPERIMENTAL PROCEDURE FOR THE DROP TESTS

In order to establish if the proposed method of preforming an RLT is viable, the developed damper and control system was tested using similar conditions to the final application.

Firstly, the expected application was identified and an appropriate drop rig was developed to emulate this process. The errors induced by the experiment itself are quantified before the experimental procedure is related. The possible improvements are discussed in terms of the impact on the final design.

6.1 Emulation of Pile Testing

The shock absorber is designed to act as both a cushioning material between the driving mass and the pile, and to control the impacting force on the pile. Ideally the coil should not be energised until the piston head first comes into contact with the pile, after which the desired force may be obtained by controlling the yield stress of the MR fluid. Table 6.1 outlines the overall requirements of the experiment in order to be comparable to actual pile testing practices [4].

Without a control algorithm, it is possible to damage the shoulder of the piston if dropped from the maximum height specified [4]. Regardless, the calculations and modelling assumes the maximum drop height as the worst case scenario. The distance of the damper's stroke used governs the period over which control may be asserted. This is largely based on the final velocity and mass.

Table 6.1: Final specifications of the drop test.

Parameter	**Value**
Maximum Drop Height	2,5 m
Stroke of Piston	20,0 mm
Maximum Final Velocity	7,0 m·s^{-1}
Weight of Mass	10,2 kg

6.2 Development of Drop Rig

A rig guides the damper while it descends, as shown in Figure 6.1. The primary function of the rig is to guide the damper during its decent to minimise the error that occurs from misalignment with the vertical. The shock absorber has a 15 mm circular cut-out through the center where the guide rod is placed.



Figure 6.1: Photograph of the drop rig.

A rod of diameter 14 mm is positioned through the center of the damper and held vertically in place by a mild steel cross-bar. The guide rod may be positioned over a selected test material. The base of the rig is made from square piping which both contains the soft-board and supports the vertical components. The entire rig is made from mild steel parts welded in place.

6.3 Practical Errors

An error value is introduced into the system by virtue of the experiment itself. This error arises from the freedom allowed by the guiding rod and the central cavity in the damper. When the damper falls, it may tilt to a side which has the affect of misaligning the accelerometers. Since two accelerometers are used on either side of the driving mass, it is possible to digitally compare the two signals and get an idea of how much the damper wobbled during an impact.

The maximum allowable wobble is dictated by the diameter of the guiding rod used and the length of the piston. This is illustrated in Figure 6.2, where the maximum angle formed is described by Θ.

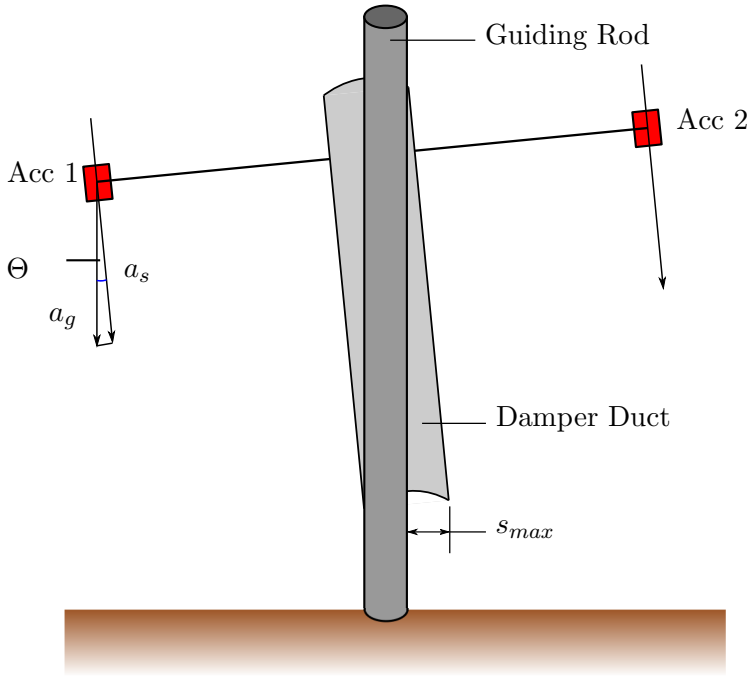


Figure 6.2: Misalignment affect on the experiment.

By using a 13 mm rod in the bored centre whole with a 15 mm diameter, the maximum misalignment length (s_{max}) is only 2 mm. Combined with the 200 mm piston length, the maximum angle possible for Θ is 0,57 °C. This translates to a 0,005 % error in the accelerometer readings. While this error is not very significant, measures taken to reduce this error include:

- Correctly aligning the drop rig
- Properly sizing the guiding rod
- Using a floating bearing to properly distribute the force

The drop rig was aligned with a spirit level, but the guiding rod cannot be made to fit too well as it would generate resistance and possibly damage the wiring which shares the same whole.

6.4 Experimental Procedure and Methodology

The initial experimenting with the shock absorber required manual tweaking of the yield stress in order to build an expected response of the system. Following the diagram in Figure 6.3, the PWM was first set to a known frequency and duty cycle. Starting with a duty cycle of 0 % and ending with 75 %, each experiment was repeated three times. A 100 % duty cycle would be similar to short circuiting the supply.

The process was similarly repeated for a changing frequency with a set duty cycle of 50 %. To take each reading, the damper was lifted to the appropriate level and was kept suspended using a cord. The piston was checked for full extension and a rubber band was used to determine the total stroke used. The controller was then reset and the coil engaged via the switch. When the cord was released, the damper fell and impacted with the test material, triggering the controller to data capture and then transmit the captured process.

The damper is raised to a height of only 120 mm to build preliminary data and to assess the plausibility of the design. The drop height was chosen based on a discussion with Dr. I. Luker [4], and the available materials used for the support rig. The experiments performed on the damper are summarised in Table 6.2.

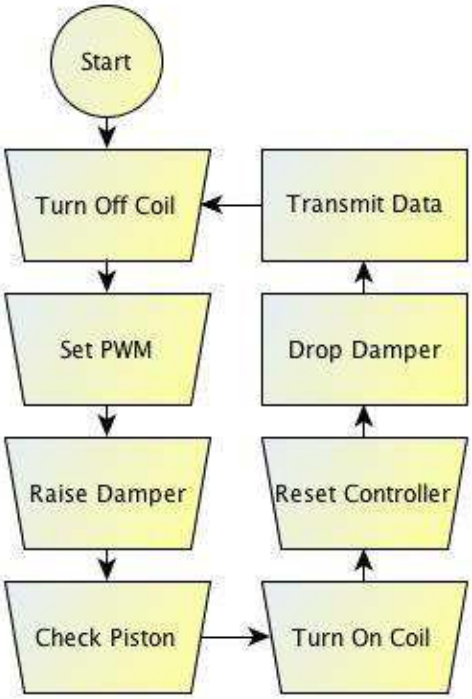


Figure 6.3: Flow diagram of the manual procedure.

Table 6.2: Summary of experiments performed on the damper

Test Conditions	**1**	**2**	**3**
Stationary	Off	On	-
Thermal Response (kHz)	10	20	90
Frequency (kHz)	10	20	90
Duty Cycle (%)	0	50	76

The stationary test refers to when the damper was not dropped or moved, whilst the set up was checked. The traducers were then checked when the coil was powered on and off. During the stationary test, the thermal response of the fluid was monitored to determine how the damper responds thermally to a change in frequency.

When changing the frequency, the duty cycle is set to 50 %. A drop height of 120 mm was used when taking all measurements, which is based on the geometry of the drop rig and the height restrictions previously mentioned. Similarly, the duty cycle tests are all performed using a 20 kHz frequency while the duty cycle is manipulated.

6.5 Conclusion

The experiments performed emulate typical conditions. This was accomplished by means of a drop rig which guided the damper to the test material. The error introduced from the experiment rig was found to be negligible relative to the error associated with the accelerometers. The first experiment establishes that the various components are operational and establishes how the damper responds thermally, while the two subsequent experiments were devised to establish whether the device is controllable and which method should be used to control the damper.

Chapter 7

RESULTS AND DISCUSSION

The experiments performed on the damper were designed to verify the design, and quantify the acceleration response for different PWM schemes. Based on this information an appropriate control scheme may be developed. The method used to verify the design included changing the frequency and duty cycle of the PWM signal, while observing the transducers during each drop. The effectiveness of the damper is based upon how well it responds to the generated magnetic field.

7.1 Experiment Observations

The three traducers implemented were monitored during the various tests described in Chapter 6. The two accelerometers agreed with each other, as shown for an arbitrary drop in Figure 7.1.

Since the accelerometers give the same information, only one accelerometer output is shown in all subsequent graphs. Accelerometer 2 is shown, due to the smaller associated error (see Section 5.1). The experiment is first observed while stationary, then dropped under different PWM schemes.

7.1.1 Stationary testing

Before the shock absorber and mass could be dropped, the various components had to be checked. While stationary, the control circuit was initiated and the accelerometers were supplied with 9 V. The controller was then set to sample the two accelerometers to verify that everything was in working order. In Figure 7.2,

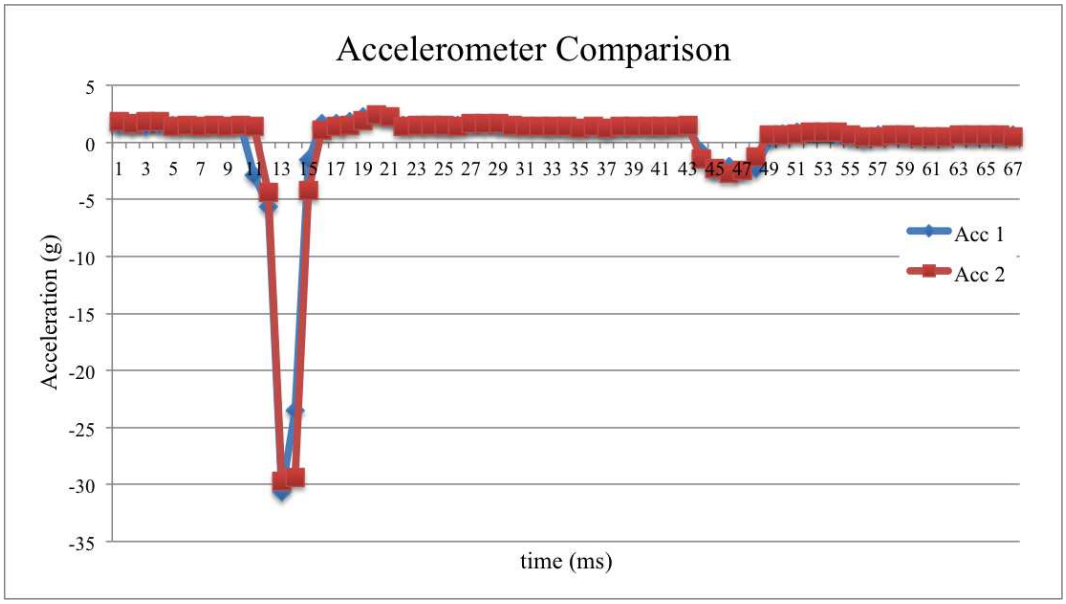


Figure 7.1: Comparison of the two accelerometers.

the data from this experiment is compared to the data obtained when the coil was energised with a 12 V_p signal at 20 kHz

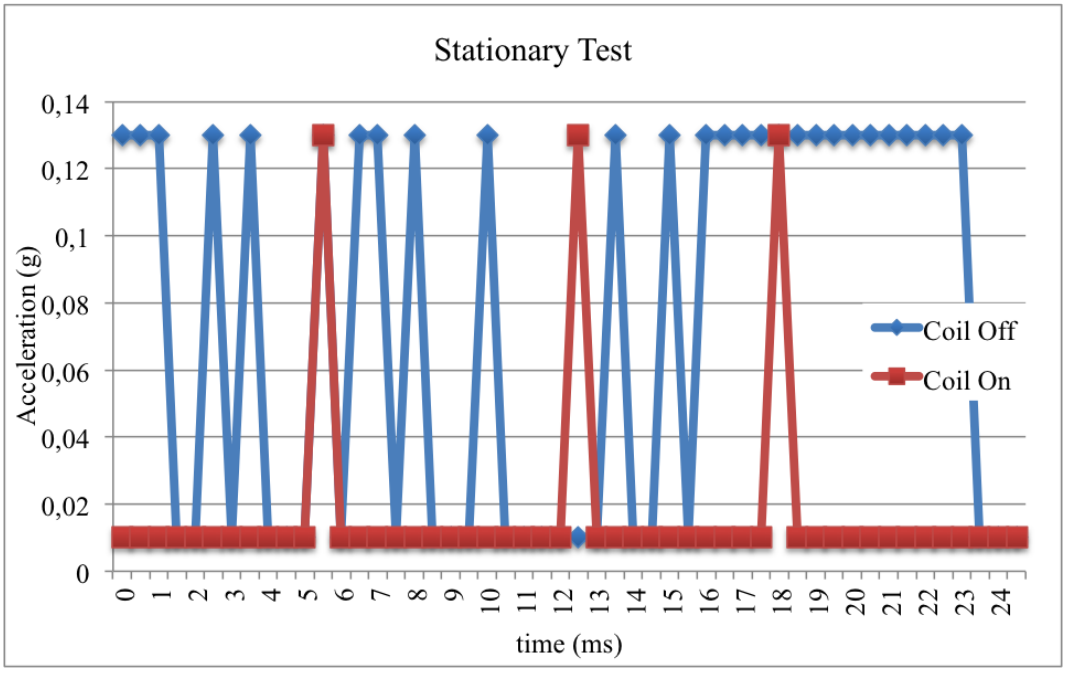


Figure 7.2: Accelerometer output while stationary.

The graph for the coil off emphasises the small changes in voltage, but in general stays between 0,51 g and 0,63 g. Similarly, the data obtained while the coil is on follows the same trend, but with less fluctuations. This is most likely due to

constructive interference from the coil switching. Since the accelerometer signals are filtered close to the micro-processor, any high frequencies induced along the transmission wires for the accelerometers are effectively reduced so as to be undetectable.

7.1.2 Thermal response

Keeping the damper stationary, the thermal response of the fluid inside the damper was observed to determine if the device operated at safe temperatures. With a duty cycle of 50 % and a maximum current of 1,5 A, the frequency of the PWM signal was changed to the same values as used in the subsequent section. The resulting thermal response of the fluid in the damper is shown in Figure 7.3.

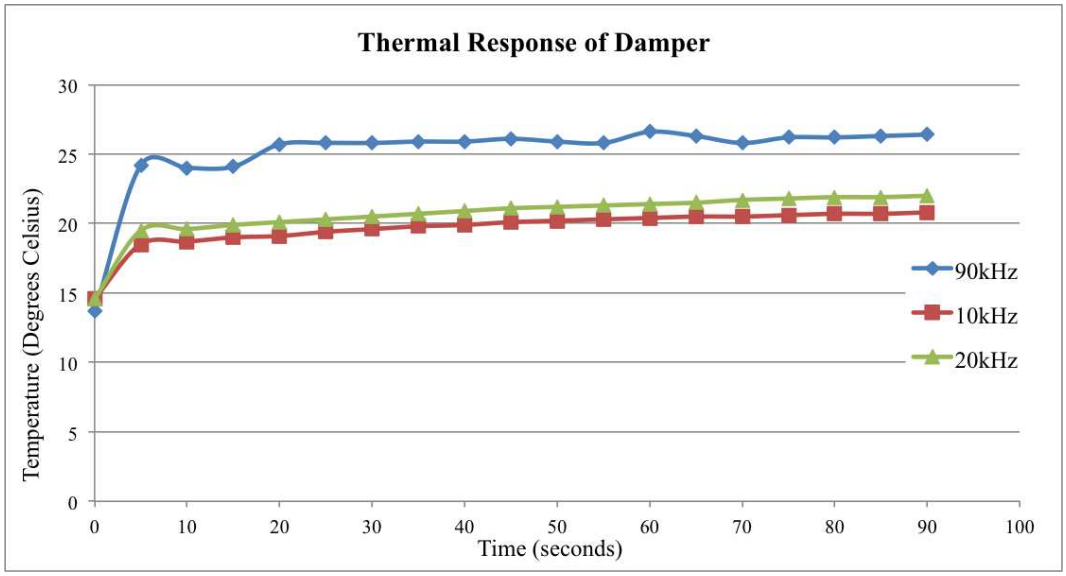


Figure 7.3: Thermal response of the three operating frequencies.

Each time a test was performed, the damper was allowed 30 minutes to return to approximately 14 °C which was the ambient temperature on the day of testing. It was observed that the temperature of the fluid increased quickly for the first 10 seconds for all frequencies. After the initial rise, the temperature dropped slightly. This effect is more pronounced for higher frequencies and is explained in Section 7.2.

After 25 seconds, the temperature increase was more gradual and asymptotes toward a set value based on frequency. The 10 kHz frequency stabilised to 24,5 °C after 30 minutes. Likewise, the 20 kHz reached 28,9 °C and 90 kHz reached 30,0 °C. When the damper was dropped from 120 mm, the increase in temperature was no more than

1,4 °C, which dropped back to the steady state temperature after approximately 20 seconds.

7.1.3 Incremented frequency

To determine how the damping will respond to a change of frequency, the damper was dropped using the same conditions as outlined for the duty cycle tests. By varying the frequency of the PWM signal to the damper, the graph in Figure 7.4 shows how the system responded.

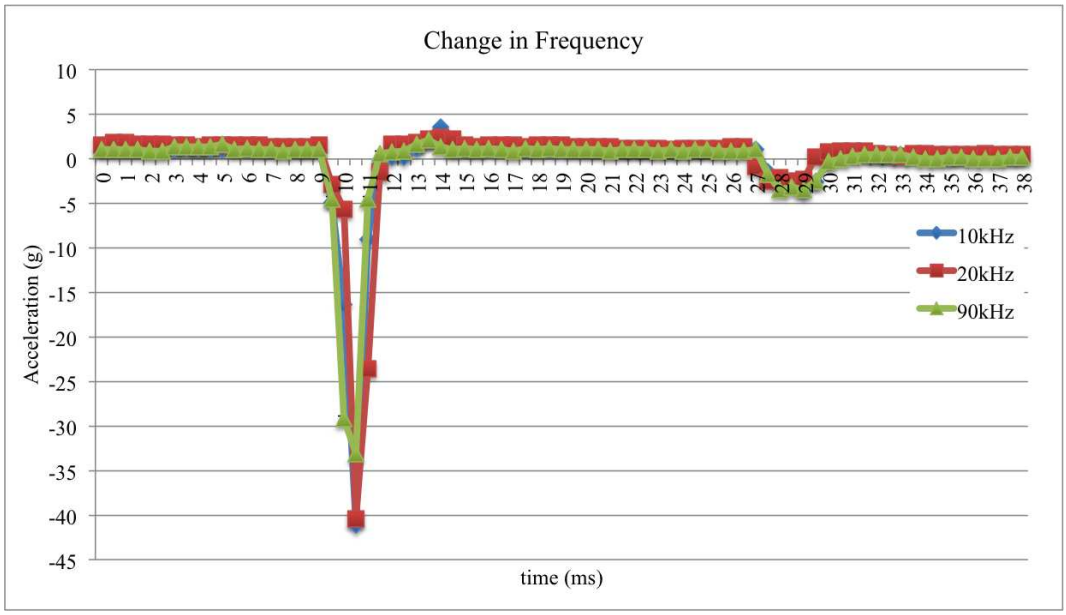


Figure 7.4: Comparison of all the different frequency schemes.

The various frequencies used gave no obviously discernible difference between damper impacts. The implications of this are discussed fully in Section 7.2. Fixing the frequency to 20 kHz, the duty cycle was then manipulated to determine if it is possible to control the damper.

7.1.4 Incremented duty cycle

The duty cycle was tested by dropping the damper under different duty cycle conditions. Each impact was repeated three times to confirm repeatability, as shown in Figure 7.5 for a duty cycle of 50 %.

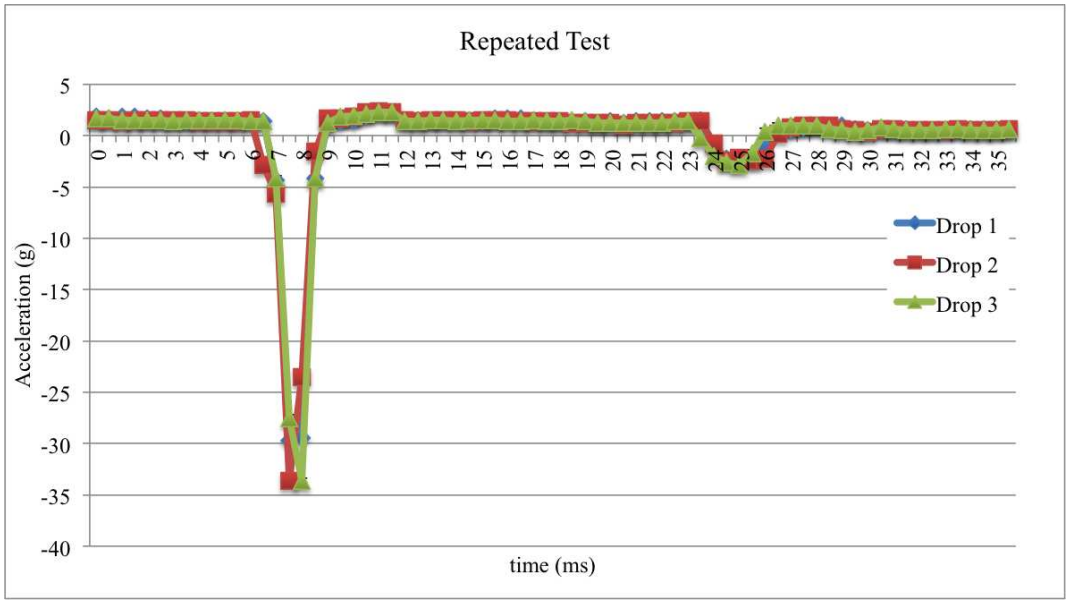


Figure 7.5: Acceleration data from three tests under identical conditions.

Each impact was quite consistent. Initially, the sensor read approximately 1 g. When the impact occurs, the accelerometers experience a negative acceleration with a maximum of $-33{,}66$ g. The sensor then reverts to 1 g for 14 ms, when a second impact occurs of far less magnitude (measured at a maximum of $-2{,}58$ g). Finally, the accelerometers registered approximately 0 g when the damper was at rest.

Comparing all the duty cycle schemes yields the Figure 7.6. A similar trend was found for each duty cycle, except the peak magnitude for the initial impact was higher for increased duty cycle percentage. Also of interest is the duration over which the impact occurs.

The longest duration of 5 ms occurred during a 0 % duty cycle drop, while the time got progressively shorter for increased duty cycle percentage. The impact occurred for just over 2,5 ms with a 76 % duty cycle.

Also of interest was the 0 % duty cycle produced no second impact, whilst the second impact occurred for an increase in duty cycle. The damper was found to only use approximately 7 mm of the 20 mm stroke available during all impacts.

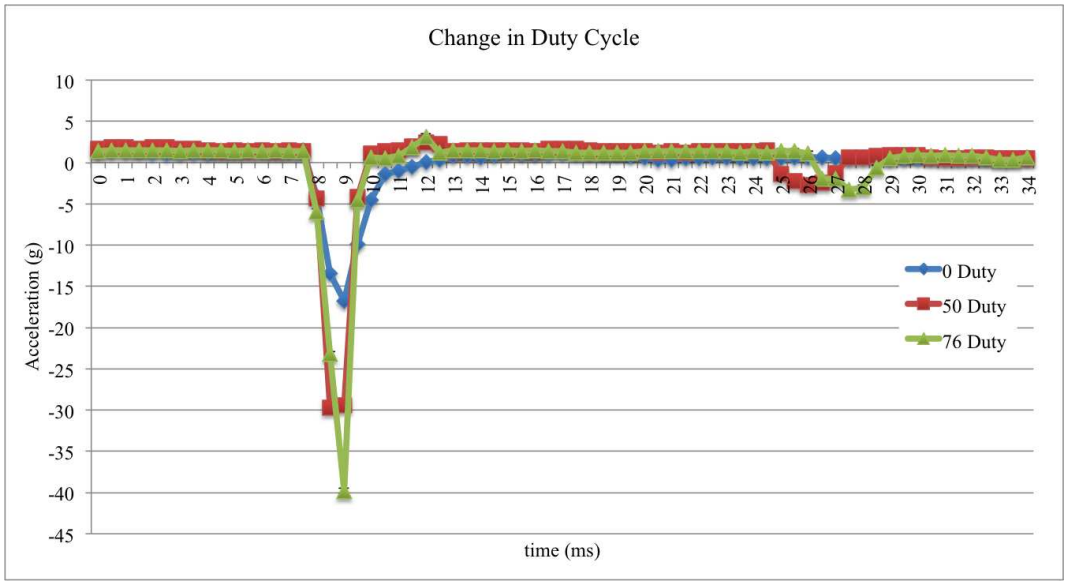


Figure 7.6: Comparison of all the different duty cycle schemes.

7.2 Analysis

When measuring the thermal response of the system, the temperature increase was due to the powering of the coil heating the fluid. While the initial change in temperature was relatively sudden, the ambient temperature still limited the maximum temperature that the fluid could reach. The slight drop in temperature is most likely due to the placement of the thermocouple cable, which is in an area that allows fluid flow. The heated fluid moved by convection currents, exposing the transducer to cooler fluid before the fluid started to heat up more uniformly.

The temperature stabilised over time when the total energy input into the system equated to the net energy lost. It was anticipated that higher frequencies would cause higher temperatures, as this would create more movement of the magnetic particles as well as an increase in the impedance of the inductor.

The temperature ranges are well below the flash point of MR fluid and unlikely to cause enough fluid expansion for leaking to occur. While dropping the damper does cause an increase in temperature, the increase is minor for the small drop heights tested.

The drop test revealed a pattern as shown in Figure 7.7, where each region is identified from the information gleaned from the transducers. While the region of most interest is the initial impact, the impact is better understood by considering

all regions jointly.

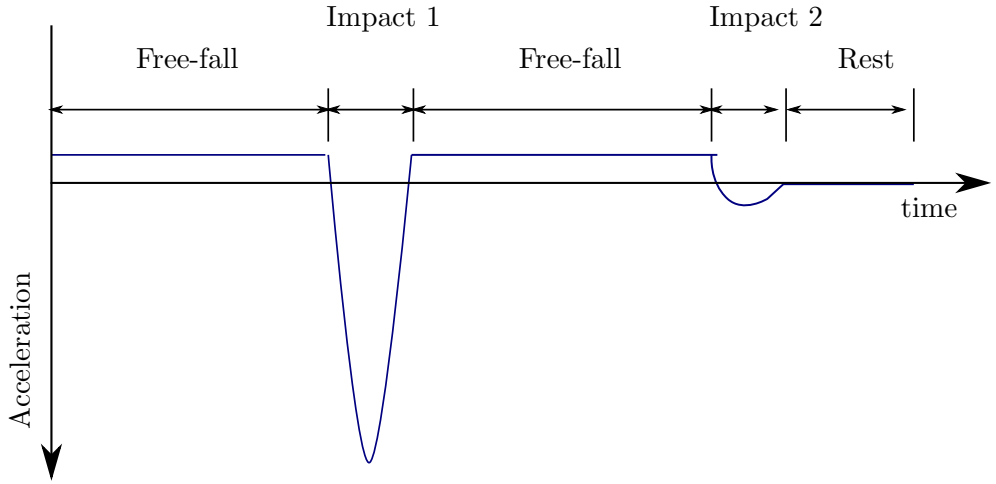


Figure 7.7: Illustrative graph of the different regions during damping.

Free-fall occurs in the first region. The free-fall for all experiments registered between 1,23 g and 1,53 g, which is expected as no external force other than gravity acts on the damper.

The first impact time got shorter with increased duty cycle. This is due to the shock absorber damping increasing from an increased fluid yield stress. Because the damper effectively becomes more rigid, the force applied in the opposite direction to the damper's descent increases with increased duty cycle.

This also results in the damper bouncing higher, as observed by the second free-fall region, thereby delaying the second impact. The second impact is not as significant as the first impact in terms of both the RLT to be performed and in terms of the magnitude, which reaches a maximum of $-3{,}3$ g. After the second impact the damper once again returns to rest conditions, indicating an end to the experiment.

Controlling the damper using frequency would prove very ineffective given the data obtained when changing the frequency. The MR fluid responds sufficiently quickly to a change in magnetic field, which makes the average yield stress of the fluid constant for varying frequency schemes. The frequency can not be dropped much lower than 10 kHz because then it would become comparable to the sampling rate, and faster than 90 kHz would be inefficient due to the skin frequency of the wire and the expected heating effect from the vibrating magnetic particles.

While only 7 mm of the stroke is used when dropping from a height of 120 mm, it

is expected that more stroke would be used for much higher drop heights as the impact would occur at a higher velocity. This may also increase the impact time so that the desired 50 ms may be achieved.

7.3 Conclusion

The stationary test verified that all the various components integrated and operated as anticipated at a safe temperature. Each subsequent test proved to be repeatable, with the damper responding well to a change in duty cycle but not to a change in frequency. The duration of each impact was shorter than required for an RLT, and only 7 mm of the stroke was used. By implementing a control algorithm and dropping the damper from significantly higher up, it is anticipated that more stroke would be used and the duration of the impact time extended.

Chapter 8

SUMMARY CONCLUSIONS AND RECOMMENDATIONS

By placing a coil in the damper and widening the annular gap, the damper was made ready for the MR fluid. The driver circuit is able to supply current to the coil which noticeably changed the impact in terms of duration and force applied. This difference is detectable by the accelerometers which are calibrated to minimise the error. The designed controller is able to monitor the transducers and interface to the driver circuit. By programming the micro-controller, an algorithm may be developed to control the non-linear damper [57–59]. During the course of the research, several design improvements were considered, but all critical design changes were made when appropriate.

8.1 Recommendations for Future Work

While the damper system is capable of preforming the task required of it, there are several recommendations that may improve the operation of the technology. The recommendations were not implemented as they were all not critical to the project and would have improved the design, but at the cost of more time and increased design complexity.

The changes recommended for the damper consider the effect of temperature changes, further testing of the coil design and evaluation of the altered gap. Currently, the temperature of the fluid is monitored to avoid thermal expansion. A better method of dealing with thermal expansion would be to use an accumulator or valve which would compensate for volume change due to thermal effects [60]. This was not

added as it is unlikely that the damper will be used for long periods of time at high temperature conditions [7, 8].

Fluid loss was also considered during the coil placement and design. The cavity for the coil is large enough to place two parallel coils inside. Using parallel coils would reduce the impedance and may improve the system response time [7]. Only a single coil was used as placing a parallel coil is difficult to implement without creating a large wire access whole, which would increase the chance of fluid leaking.

The damper could also be tested in various ways to ascertain the performance and durability of the shock absorber, as well as to verify theoretical models [8]. While this information is of interest, it is out of scope for this project which focuses on the development of a measurement and control system for the damper.

While the controller is fully operational and achieves all its functions, several design improvements could be incorporated into the next revision. The PIC processor would transmit data faster with USB communication, thereby avoiding the timing issues encountered with real-time data transfer via RS-232. This improvement would require re-fabricating of the PCB, purchase of a different micro-controller, as well as changing the code and peripheral device software.

In terms of the PCB layout and terminals, mounting holes would have made the packaging simpler. Additionally, a set reference rather than using a POT scaler would avoid the reference-shift when connected to a portable supply. This issue was avoided by using an internal reference of 5 V when not working off a bench power supply. When the controller is reset, the driver input is low, which is then inverted and causes the MOSFET gate to be biased. This has the effect of shorting the supply if the coil is engaged. A non-inverting driver would avoid this issue.

The accelerometer calibration process could be simplified by using a smaller motor in conjunction with a variac to directly control the rotational speed of the rotor, this method would allow a greater range of centripetal accelerations, giving a calibration curve with better sensitivity. Having no small motor with access to the drive shaft for mounting objects to, the time required to set up a more accurate calibration process would have been great.

Furthermore, dynamically calibrating the accelerometers would improve the associated errors dramatically. To implement this would require increased complexity in the microchip algorithm and a more sophisticated calibration process.

The process used to test the assembled device is governed by the support rig. The rig could be improved by installing a catch and release mechanism which would make the tests easier to perform and improve the quality of the testing results. An electronic trigger could also be used to fine tune the timing of the impact. A load-cell could also be incorporated to give a direct reading of the force applied. While these are appealing options, they involve more cost, time and complexity.

8.2 Summary and Conclusions

The damper is to aid in the development of a new non-destructive, rapid load test method. This is accomplished by altering a prototype shock absorber so that it may give a controlled force to a material. Only preliminary testing was performed before being handed to the School of Civil Engineering in the University of the Witwatersrand. The device is to be used in a laboratory to analyse various materials and pile samples.

The technology produced is limited to load bearing piles, with the initial focus being cast—in—place concrete piles. Using non-destructive testing techniques, the goal is to develop a test similar to the Statnamic and Fundex Pile Test. It is anticipated that the Unloading Point Method, which focuses on pile penetration versus the force applied, will be used to evaluate the piles. By monitoring the accelerometers attached to the falling mass, it is possible to both control the time period and amount of force applied to a pile.

In summary, a prototype damper was altered to allow the device to be controlled so as to solve the problem of creating a new RLT. While the test itself is not yet fully developed, the electronic support for the test is now available for further development as well as a controllable damper. This was accomplished by modifying the damper, calibrating the transducers, developing a controller and finally testing the arrangement, which meets all the objectives previously discussed.

Appendix A

CONTROLLER SCHEMATIC

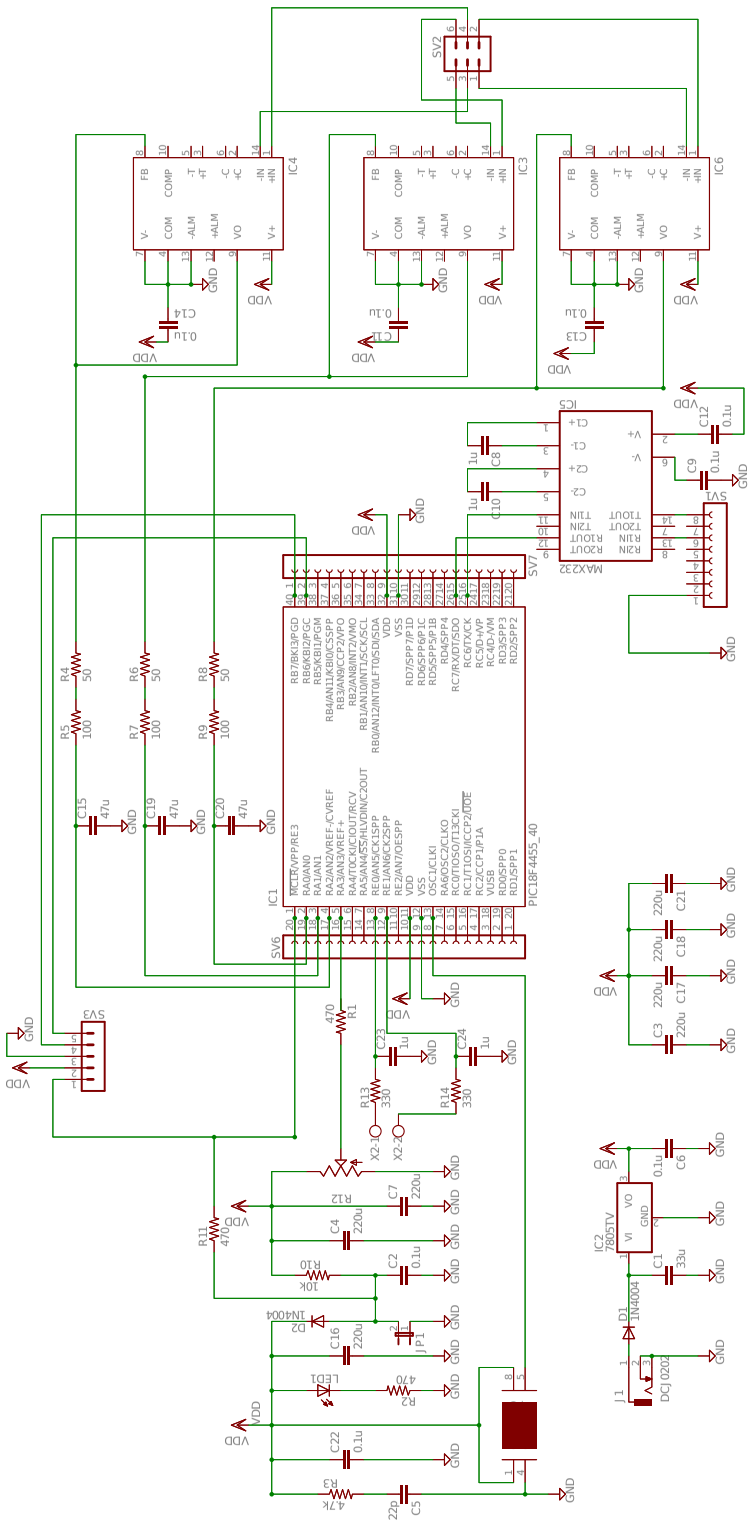


Figure A.1: Circuit diagram of the controller.

Appendix B

DRIVER SCHEMATIC

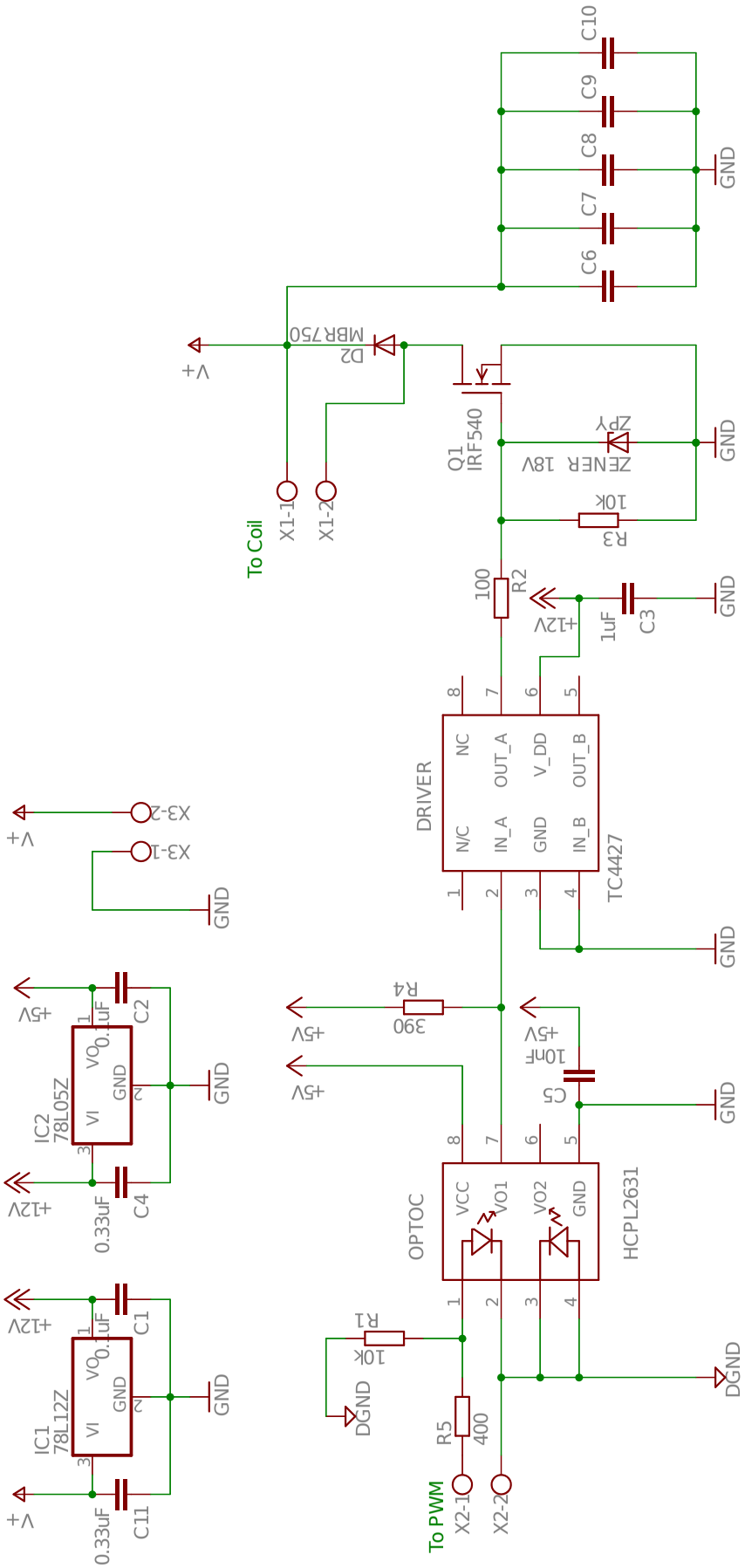


Figure B.1: Circuit diagram of the MOSFET driving circuit.

REFERENCES

[1] J. P. Jones and F. M. Newcomb, *An Introduction to Pile Driving.* Stanford University Construction Institute, 1963. Technical Report 23.

[2] F. W. C. Yen, "Driven Pile Types." http://www.scribd.com/doc/53589571/Types-of-Piles, Last Accessed 14 August 2011.

[3] B. Hertlein and A. Davis, *Nondestructive Testing of Deep Foundations.* West Sussex, England: John Wiley & Sons Ltd, 2006.

[4] I. Luker, "Personal Communication, University of the Witwatersrand." Irvin.Luker@wits.ac.za, November 2010.

[5] K. Rollins and D. Brown, "Static Axial Load Testing." CE6311 Lecture 10, Unpublished Notes.

[6] R. D. Broderick, *Statnamic Lateral Loading Testing of Full-Scale 15- and 9-Group Piles in Clay.* PhD thesis, Brigham Young University, 2007.

[7] G. Yang, J. B. Spencer, J. D. Carlson, and M. Sain, "Large-scale MR Fluid Dampers: Modeling and Dynamic Performance Considerations," *Engineering Structures*, vol. 24, pp. 309–323, 2002.

[8] J. C. Dixon, *The Shock Absorber Handbook.* Great Britain: John Wiley & Sons, Ltd, second ed., 2007.

[9] N. M. Bruno, C. Ciocanel, and A. Kipple, "Modeling Flow of Magnetorheological Fluid through a Micro-channel," in *Proceedings of the COMSOL Conference*, pp. 1–7, 2009.

[10] G. S. Park and S. H. Park, "Determination of the Curvature of the Magnetic Fluid Under the External Forces," *IEEE Transactions on Magnetics*, vol. 38, pp. 957–960, Mar. 2002.

[11] K. Shimada and S. Kamiyama, "Numerical Analysis of Effect of Distribution of Mass Concentration on Steady Magnetic Flow in a Straight Tube," *IEEE Transactions on Magnetics*, vol. 36, no. 5, pp. 3706–3708, 2000.

[12] B. M. Berkovsky, V. F. Medvedev, and M. S. Krakov, *Magnetic Fluids Engineering Applications.* Oxford University Press Inc., 1993.

[13] M. Sain and B. Spencer, "Nonlinear Blackbox Modeling of MR-dampers for Civil Structural Control," *IEEE Transactions on Control Systems Technology*, vol. 13, pp. 345–355, May 2005.

[14] S. Odenbach, *Colloidal Magnetic Fluids: Basics, Development and Application of Ferrofluid*. Berlin Heidelberg: Springer-Verlag, 2009.

[15] "Lord Inc." http://www.lord.com/Home/MagnetoRheologicalMRFluid/, Last Accessed 20 May 2011.

[16] Lord Corporation, Cary, USA, *MRF-132DG: Magneto-Rheological Fluid*, 2008. Data Sheet.

[17] M. Thompson, "Simple Models and Measurements of Magnetically Induced Heating Effects in Ferromagnetic Fluids," *IEEE Transactions on Magnetics*, vol. 34, no. 5, pp. 3755–3764, 1998.

[18] LORD Corporation, USA, *LORD User Instructions: LORD Wonder Box Device Controller Kit*, 2006. Data Sheet.

[19] "Viscosity and Density (Metric SI Units)." http://www.pipeflow.co.uk/ public/articles/Viscosity_And_Density_Units_And_Formula.pdf, Last Accessed 15 November 2010.

[20] "SubsTech Substances and Technology." www.substech.com/ dokuwiki/doku.php, Last Accessed 22 August 2011.

[21] A. G. Olabi and A. Grunwald, "Design and Application of Magneto-Rheological Fluid," *School of Mechanical and Manufacturing Engineering*, pp. 1–19, 2004.

[22] T. Miyasaka, F. Kuwabara, G. Likins, and F. Rausche, "Rapid Load Test on High Bearing Capacity Piles," *The 8th International Conference on the Application of Stress Wave Theory to Piles*, 2008.

[23] P. Middendorp and R. J. van Foeken, "When to Apply Dynamic Load Testing and Statnamic Testing," *2nd Statnamic Seminar*, 1998.

[24] M. Janes, A. Sy, and R. G. Campanella, "A Comparison of Statnamic and Static Axial Load Tests on Steel Pipe Piles in the Fraser Delta," *Vancouver Geotechnical Society, Symposium on Deep Foundations*, no. 118, 1994.

[25] H. Tsang, R. Su, and a. Chandler, "Simplified Inverse Dynamics Models for MR Fluid Dampers," *Engineering Structures*, vol. 28, pp. 327–341, Feb. 2006.

[26] W. Chooi and S. Oyadiji, "Design, Modelling and Testing of Magnetorheological (MR) Dampers Using Analytical Flow Solutions," *Computers and Structures*, vol. 86, pp. 473–482, Feb. 2008.

[27] S. J. Dyke and J. B. F. Spencer, "A Comparison of Semi-Active Control Strategies for the MR Damper," *IEEE Transactions on Control Systems Technology*, pp. 580–584, 1997.

[28] R. A. Serway and J. W. J. Jewett, *Physics for Scientists and Engineers with Modern Physics*. Belmont, CA: Thomson Brooks/Cole, 6th ed., 2004.

[29] Analog Devices, Inc., Norwood, USA, *ADXL78: Single-Axis, High-g, Accelerometers*, 2005. Data Sheet.

[30] P. E. Mix, *Introduction to Nondestructive Testing*. A John Wiley & Sons, Inc., second ed., 2005.

[31] LORD Corporation, Cary, NC, *LORD Material Safety Product: MR FLUIDS MRF-132DG*, 2008. Data Sheet.

[32] P. Lorrain and D. Corson, *Electromagnetism Principals and Applications*. New York: W. H. Freeman and Company, second ed., 2001.

[33] Maxim Integrated Products, Inc, California, USA, *MAX220: Maxim Driver/Receivers*, 2006. Data Sheet.

[34] Microchip Technology Inc., USA, *PIC18FXX2 Data Sheet*, 2002. Data Sheet.

[35] Fairchild Semiconductors, California, USA, *LM78XX: 3-Terminal 1A Positive Voltage Regulator*, 2008. Data Sheet.

[36] T. H. Hubing, "Effective Strategies for Choosing and Locating Printed Circuit Board Decoupling Capacitors," *International Symposium on Electromagnetic Compatibility*, 2005.

[37] T. H. Hubing, "PCB EMC Design Guidelines: A Brief Annotated List," *IEEE Symposium on Electromagnetic Compatibility*, pp. 34–36, 2003.

[38] I. Hofsajer, "Personal Communication, University of the Witwatersrand." Ivan.Hofsajer@wits.ac.za, 2010.

[39] "Design Considerations for Mixed-Signal: How to Design a PCB Layout." www.e2v.com, Last Accessed 10 November 2010. Application Note.

[40] V. Rosten, *Design-in of RF circuits*. Nordic VLSI ASA, Norway, 2002. White Paper.

[41] J. Wang, H. Hu, J. Wang, Z. Li, and Z. Gong, "Development of an Embedded Control System for Magnetorheological Fluid Damper Under Impact Load," in *The Ninth International Conference on Electronic Measurement & Instruments*, 2009.

[42] Fairchild Semiconductor Corporation, *HCPL2601: Single-Channel High Speed 10MBit/s Logic Gate Optocouplers*, 2008. Data Sheet.

[43] Microchip Technology Inc., USA, *TC4427 1.5A Dual High-Speed Power MOSFET Drivers*, 2006. Data Sheet.

[44] L. Balogh, *Design And Application Guide For High Speed MOSFET Gate Drive Circuits*. Texas Instruments. White Paper.

[45] B. Maurice and L. Wuidart, *Application Note: Drive Circuits for Power MOSFETs and IGBTs*. STMicroelectronics, 1999.

[46] A. Fabre, M. Alami, B. Alaoui, and A. Bouhdada, "Two New Temperature Compensated Current Sources," *IEEE Transactions on Circuits and Systems I: Fundamental Theory and Applications*, vol. 44, no. 11, pp. 1071–1074, 1997.

[47] International Rectifier, California, USA, *IRF540: HEXFET Power MOSFET*, 2005. Data Sheet.

[48] Microchip Technologies Inc., USA, *TC1410: 0.5A High-Speed MOSFET Drivers*, 2003. Data Sheet.

[49] IEEE-SA Standards Board, New York, *IEEE Standard Specification Format Guide and Test Procedure for Linear Single-Axis, Nongyroscopic Accelerometers*, 2008.

[50] Maxim Integrated Products, Inc, California, USA, *MAX4040: Single/Dual/Quad, Low-Cost, SOT23, Micropower Rail-to-Rail I/O Op Amps*, 2005. Data Sheet.

[51] J. P. Bentley, *Principles of Measurement Systems*. Edinburgh Gate, Harlow: Pearson Prentice Hall, fourth ed., 2005.

[52] C. Phillips, J. Parr, and E. Riskin, *Signals, Systems, and Transforms*. Upper Saddle River, New Jersey: Pearson Education, Inc., third ed., 2003.

[53] D. Marioli, E. Sardini, and A. Taroni, "A System for the Generation of Static and Very Low-frequency Reference Accelerations," *IEEE Transactions on Instrumentation and Measurement*, vol. 46, no. 1, pp. 27–30, 1997.

[54] D. Mitrani, J. Tomé, J. Salazar, A. Turó, J. M.J. García, and A. Chávez, "Methodology for Extracting Thermoelectric Module Parameters," *Instrumentation*, vol. 54, pp. 1548–1552, 2005.

[55] Analog Devices, Inc., Norwood, USA, *AD595: Monolithic Thermocouple Amplifiers with Cold Junction Compensation*, 1999. Data Sheet.

[56] Fluke Corporation, Washington, USA, *Fluke 5520A Multi-Product Calibrator*, 2003. Data Sheet.

[57] S. D. Cairano, A. Bemporad, I. Kolmanovsky, and D. Hrovat, "Model Predictive Control of Nonlinear Mechatronic Systems: An Application to a Magnetically Actuated Mass Spring Damper," *Elsevier Publications, IFAC*, pp. 241–246, 2006.

[58] B. Kim and P. N. Roschke, "Magnetorheological Behaviour Using a Neural Network," *Proceedings Of The American Control Conference*, 1999.

[59] K. C. Schurter and P. N. Roschke, "Fuzzy Modelling of a Magnetorheological Damper Using ANFIS," *IEEE Xplore*, 2000.

[60] F. Gordaninejad and E. O. Ericksen, "Controllable Magneto-Rheological Fluid Damper," 28 01, 2003. US Patent US 6,510,929 B1.

Bibliography

M. I. Greenberg, D. C. Cone, and J. R. Roberts, *Material Safety Data Sheet*. Lord Corporation, Mar. 1996.

Y.-S. Koh, "Double-Tube Shock Absorber Using a Hydraulic Fluid and a Magnetorheological Fluid," 2002.

L. Love, J. Jansen, T. McKnight, Y. Roh, T. Phelps, L. Yeary, and G. Cunningham, "Ferrofluid Field Induced Flow for Microfluidic Applications," *IEEE/ASME Transactions on Mechatronics*, vol. 10, pp. 68–76, Feb. 2005.

E. N. Anderfaas and D. Banks, "Magnetorheological Damper System," 11 10, 2005. US Patent US 6,953,108 B2.

D. Kelland, "Magnetic Separation of Nanoparticles," *IEEE Transactions on Magnetics*, vol. 34, pp. 2123–2125, July 1998.

S. Mercer, "Minimizing RF PCB Electromagnetic Emissions," *RF Design*, pp. 46–49, 1999.

M. Ahmadian and J. Norris, "Experimental Analysis of Magnetorheological Dampers When Subjected to Impact and Shock Loading," *Communications in Nonlinear Science and Numerical Simulation*, vol. 13, pp. 1978–1985, Nov. 2008.

P. C. Chen and N. Wereley, "Magnetorheological Damper and Energy Dissipation," 24 02, 2004. US Patent US 6,694,856 B1.

T. H. Hubing, "Building IC Models Based on Measurements and Using these Models Productively," *Clemson University*, pp. 1–3, 2007.

R. E. Rosensweig, "Viscosity of Magnetic Fluid in a Magnetic Field," *Journal of Colloid and Interface Science*, vol. 29, no. 4, pp. 680–686, 1969.

R. D. Anderson, "Method for Controlling the Damping Force of a Damper," 08 04, 2003. US Patent US 6,543,589 B2.

M. Lita, N. Popa, C. Velescu, and L. Vekas, "Investigations of a Magnetorheological Fluid Damper," *IEEE Transactions on Magnetics*, vol. 40, pp. 469–472, Mar. 2004.

D. Carlson, B. Marjoram, J. Toscano, and D. Leroy, *Magneto-Rheological Technology and Applications*. Lord Corporation, France, 2007.

LORD Corporation, *Lord Technical Data: RD-1005-3 Damper*, 2006.

D. Schmitt and T. S. Fiez, "A Low Voltage CMOS Current Source," *Washington State University*, vol. 3, no. 2, pp. 110–113, 1997.

L. C. Félix-herrán, J. D. J. Rodríguez-ortiz, R. Soto, R. Ramírez-mendoza, T. D. Monterrey, C. Monterrey, A. Eugenio, and G. Sada, "Modeling and Control for a Semi-active Suspension with a Magnetorheological Damper Including the Actuator Dynamics," in *Electronics, Robotics and Automotive Mechanics Conference*, pp. 338–343, 2008.

G. T. Ngatu and N. M. Wereley, "Viscometric and Sedimentation Characterization of Bidisperse Magnetorheological Fluids," *IEEE Transactions on Magnetics*, vol. 43, pp. 2474–2476, June 2007.

Z. Tianjun and Z. Changfu, "Development of MRF Damper Modelling and Validation of MRF Damper Test," *IITA International Conference on Control, Automation and Systems Engineering*, vol. 6, pp. 238–241, July 2009.

J. Dunn, *Matching MOSFET Drivers to MOSFETs*. Microchip Technology Inc., 2004.

R. Rajapakse, *Pile Design and Construction Rules of Thumb*. Oxford: Butterworth-Heinemann, 2008.

T. Hubing, J. Chen, J. Drewniak, T. Van Doren, Y. Ren, J. Fan, and R. DuBroff, "Power Bus Noise Reduction Using Power Islands in Printed Circuit Board Designs," *University of Missouri-Rolla*, 1996.

G. M. Veca and C. Cataldi, "The Magnetorheological Fluid Damper Dynamic Model," *Electrical Engineering*, pp. 2010–2010, 2006.

R. Morais, G. Goncalves, K. Skeff Neto, F. Pelegrini, and N. Buske, "Study of particle-particle interaction in magnetic fluids using magnetic resonance," *IEEE Transactions on Magnetics*, vol. 38, pp. 3225–3227, Sept. 2002.

C. Rinaldi, A. Chaves, S. Elborai, X. Tony, and M. Zahn, "Magnetic Fluid Rheology and Flows," *Current Opinion in Colloid & Interface Science*, vol. 10, pp. 141 – 157, 2005.

M. L. Oliver, "Magneto-Rheological Damping Apparatus," 21 05, 2002. US Patent US 6,390,253 B1.

M. Tomlinson and J. Woodward, *Pile Design and Construction Practice*. London and New York: Taylor and Francis Group, fifth ed., 2008.

A. K. Samantaray, "Modeling and Analysis of Preloaded Liquid Spring/Damper Shock Absorbers," *Simulation Modelling Practice and Theory*, vol. 17, pp. 309–325, Jan. 2009.

Y.-S. Koh, "Shock Absorber Using a Hydraulic Fluid and a Magnetorheological Fluid," 26 03, 2001. US Patent US 6,360,856 B1.

O. Ciftja, "Lamellar-like Structures in Ferrofluids Placed in Strong Magnetic Fields," *Solid State Communications*, vol. 149, pp. 532–536, 2009.

S. Beresnev, V. Polevikov, and L. Tobiska, "Numerical Study of the Influence of Diffusion of Magnetic Particles on Equilibrium Shapes of a Free Magnetic Fluid Surface," *Communications in Nonlinear Science and Numerical Simulation*, vol. 14, pp. 1403–1409, Apr. 2009.

L. Huixin, Q. Ping, and Z. Qunli, "The Finite Element Analysis of Pile-anchor Support System in Foundation Pit," *Second International Conference on Information and Computing Science*, 2009.

R. Pereira, G. Goncalves, F. Bakuzis, P. Morais, R. Azevedo, and K. Neto, "Magnetic Birefringence in Copper and Zinc Ferrite-based Ionic Magnetic Fluids," *IEEE Transactions on Magnetics*, vol. 37, pp. 2657–2659, July 2001.

Z. Tianjun and Z. Changfu, "Development of MRF Damper Modelling and Validation of MRF Damper Test," *IITA International Conference on Control, Automation and Systems Engineering*, vol. 6, pp. 238–241, July 2009.

M. Aquino, G. Miano, C. Serpico, W. Zamboni, and G. Coppola, "Forces in Magnetic Fluids Subject to Stationary Magnetic Fields," *IEEE Transactions on Magnetics*, vol. 39, no. 5, pp. 2657–2659, 2003.

J. Bajkowski, J. Nachman, M. Shillor, and M. Sofonea, "A Model for a Magnetorheological Damper," *Mathematical and Computer Modelling*, vol. 48, pp. 56–68, 2008.

V. M. Ulitskii, "History of Pile Foundation Engineering," *Soil Mechanics and Foundation Engineering*, vol. 32, no. 3, pp. 35–38, 1995.

H. Shim, Y. Fu, and T. H. Hubing, "Radiated Emissions from Populated Printed Circuit Boards Due to Power Bus Noise," *International Symposium on Electromagnetic Compatibility*, vol. 00, pp. 396–400, 2004.

M. Cho, S. Lim, I. Jang, H. Choi, and M. Jhon, "Encapsulation of Spherical Iron-Particle with PMMA and its Magnetorheological Particles," *IEEE Transactions on Magnetics*, vol. 40, pp. 3036–3038, July 2004.

V. Ervithayasuporn and Y. Kawakami, "Synthesis and Characterization of Core Shell Type Fe_3O_4 Nanoparticles in Poly(organosilsesquioxane)," *Journal of Colloid and Interface Science*, vol. 332, no. 2, pp. 389–393, 2009.

P. P. Phule, "Magnetorheological Fluid," 16 11, 1999. US Patent 5,985,168.

P. Fannin, "On the High-Frequency Measurement of the Dynamic Properties of Nano-Particle Colloids," *Journal of Magnetism and Magnetic Materials*, vol. 321, pp. 850–853, 2009.

C. Rostamzadeh and B. Archambeault, "Numerical and Experimental Investigation of PCB Ground-fill on Radiated EMI," *IEEE International Symposium on Electromagnetic Compatibility*, vol. 7, pp. 79–83, 2006.

T. Rheinlander, J. Justiz, A. Haller, R. Kotitz, W. Weitschies, and W. Semmler, "Dynamic Properties of Fractions Yielded by Magnetic Fractionation of Magnetic Fluids," *IEEE Transactions on Magnetics*, vol. 35, no. 5, pp. 4055–4057, 1999.

Y. Amirat and K. Hamdache, "Strong Solutions to the Equations of a Ferrofluid Flow Model," *Journal of Mathematical Analysis and Applications*, vol. 353, no. 1, pp. 271–294, 2009.

S. Rollier, C. Benz, and H. D. Huber, *Technical Information LTSR: ASIC Based Closed-Loop Transducers from 6A up to 25A Nominal with Reference Access.* LEM Components, 2003.

C. H. Chen, ed., *Ultrasonic and Advanced Methods for Nondestructive Testing and Material Characterization.* Singapore: World Scientific Publishing Co., 2007.

S. Chatterjee, "On the Principle of Impulse Damper: A Concept Derived from Impact Damper," *Journal of Sound and Vibration*, vol. 312, pp. 584–605, Feb. 2008.

K. Hayashi, W. Sakamoto, and T. Yogo, "Magnetic and Rheological Properties of Monodisperse Fe_3O_4 Nanoparticle/Organic Hybrid," *Journal of Magnetism and Magnetic Materials*, vol. 321, pp. 450–457, Mar. 2009.

W. Anderson, *Controlling Electrohydraulic Systems.* Minnesote: Marcel Dekker Inc., 1998.

E. Roza, "Analog-to-digital Conversion Via Duty-cycle Modulation," *IEEE Transactions on Circuits and Systems II: Analog and Digital Signal Processing*, vol. 21, no. 6, pp. 87–914, 1997.

T. Pranoto, K. Nagaya, Y. Ebara, and Q. Long, "Vibration Suppression Device Using Permanent-Electromagnet and MRF Shear Damper," *Journal of Materials Processing Technology*, vol. 181, pp. 235–240, Jan. 2007.

C.-m. Chew, G.-S. Hong, and W. Zhou, "Series Damper Actuator: A Novel Force/Torque Control Actuator," *IEEE*, pp. 533–546, 2004.

T. Schmitz and M. Wong, *Choosing and Using Bypass Capacitors.* Intersil Corporation, 2007.

Microchip Technology Inc., *MPLAB C30 C Compiler User's Guide*, 2005.

P. Morais, O. Silva, P. Gravina, L. Figueiredo, E. Lima, L. Silva, R. Azevedo, and K. Neto, "Cadmium-ferrite Based Magnetic Fluid: Birefringence and Transmission Electron Microscopy Investigation," *IEEE Transactions on Magnetics*, vol. 39, pp. 2639–2641, Sept. 2003.

J. Liu, K. Xia, and C. Zhu, "Structural Vibration Intelligent Control Based on Magnetorheological Damper," 2009. White Paper.

H. Johnson and M. Graham, *High-Speed Digital Design*. Prentice Hall, Inc., 1993.

S. Shuchi, T. Mori, and H. Yamaguchi, "Flow Boiling Heat Transfer of Binary Mixed Magnetic Fluid," *IEEE Transactions on Magnetics*, vol. 38, pp. 3234–3236, Sept. 2002.

S. Rollier, C. Benz, and H. D. Huber, "Technical Information LTSR: ASIC Based Closed-Loop Transducers from 6A up to 25A Nominal with Reference Access," 2003.

J. Lozoya-santos, R. Morales-menendez, and R. Ramirez-mendoza, "MR-Damper Based Control System," in *IEEE International Conference on Systems, Man, and Cybernetics*, 2009.

M. Hossain, W. A. Davis, T. R. Howard Jr, and R. L. Carter, "Design of V_{BE} Referenced Bootstrap Current Source, Sensitivity, and Self-Heating Effect," *IEEE*, pp. 2008–2011, 2008.

F. Tyan, S.-h. Tu, and W. S. Jeng, "A Lyapunov Based Multi-level Controller for a Semi-active Suspension System with an MRF Damper," in *American Control Conference*, (Taipei), pp. 3213–3218, 2008.

G. R. Liu and X. Han, *Computational Inverse Techniques in Nondestructive Evaluation*. CRC Press LLC, 2003.

H. Liu, P. Qi, and Q. Zhou, "The Finite Element Analysis of Pile-Anchor Support System in Foundation Pit," *Second International Conference on Information and Computing Science*, pp. 131–134, 2009.

C. Sakai, H. Ohmori, and A. Sano, "Modeling of MR Damper with Hysteresis and Application to Vibration Control," *SICE Annual Conference in Fukui*, pp. 2697–2702, 2003.

M. L. Oliver, C. Kruckemeyer, and E. L. Jensen, "Magnetorheological Damper with Piston Bypass," 16 07, 2002. US Patent US 6,419,058 B1.

C. Guo and T. H. Hubing, "Circuit Models for Power Bus Structures on Printed Circuit Boards Using a Hybrid FEM-SPICE Method," *IEEE Transactions on Advanced Packaging*, vol. 29, pp. 441–447, Aug. 2006.

H. Mamiya and I. Nakatani, "Phase Diagram of an Iron-nitride Magnetic Fluid: Effects of Temperature and Weak Magnetic Field," *IEEE Transactions on Magnetics*, vol. 35, no. 5, pp. 4061–4063, 1999.

T. H. Hubing, T. P. V. Doren, and J. L. Drewniak, "Identifying and Quantifying PCB Inductance," *University of Missouri-Rolla*, pp. 205–208, 1994.

Y. Kim, R. Langari, and S. Hurlebaus, "Semiactive Nonlinear Control of a Building with a Magnetorheological Damper System," *Mechanical Systems and Signal Processing*, vol. 23, pp. 300–315, Feb. 2009.

H. H. Nguyen, D. Nguyen, T. L. Nguyen, C. H. Vu, Q. T. Nguyen, and T. K. Nguyen, "Interaction Between Pile-Soil Under Dynamic Load Using Finite Element Method," 1999.

T. Roy, L. Smith, and J. Prymak, "ESR and ESL of Ceramic Capacitor Applied to Decoupling Applications," *IEEE 7th Topical Meeting on Electrical Performance of Electronic Packaging*, pp. 213–216, 1996.

T. H. Hubing, "The Development of a Closed-Form Expression for the Input Impedance of Power-Return Plane Structures," *IEEE Transactions on Electromagnetic Compatibility*, vol. 45, pp. 478–485, Aug. 2003.

S. Hayashi, S. Saha, and H. Hamaguchi, "A New Class of Magnetic Fluids: bmim[$FeCl_4$] and nbmim[$FeCl_4$] Ionic Liquids," *IEEE Transactions on Magnetics*, vol. 42, pp. 12–14, Jan. 2006.

B. Hertlein and A. Davis, *Nondestructive Testing of Deep Foundations*. John Wiley & Sons Ltd, 2006.

V. Kordonsky, S. Demchuk, I. Prokhorov, and Z. Shulman, "Magnetorheological Fluid and the Methods of Making Thereof," 11 06, 1996. US Patent 5,525,249.

B. Archambeault, "Design Tips: Decoupling Capacitor Connection Inductance," *IEEE*, pp. 71–72, 2009.

H. Chiueh, J. Draper, and J. Choma, "A Dynamic Thermal Management Circuit for System-On-Chip Designs," *8th IEEE International Conference on Electronics, Circuits and Systems*, pp. 577–580, 2003.